

**EQUIVALENT ENERGY BASED DESIGN PROCEDURE FOR CONTROLLED  
ROCKING-CONCENTRICALLY BRACED FRAMES**

by

Vinay Kumar Boddapati

B.Tech., Maharshi Dayanand University, 2013

A THESIS SUBMITTED IN PARTIAL FULFILLMENT OF  
THE REQUIREMENTS FOR THE DEGREE OF

MASTER OF APPLIED SCIENCE

in

THE FACULTY OF GRADUATE AND POSTDOCTORAL STUDIES  
(Civil Engineering)

THE UNIVERSITY OF BRITISH COLUMBIA

(Vancouver)

August 2016

© Vinay Kumar Boddapati, 2016

## **Abstract**

Conventional seismic force resisting systems (SFRSs) such as moment frames, braced frames and shear wall systems rely on the use of ductile design philosophy, where structural components are designed to undergo large inelastic deformations to dissipate the sudden surge of the earthquake energy. This design philosophy has shown to be very effective in preventing structural collapse. However, the extensive inelastic deformation usually leads to significant damage to the structural and non-structural components. Many earthquake reconnaissance reports show that this design philosophy typically leads to residual deformations which result in hefty financial losses. In recent years, novel structural systems, which are targeted to achieve higher performance, have been developed. These structural systems are targeted to resist strong earthquake shaking with minimal structural/non-structural damages. This allows the structure to remain functional immediately after the earthquake. Controlled rocking-concentrically braced frame (CR-CBF) is one such novel system developed to achieve higher performance. CR-CBF relies on the use of post-tensioning (PT) tendons and supplemental damping devices (ED), to create a controlled-rocking mechanism at the base of the structure. Since gravity loads alone cannot eliminate the residual deformations, the PT are introduced in the system to allow self-centering. In addition, ED are installed in the system to dissipate the sudden surge of seismic energy and control the peak displacement response of the structure. Both the PT and ED components are designed to be easily replaceable without affecting the functionality of the structure after a strong earthquake shaking. A novel seismic design methodology named Equivalent-Energy Design Procedure (EEDP) is adopted in this study to design the CR-CBF. This design procedure allows the designers to select different performance objectives at different shaking intensities. Two prototype buildings with

varying heights are designed using EEDP. Detailed numerical models of these prototypes are developed in OpenSees (2010) to evaluate the seismic performance of CR-CBF. Detailed performance assessment of the CR-CBFs, in terms of adjusted collapse margin ratio, are evaluated using the FEMA P695 (2009) methodology. The results presented in this thesis demonstrate that the proposed CR-CBFs have adequate earthquake safety and they can be designed efficiently using the proposed EEDP approach.

## **Preface**

This dissertation is original, unpublished, independent work by the author of this thesis. The author is responsible for the literature review, model development and presentation of the results.

# Table of Contents

<b>Abstract.....</b>	<b>ii</b>
<b>Preface.....</b>	<b>iv</b>
<b>Table of Contents .....</b>	<b>v</b>
<b>List of Tables .....</b>	<b>ix</b>
<b>List of Figures.....</b>	<b>x</b>
<b>List of Symbols .....</b>	<b>xiv</b>
<b>List of Abbreviations .....</b>	<b>xvi</b>
<b>Acknowledgements .....</b>	<b>xvii</b>
<b>Dedication .....</b>	<b>xviii</b>
<b>Chapter 1: Introduction .....</b>	<b>1</b>
1.1    Motivation.....	1
1.2    Background.....	1
1.2.1    Residual Displacements .....	2
1.2.2    Performance-Based Seismic Engineering.....	4
1.2.3    Controlled Rocking Systems.....	5
1.3    Objectives .....	7
1.4    Organization of Thesis.....	9
<b>Chapter 2: Literature Review of Rocking Systems .....</b>	<b>11</b>
2.1    Early Studies of Rocking Structures.....	11
2.2    Flexible Rocking Structures.....	15
2.3    Controlled Rocking System .....	20

2.3.1	Early Developments.....	20
2.3.2	Controlled Rocking Precast Concrete Wall .....	22
2.3.3	Controlled Rocking Bridge Pier.....	24
2.3.4	Controlled Rocking Shear Wall .....	26
2.3.5	Controlled Rocking Steel Frame.....	28
2.3.5.1	Self-Centering Concentrically Braced Frame .....	28
2.3.5.2	Base Plate Yielding System .....	31
2.3.5.3	Viscously Damped Rocking Braced Frame .....	33
2.3.5.4	Controlled Rocking Frame with replaceable energy-dissipating fuses.....	33
2.4	Existing Applications of Controlled Rocking Systems .....	36
2.5	Existing Design Methodologies for Controlled Rocking Steel Frames.....	37
2.6	Summary .....	44
<b>Chapter 3: Equivalent Energy Design Procedure (EEDP) .....</b>		<b>45</b>
3.1	Development of Energy-based Design Methodologies .....	45
3.2	Equivalent Energy Design Procedure (EEDP) and its application in CR-CBF.....	47
3.2.1	Rocking Mechanism of CR-CBF.....	47
3.2.2	Overview of EEDP for CR-CBF.....	52
3.2.2.1	Select Performance Objectives under different Seismic Hazard Intensities.....	55
3.2.2.2	Select Yielding RDR $\Delta y$ to Compute $F_y$ and $T$ .....	55
3.2.2.3	Select Plastic RDR $\Delta p$ to Compute $\gamma a$ and $F_p$ .....	56
3.2.2.4	Calculate $\gamma b$ and Ultimate RDR $\Delta u$ .....	58
3.2.2.5	Distribute Base Shears between Primary and Secondary SFRSs .....	59
3.2.2.6	Select Yielding Mechanisms and Design Structural Members.....	60

3.2.2.6.1	Seismic Demand on ED .....	61
3.2.2.6.2	Seismic Demand on PT .....	62
3.2.2.6.3	Capacity Design of Frame Members.....	62
<b>Chapter 4:</b>	<b>Prototype Design and Numerical Modelling.....</b>	<b>66</b>
4.1	Description of the Prototype Buildings.....	66
4.2	Seismicity and Hazard Selection for the Prototype Site .....	69
4.3	Prototype Design Summary .....	71
4.3.1	3-Storey Prototype .....	72
4.3.2	6-Storey Prototype .....	74
4.4	Numerical Modelling of the Prototypes.....	76
4.4.1	Overview of the Model .....	77
4.4.2	Comparison of Design and Model Time Period .....	79
<b>Chapter 5:</b>	<b>Seismic Performance Assessment of CR-CBF.....</b>	<b>80</b>
5.1	Selection and Scaling of Ground Motions .....	80
5.2	Seismic Response of 3-storey and 6-storey Prototype Buildings .....	83
5.2.1	Peak Forces in the ED and PT .....	83
5.2.2	Peak Displacements .....	84
5.2.3	Residual Displacements .....	88
5.3	Comparison of Seismic Performance of CR-CBF with BRBF.....	89
5.3.1	Description of BRBF Prototype Geometry and Design.....	89
5.3.2	Seismic Response of Systems.....	90
5.3.2.1	Peak Displacements .....	91
5.3.2.2	Peak Accelerations.....	92

5.3.2.3	Residual Displacements .....	94
<b>Chapter 6:</b>	<b>Collapse Margin of Safety Assessment of CR-CBF .....</b>	<b>96</b>
6.1	Overview of Collapse Safety Assessment Methodology.....	96
6.2	Evaluation of Collapse Safety for CR-CBF Prototypes.....	101
<b>Chapter 7:</b>	<b>Conclusion.....</b>	<b>110</b>
7.1	Summary.....	110
7.2	Future Research Needs .....	111
<b>Bibliography .....</b>		<b>114</b>
<b>Appendices.....</b>		<b>121</b>
Appendix A	Design Calculations for 3-Storey Prototype.....	121
A.1	Select Performance Objectives under different Seismic Hazard Intensities.....	121
A.2	Select Yielding RDR $\Delta y$ to Compute $F_y$ and $T$ .....	122
A.3	Select Plastic RDR $\Delta p$ to Compute $\gamma_a$ and $F_p$ .....	122
A.4	Calculate $\gamma_b$ and Ultimate RDR $\Delta u$ .....	122
A.5	Distribute Design Base Shears between Primary and Secondary SFRSs .....	123
A.6	Select Yielding Mechanisms and Design Structural Members.....	123
Appendix B	Design Calculations for 6-Storey Prototype.....	127
B.1	Select Performance Objectives under different Seismic Hazard Intensities.....	127
B.2	Select Yielding RDR $\Delta y$ to Compute $F_y$ and $T$ .....	127
B.3	Select Plastic RDR $\Delta p$ to Compute $\gamma_a$ and $F_p$ .....	128
B.4	Calculate $\gamma_b$ and Ultimate RDR $\Delta u$ .....	128
B.5	Distribute Design Base Shears between Primary and Secondary SFRSs .....	129
B.6	Select Yielding Mechanisms and Design Structural Members.....	129

## List of Tables

Table 4.1 Gravity loads for CR-CBF prototypes .....	68
Table 4.2 Parameters to define design acceleration spectrum .....	70
Table 4.3 Post-tensioning parameters [from DSI (2006)] .....	72
Table 4.4 EEDP design parameters for 3-storey prototype .....	72
Table 4.5 EEDP design parameters for 6-storey prototype .....	75
Table 4.6 Comparison of design and model time period .....	79
Table 5.1 List of ground motions with their scaling factors .....	81
Table 6.1 List of Far-Field ground motions (FEMA P695 2009).....	104
Table 6.2 List of Near-Field ground motions (FEMA P695 2009) .....	105
Table A.1 Calculations for computing ED force demand for 3-storey prototype .....	124
Table A.2 Calculations for computing PT force demand for 3-storey prototype .....	125
Table A.3 Summary of capacity design for 3-storey prototype.....	126
Table B.1 Calculations for computing ED force demand for 6-storey prototype.....	130
Table B.2 Calculations for computing PT force demand for 6-storey prototype .....	131
Table B.3 Summary of capacity design for 6-storey prototype .....	132

## List of Figures

Figure 1.1 Mode of inelasticity in (a) steel moment resisting frame [from Hamburger et al. (2008)] and (b) steel concentrically braced frame [from (Sabelli 2001; Sabelli et al. 2013)].....	3
Figure 1.2 Vision 2000 recommended seismic performance matrix [after SEAOC (1995)] .....	5
Figure 1.3 Seismic response of (a) Conventional SFRS and (b) Controlled Rocking SFRS .....	6
Figure 1.4 Controlled Rocking- Concentrically Braced Frame (CR-CBF) .....	8
Figure 2.1 Housner’s rigid rocking block [after Housner (1963)].....	13
Figure 2.2 Rocking spectrum [plots from Makris and Konstantinidis (2003)].....	14
Figure 2.3 Three-storey rocking frame prototype [from Clough and Huckelbridge (1977)] .....	17
Figure 2.4 Systems used for investigation, with rigid foundation (left) and flexible foundation (right) [after Psycharis (1991)] .....	18
Figure 2.5 Analytical model of flexible rocking structure [after Acikgoz and DeJong (2012)] ..	19
Figure 2.6 Different models of flexible rocking structure; (a) Acikgoz and DeJong (2012); (b) Ma (2010a); (c) Truniger et al. (2014) .....	20
Figure 2.7 “Stepping” reinforced concrete bridge pier [from Beck and Skinner (1974)] .....	21
Figure 2.8 Elevation view of the 5 storey prototype [from Priestley et al. (2000)].....	23
Figure 2.9 Moment frame with rocking wall [after Wada et al. (2009)] .....	24
Figure 2.10 Sketch of rocking bridge column and ideal force-deformation response [from Mander and Cheng (1997)] .....	25
Figure 2.11 Finite element model of the wall-frame prototype [from Ajrab et al. (2004)] .....	27
Figure 2.12 Proposed PT steel moment connection [from Ricles et al. (2001)].....	29

Figure 2.13 Proposed limit states, performance levels and seismic hazard intensities [after Roke et al. (2006)].....	30
Figure 2.14 Base Plate Yielding (BPY) system [from Midorikawa et al. (2006)] .....	31
Figure 2.15 Viscously damped rocking braced frame [from Tremblay et al. (2008a)] .....	33
Figure 2.16 Controlled rocking with replaceable energy dissipating fuses [from Hajjar et al. (2008)].....	35
Figure 2.17 Fuse configurations [from Ma et al. (2010a)] .....	35
Figure 2.18 South Rangitikei Rail Bridge with a close up of the rocking piers [from Ma (2010a)] .....	36
Figure 2.19 Kilmore Street Medical Centre [from Latham et al. (2013)].....	37
Figure 2.20 Proposed lateral load profiles [after Eatherton and Hajjar (2010)] .....	40
Figure 2.21 Storey shear distribution envelope [after Ma (2010b)] .....	41
Figure 3.1 Two degrees-of-freedom representation of a CR-CBF .....	48
Figure 3.2 (a) Local force-deformation response of <i>Frame</i> ; (b) Local force-deformation response of <i>PT</i> ; (c) Global force-deformation response of ( <i>Frame+PT</i> ).....	50
Figure 3.3 Local force-deformation response of ED .....	50
Figure 3.4 System force-deformation response of CR-CBF.....	51
Figure 3.5 Concept of Equivalent Energy Design Procedure (EEDP) .....	54
Figure 3.6 Limit states and performance levels of a CR-CBF.....	54
Figure 3.7 Energy modification factor $\gamma_a$ [plots from Yang et al. (2016)].....	57
Figure 3.8 Energy modification factor $\gamma_b$ [plots from Yang et al. (2016)].....	59
Figure 3.9 (a) Preliminary 3-storey CR-CBF configuration, (b) FBD of upper portion of frame, (c) FBD of joint B, (d) FBD of joint D, (e) FBD of joint G and (f) FBD of joint I .....	64

Figure 4.1 (a) Floor plan and (b) Elevation of the 3-storey and 6-storey CR-CBF prototypes ....	67
Figure 4.2 Proposed connections between gravity frame and controlled rocking frame[from Eatherton and Hajjar (2010)] .....	69
Figure 4.3 Design acceleration spectra for Berkeley, USA .....	71
Figure 4.4 EEDP force-deformation backbone of 3-storey CR-CBF prototype.....	73
Figure 4.5 Final layout of 3-storey CR-CBF prototype.....	74
Figure 4.6 EEDP force-deformation backbone of 6-storey CR-CBF prototype.....	75
Figure 4.7 Final layout of 6-storey CR-CBF prototype.....	76
Figure 4.8 Schematic representation of finite element model of CR-CBF.....	79
Figure 5.1 Response spectra of scaled ground motions for (a) 3-storey and (b) 6-storey prototype .....	82
Figure 5.2 Normalized median forces in (PT) and (ED) due to various seismic hazard intensities .....	84
Figure 5.3 Peak displacements in (a) 3-storey and (b) 6-storey prototype under SLE seismic hazard intensity.....	85
Figure 5.4 Peak displacements in (a) 3-storey and (b) 6-storey prototype under DBE seismic hazard intensity.....	85
Figure 5.5 Peak displacements in (a) 3-storey and (b) 6-storey prototype under MCE seismic hazard intensity .....	86
Figure 5.6 Peak median ISDR and base rotation in (a) 3-storey and (b) 6-storey prototype under all three seismic hazard intensities.....	87
Figure 5.7 Comparison of median and target roof drift ratios of (a) 3-storey and (b) 6-storey prototype under various seismic hazard intensities .....	88

Figure 5.8 IRDRs of (a) 3-storey and (b) 6-storey prototype under MCE seismic hazard intensity .....	89
Figure 5.9 Final design layout of 3-storey and 6-storey BRBF prototypes .....	90
Figure 5.10 Median of peak displacements in (a) 3-storey and (b) 6-storey BRBF prototypes under all three seismic hazard intensities.....	92
Figure 5.11 Comparison of median of peak floor accelerations in (a) 3-storey and (b) 6-storey CR-CBF and BRBF prototypes under all three seismic hazard intensities .....	94
Figure 5.12 Comparison of median IRDRs of 3-storey and 6-storey CR-CBFs and BRBF prototype under MCE seismic hazard intensity .....	95
Figure 6.1 FEMA P695 (ATC 63) collapse safety assessment procedure (after Deierlein et al. (2008)).....	100
Figure 6.2 Seismic performance factors (from FEMA P695 (2009)).....	101
Figure 6.3 Pushover curves for (a) 3-storey and (b) 6-storey CR-CBF prototypes .....	103
Figure 6.4 IDA curves for (a) 3-storey and (b) 6-storey CR-CBF prototypes.....	107
Figure 6.5 Collapse fragility curves for (a) 3-storey and (b) 6-storey CR-CBF prototypes.....	108

## List of Symbols

$E_a$	:	Strain energy
$E_s$	:	Elastic strain energy
$E_h$	:	Hysteretic strain energy
$R$	:	Response modification factor
$I$	:	Importance factor
$\gamma$	:	Energy modification factor
$\Delta_y$	:	Yield drift ratio of EPP-SDOF/ NLSDOF
$\Delta_e$	:	Elastic drift ratio of E-SDOF/ LSDOF
$\Delta_u$	:	Ultimate drift ratio of EPP-SDOF/ NLSDOF
$V_e$	:	Elastic base shear of E-SDOF/ LSDOF
$V_y$	:	Yield base shear of EPP-SDOF/ NLSDOF
$T$	:	Fundamental time period of the structure
$g$	:	Gravitational constant
$S_a$	:	Spectral acceleration (in units of g)
$\mu_s$	:	Structural ductility factor
$R_\mu$	:	Ductility reduction factor
$W$	:	Seismic weight of the structure
$\theta_p$	:	Plastic inter-story drift ratio
$\beta_i$	:	Normalized shear distribution with respect to top story shear
$\lambda_i$	:	Normalized equivalent lateral force at $i^{th}$ storey with respect to base shear

$F_i$	:	Normalized equivalent lateral force at $i^{th}$ storey
$F_{PT,0}$	:	Initial PT pre-tensioning force
$d_{PT}$	:	Lever arm of PT from rocking toe
$F_{ED}$	:	ED yield/slip load
$d_{ED}$	:	Lever arm of ED from rocking toe
$V_u$	:	Ultimate base shear of NLSDOF
$\Delta_p$	:	Plastic drift ratio of NLSDOF
$C_0$	:	MDOF displacement modification factor
$\gamma_a$	:	Energy modification factor of NLSDOF from $\Delta_y$ to $\Delta_p$
$\gamma_b$	:	Energy modification factor of NLSDOF from $\Delta_p$ to $\Delta_u$
$V_{PR}$	:	Distributed base shear of primary SFRS
$V_{SE}$	:	Distributed base shear of secondary SFRS

## List of Abbreviations

CR-CBF	:	Controlled rocking- concentrically braced frame
SFRS	:	Seismic force resisting system
MRF	:	Moment resisting frame
CBF	:	Concentrically braced frame
EBF	:	Eccentrically braced frame
BRBF	:	Buckling-restrained braced frame
PBPD	:	Performance-based plastic design
EEDP	:	Equivalent energy-based design procedure
E-SDOF	:	Elastic- single degree of freedom structure
EPP-SDOF	:	Elastic perfectly plastic- single degree of freedom structure
LSDOF	:	Linear- single degree of freedom structure
NLSDOF	:	Nonlinear- single degree of freedom structure
MDOF	:	Multiple degree of freedom structure
PT	:	Post-tensioning element
ED	:	Energy dissipating element
PBEE	:	Performance-based earthquake engineering

## Acknowledgements

This thesis is a culmination of guidance and support from numerous people. Space constraint allows me to name only a few but my sincere gratitude goes out to everyone I interacted within the course of this research.

Firstly, I am ever so grateful to my supervisor, Dr. Tony Yang for always encouraging me to be a good researcher, patiently letting me commit mistakes and learn from them. Words fail me to thank him enough. This work wouldn't have been possible without his sheer conviction and love for the subject. His quality of always willing to help will continue to inspire me. His knowledge and experience gave a fresh perspective for the betterment of the thesis, by pointing out avenues that needed further examination.

I would also like to thank all the members of my research group, especially Dorian Tung and Yuanjie Li for the countless hours of fruitful discussions that helped me along the way. Their selfless contribution in letting me use their data is immensely appreciated.

Last but certainly not the least, I want to express my deepest regard for my parents for all the sacrifices they made to ensure that I got what I desired. I would like to give a big shout out to my brother VJ for helping me keep my sanity and inspiring me to never give up. I hope my family continues to stand by me and bless me in all my future endeavors.

## **Dedication**

*To my beloved family*

# Chapter 1: Introduction

## 1.1 Motivation

The aftermath of events such as the 2011 Canterbury earthquake and 2011 Tohoku earthquake resulted in a combined direct economic loss of \$240 billion USD (Berger et al. 2012). This translates to 9% and 4% GDP (Gross Domestic Product) for New Zealand and Japan, respectively (Mahul and White 2012). In recent years, rapid urbanization has led to the concentration of large population and infrastructure growth in the major cities, which are also seismically active regions. This situation poses a great seismic risk to life and economy (Bilham 2009). To minimize the seismic risk and to improve earthquake resiliency, new and innovative earthquake resilient systems and design methodologies need to be developed.

## 1.2 Background

Earthquakes feed large energy into the structure. The modern seismic codes recognize that elastic design of the structures for such large forces may be highly uneconomical. Hence, the structure are designed in a ductile manner by using force-reduction factor like  $R$  in ASCE/SEI 7-10 (2010) and  $R_d \times R_o$  in NBCC (2010). These factors are vaguely selected based on the engineering judgment. By using these force reduction factors, the maximum seismic design forces are arbitrarily capped. In the event of strong earthquake shaking, the code-based designs need to sustain the earthquake energy through inelastic deformation. This design philosophy succeeds in saving human lives by focusing on collapse prevention under the maximum credible earthquake, but fails to quantify the post-disaster performance of structures. This often leads to unpredictable and uncontrolled damage, resulting in hefty financial losses. In some severe cases, the structures

maybe uninhabitable and disrupts its service function. In the 1995 Hyogoken-Nanbu earthquake, about 240,000 buildings were left in a partial state of collapse which clearly indicate the existing seismic force-resisting systems (SFRS) design is not capable of high speed recovery post disaster (Architectural Institute of Japan 1998).

### **1.2.1 Residual Displacements**

Iwata et al. (2006) investigated the buildings damaged during the 1995 Hyogoken-Nanbu earthquake. They attributed the accumulation of high residual deformations in the systems to their poor performance during the earthquake. Considering the economic feasibility, they also proposed reparability limits based on residual deformations. In fact, many researchers concur with the fact that residual deformations should be considered as a crucial design parameter when making project feasibility decisions (Christopoulos and Pampanin 2004; McCormick et al. 2008; Wang et al. 2008). Most of these studies recommend a residual drift ratio less than 0.5%, which is calculated based on construction tolerances, functionality and safety of occupants.

Many researchers have even investigated the seismic performance of conventional code-approved SFRS presented in ANSI/AISC 341-10 (2010) and their propensity to accumulate residual deformations. Erochko et al. (2010) analyzed various configurations of buildings with steel moment resisting frames, between two and twelve stories, designed in accordance with the requirements of ASCE/SEI 7-10 (2010). Nonlinear time history analyses for earthquakes scaled to DBE seismic hazard level revealed the extent of residual displacements in the structure to be as high as 1.2%. Tremblay et al. (2008b) showed that median residual drift in buildings with Buckling Restrained Braced Frames subjected to DBE scaled ground motions can be as high as 1.4%. Figure

1.1 shows the code-intended mode of inelasticity in (a) moment resisting frames and (b) concentrically braced frames, ultimately resulting in residual deformations.

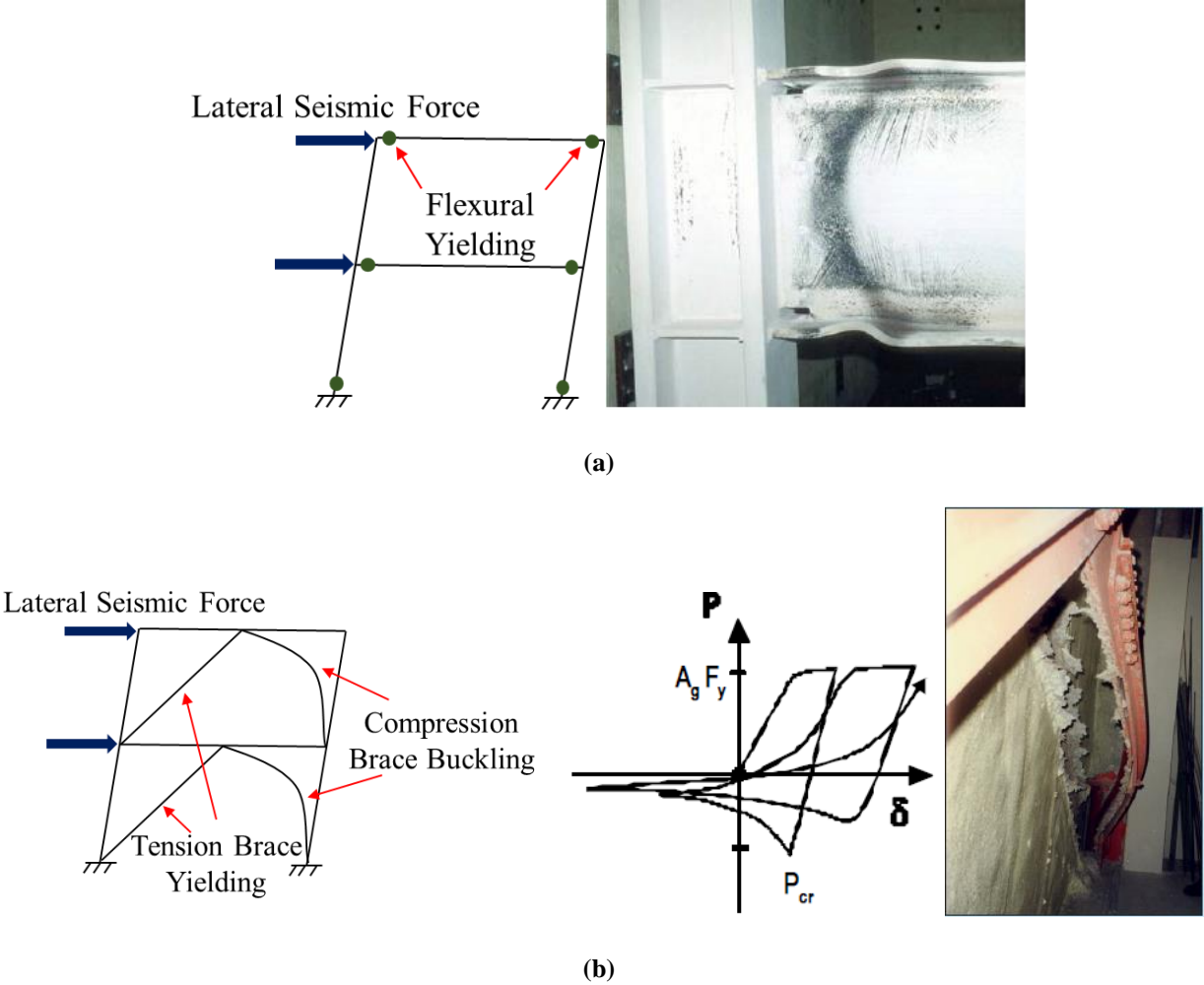


**Figure 1.1 Mode of inelasticity in (a) steel moment resisting frame [from Hamburger et al. (2008)] and (b) steel concentrically braced frame [from (Sabelli 2001; Sabelli et al. 2013)]**

Thus, the shortcomings in the performance of structures designed in accordance to the existing building codes clearly point to the grave need of improved design methodologies, wherein retention of life safety is a necessary but not sufficient criteria. There is a need to be able to quantify structural damage at all intensities of earthquakes, thereby limiting the direct economic losses to

the minimum. All these factors motivated researchers to develop the concept of performance-based seismic engineering.

### **1.2.2 Performance-Based Seismic Engineering**

The Structural Engineering Association Of California published the Vision 2000 report (SEAOC 1995), which was the earliest attempt to introduce a design framework wherein structural performance at varying intensity of earthquakes was quantified by relating it to a specific performance target. The American Society of Civil Engineers readily adopted this design criteria in their document ASCE/SEI 41-06 (2007). This standard defines the performance targets corresponding to different intensities of ground shaking as:

- (i) Immediate Occupancy (IO) performance level corresponding to a lower intensity, frequent earthquake (referred to as Service Level Earthquake or SLE) with a probability of exceedance 50% in 50 years.
- (ii) Life Safety (LS) performance level corresponding to a medium intensity, rare earthquake (referred to as Design Basis Earthquake or DBE) with a probability of exceedance 10% in 50 years.
- (iii) Collapse Prevention (CP) performance level corresponding to a severe intensity, very rare earthquake (referred to as Maximum Considered Earthquake) with a probability of exceedance 2% in 50 years.

This is clearly demonstrated by a performance-matrix as shown in Figure 1.2. Adopting this rigorous exercise of designing the structures for a combination of different hazard intensities under strict performance targets gives the structural designers much confidence in the performance of the structure throughout its lifetime. Additionally, this approach also caters to the stakeholders'

choice of the intended performance of their buildings, in terms of cost of repair, downtime, risk of collapse or even fatalities, in the design inception stage itself.

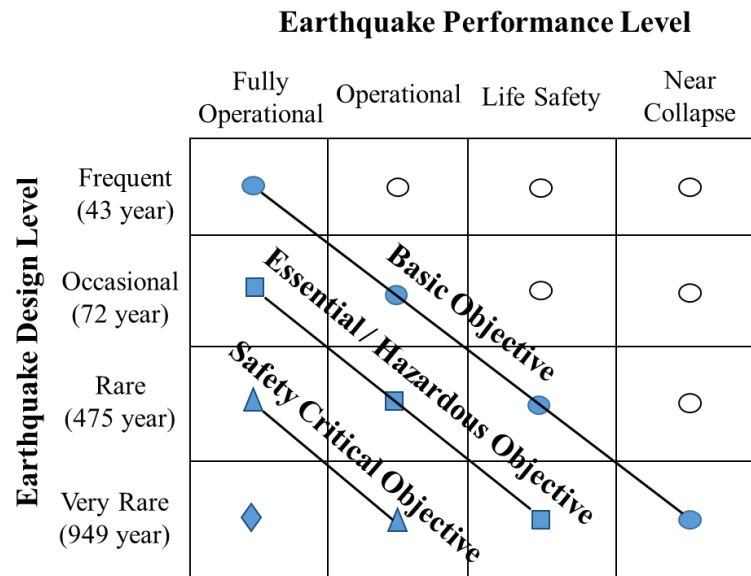


**Figure 1.2 Vision 2000 recommended seismic performance matrix [after SEAOC (1995)]**

This intrinsic shift in the focus towards a more resilient design through performance-based seismic design called for novel SFRS which could successfully incorporate the various performance levels explained so far. In pursuit of such high performance systems, researchers developed a class of next generation SFRSs called controlled rocking systems.

### 1.2.3 Controlled Rocking Systems

Controlled Rocking Systems (CRSs) are novel SFRSs that sought to alleviate the deficiencies pointed out in the conventional SFRSs discussed in Section 1.2.1. Much like the conventional systems, CRSs also exhibit nonlinear response which limits the peak forces that the structure is subjected to. However, unlike the conventional systems, CRSs have a greater ability to eliminate

residual deformation at the end of the seismic shaking. CRSs usually comprise of a restoring force component through a nonlinear gap-opening mechanism and an energy dissipating device acting in parallel which creates a controlled rocking mechanism at the base of the structure. The result of their combined response is a flag-shaped hysteresis which results to almost zero deformation when the external applied force is withdrawn. On the other hand, the conventional SFRS usually elicit a bilinear plastic response and thus are vulnerable to high residual deformations. Figure 1.3 shows the difference in the hysteresis for the conventional and CRSs. Previous experimental and numerical studies by Christopoulos et al. (2002) and Eatherton and Hajjar (2011) have shown that the CRSs and self-centering systems can have similar or even lesser peak displacements when compared to that of the conventional SFRS. This shows that the viability of using the CRSs to minimize damage and reduce the repair cost.

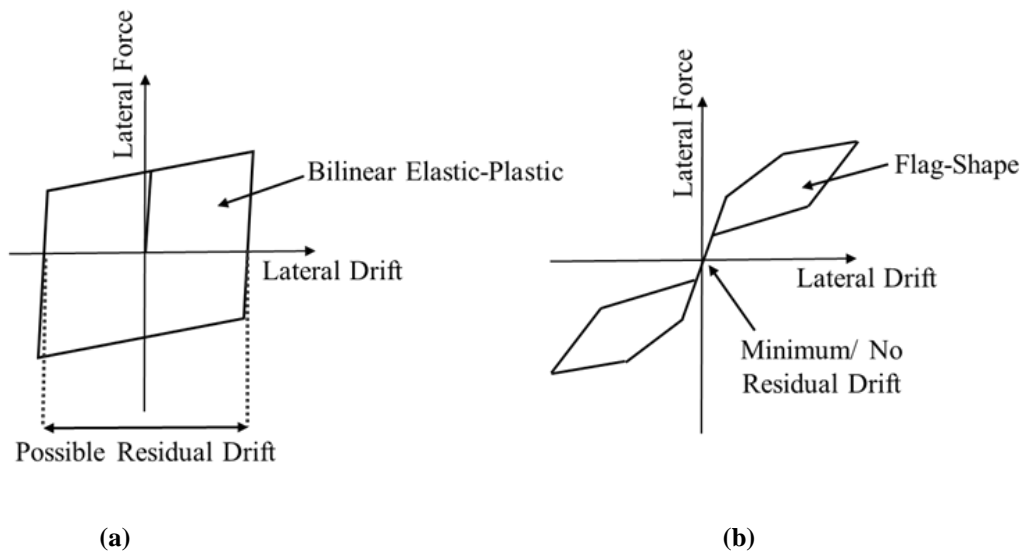


**Figure 1.3 Seismic response of (a) Conventional SFRS and (b) Controlled Rocking SFRS**

### 1.3 Objectives

Controlled rocking mechanism can be achieved by upgrading a variety of conventional SFRSs such as concrete shear wall, steel moment resisting frame and steel trusses in bridge piers. A comprehensive literature review of these systems will follow in Chapter 2. This thesis focusses on a new configuration of CRSs, named steel Controlled Rocking-Concentrically Braced Frames (CR-CBFs). As the name suggests, CR-CBF is a self-centering CBF which is capable of achieving superior performance through controlled rocking mechanism. As shown in Figure 1.6, CR-CBF has three major components:

- (i) ***Supplemental energy dissipating devices (ED)***: This is used as the primary structural fuses which is designed to yield and dissipate excess seismic energy and safeguarding rest of the structure by limiting the force applied to the structure. In this study, ED is a friction damping device capable of sustaining multiple cycles of ground shaking without any significant strength degradation. They are placed at the column bases, where they are easily accessible for inspection, repair or replacement without any hindrance to building's functionality.
- (ii) ***Vertical un-bonded post-tensioning tendons (PT)***: These are used to control the load at which uplift of frame initiates and also provides positive stiffness to the system post uplift. The PT is largely responsible for providing the restoring force and self-centering ability to the frame at the low earthquake shaking intensities. The PT can be designed to yield at higher seismic intensities, so it can act as secondary SFRS and contribute to energy dissipation along with the ED. After the earthquake, the yielded PT can be repaired by re-tensioning or replaced.
- (iii) ***Braced frame members***: These include the beams, columns and braces which shall essentially remain elastic, even at the highest hazard level. The column bases should be

equipped with specially designed bumpers that transfer base shear while allowing column uplift without any sliding.

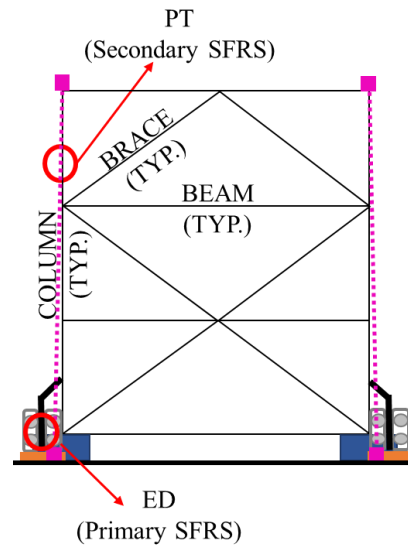


**Figure 1.4 Controlled Rocking- Concentrically Braced Frame (CR-CBF)**

To efficiently design such high performance fused structural systems, a robust performance-based Equivalent Energy-based Design Procedure (EEDP) was developed by Yang et al. (2016). In this study, EEDP is adopted and modified to design CR-CBFs. Unlike the existing design methodologies for controlled rocking systems, discussed in Chapter 2, EEDP doesn't require the assumption of response modification factors or the fundamental period of the structure. Next, two prototype office buildings in downtown Berkeley, California, are designed to demonstrate the application of EEDP. Detailed finite element models are developed in OpenSees (2010) to examine the seismic performance of these prototypes. These models are then subjected to a suite of ground motions scaled to different earthquake intensities. Thereafter, the seismic performance of EEDP designed CR-CBFs are compared to that of the conventional code-designed BRBFs. Finally, to

conclusively validate EEDP for design of CR-CBFs, the earthquake collapse safety is evaluated using FEMA P695 (2009) methodology, to ensure life safety is retained after a major earthquake.

#### **1.4 Organization of Thesis**

This thesis is divided into the following chapters:

*Chapter 2* presents detailed literature review that tries to gather all the research developments pertaining to controlled rocking systems, with a special focus on steel systems. This chapter also summarizes the existing design methodologies for controlled rocking systems.

*Chapter 3* introduces energy based design procedure and summarizes the Performance-Based Plastic Design (PBPD). Finally, EEDP is explained through its application in the design of CR-CBFs.

*Chapter 4* demonstrates various prototype design of buildings with CR-CBFs, using EEDP. Subsequently, finite element model development and validations are explained.

*Chapter 5* presents the results of the seismic assessment of the model prototypes through nonlinear dynamic analysis. The chapter discusses the hazards chosen which would be used to select and scale ground motions used in the analysis. The performance of the CR-CBFs is also compared with that of the conventional BRBFs.

*Chapter 6* presents a brief overview of the FEMA P695 (2009) methodology for collapse safety assessment and applies it to evaluate the collapse performance of CR-CBFs.

*Chapter 7* presents the summary of research findings, important conclusions and scope for future studies.

## Chapter 2: Literature Review of Rocking Systems

This section presents a comprehensive literature review of the research work undertaken related to the development of rocking systems. Section 2.1 and 2.2 discuss the mechanics of rocking structures through the various existing analytical models. Section 2.3 deals with the implementation and development of controlled rocking systems using different construction materials (steel, concrete, etc.) and SFRS (shear wall, frame, etc.). Section 2.4 highlights the various buildings which employ controlling rocking mechanism as a system to resist lateral loads. Section 2.5 discusses the various existing design procedures for controlled rocking frames. Finally, Section 2.6 summarizes the literature review, highlighting the need for an alternative design methodology for CR-CBF.

### 2.1 Early Studies of Rocking Structures

The concept of rocking has intrigued the scientific community for decades. All the modern studies dealing with the mechanics of rocking structures derive their inspiration from the pioneering study by Housner (1963). During the Chilean Earthquake in 1960, a number of tall and slender structures survived the impact, while other more stable looking structures incurred severe damage. Housner conducted a study of these '*inverted pendulum*' type rigid blocks, subjected to free- and forced- vibration (rectangular and half-sine pulse excitations) as well as earthquake excitations, showing their inherent complex non-linear behavior which is quite different from linear elastic structures. Piecewise second-order differential equations of motion, for rigid rocking block, shown in Figure 2.1, were derived for the rotational degree of freedom using Newton's Second Law of Motion:

$$I_0 \ddot{\theta} = \begin{cases} -mgR \cdot \sin(\alpha - \theta) & \theta < 0 \\ mgR \cdot \sin(\alpha + \theta) & \theta > 0 \end{cases} \quad [2.1]$$

where  $I_0$  is the moment of inertia of the rocking block,  $\theta$  is the rocking angle,  $m$  is the mass,  $g$  is the acceleration due to gravity,  $R$  is the distance from rocking edge to the center of mass and  $\alpha$  is the slenderness coefficient.

Solution of Equation [2.1] for free-vibration motion with initial conditions  $\theta = \theta_0$  and  $\dot{\theta} = 0$  at  $t = 0$  was then used to derive a simplified expression for amplitude dependent time-period of these rocking blocks. This is represented by Equation [2.2]. For energy dissipation during rocking, a stereo-mechanical impact framework was assumed in which the impact of the base with the foundation is instantaneous, inelastic (no bounce) and used conservation of momentum principle to modify the angular velocity after the impact. A coefficient of restitution,  $r$  was evaluated as shown by Equation [2.3].:

$$T = \frac{4}{\sqrt{mgR/I_0}} \cosh^{-1} \left( \frac{1}{1 - \theta_0/\alpha} \right) \quad [2.2]$$

$$r = \left[ 1 - \frac{mR^2}{I_0} (1 - \cos 2\alpha) \right]^2 \quad [2.3]$$

Housner (1963) concluded by pointing out that the propensity of a slender block to overturn is inversely proportional to the square root of its size, due to scale effect. Hence, this explained why relatively taller structures were able to survive strong ground motion.

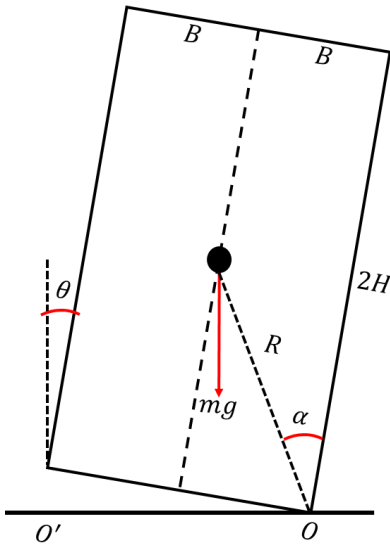


**Figure 2.1 Housner's rigid rocking block [after Housner (1963)]**

The theory established by Housner (1963) was extended further by Priestley et al. (1978). They recognized that provisions in the New Zealand seismic design code NZS 4203:1976 (S.A.N.Z 1976) implicitly resulted in rocking of part or all of the structure, which can be of advantage in some situations. An equivalent linear SDOF viscous representation of the rocking structure was proposed. This was derived by equating the free vibration decay of rocking block from Housner's work with that of a linear viscous damped oscillator. An empirical formula was proposed to estimate the equivalent viscous damping ratio of the rocking block ( $\beta$ ), as a function of ( $r$ ) from Equation [2.3]. This is represented by Equation [2.4]. The maximum rocking displacement was then estimated using displacement response spectra. Priestley et al. (1978) also performed limited shake-table testing to successfully verify both Housner's equations as well as the theory proposed by them. This methodology has been adopted in FEMA 356 document: *Prestandard and Commentary for the Seismic Rehabilitation of Buildings* (FEMA 2000).

$$\beta = -0.34 \ln(r) \quad [2.4]$$

However, Makris and Konstantinidis (2003) later point out flaws in the basic assumptions of the study by Priestley et al. (1978). The study shows how a linear SDOF oscillator (regular pendulum) and a rocking block (inverted pendulum) are dynamically different and thus the response of one system cannot provide a measure of response of the other system. Therefore, the FEMA procedure assumes simplification of rocking structure to a SDOF oscillator with a constant fundamental period and constant viscous damping, which is flawed and needs to be modified. In addition to the response spectrum, this study proposes the use of rocking spectrum shown in Figure 2.2 stating that “*rocking spectrum reflects kinematic characteristics of ground motion that are not identifiable by response spectrum*”.

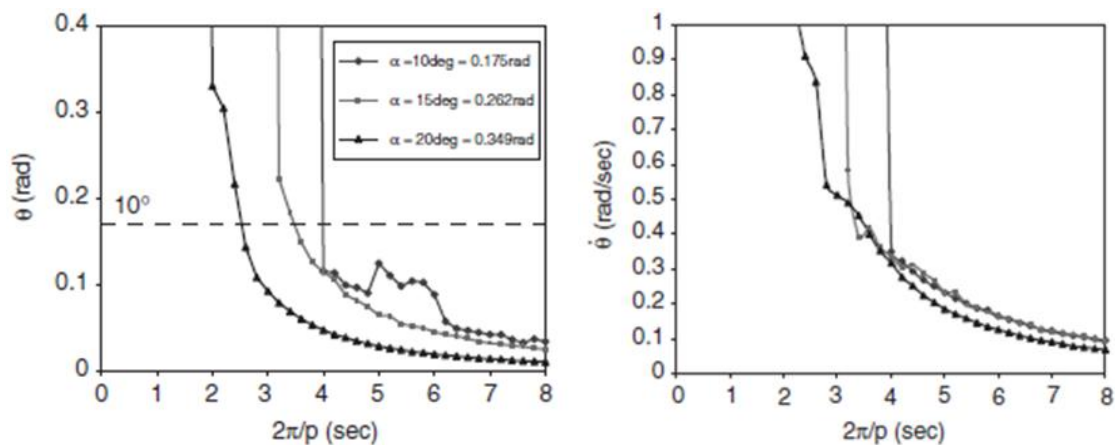


**Figure 2.2 Rocking spectrum [plots from Makris and Konstantinidis (2003)]**

Aslam et al. (1980) developed a numerical model to predict the rocking and overturning behavior of a rigid rocking block when subjected to a combination of vertical and horizontal ground accelerations. The validity of the mathematical model was bolstered by conducting free-vibration and forced-vibration experimental tests on physical prototype. Various blocks with different aspect ratios were then analyzed using the model to study the effect of varying different

parameters (boundary condition, coefficient of restitution at impact, ground motion characteristics, etc.) on the rocking behavior. Finally, this study also investigated the effect of vertically prestressing the block to the foundation. It was observed that the block overturned in the absence of the vertical restraint when subjected to a strong earthquake excitation (Pacoima Dam S16E). However, the vertical prestressing rod prevented overturning of the block by complimenting the self-weight in providing restoring force. The prestressing rod was attached to the ground at the center with the end condition assumed to be hinged. It was also assumed that the rod shall remain elastic, with an initial prestressing force equal to 40% of the block weight and stiffness of 40% of the block weight per inch. Hence, this study was the earliest attempt at exploring the benefits of vertical prestressing in controlling the dynamic response of rocking blocks to prevent overturning.

## **2.2 Flexible Rocking Structures**

Although the investigation of rigid rocking systems was successful, this idealization ignored two crucial considerations: 1) structural flexibility and 2) soil-structure interaction. Numerous studies later realized that these factors had a considerable bearing on the dynamic response of structures in the event of severe ground shaking. Rutenberg et al. (1980) studied the evidences of partial uplifting of the Veterans Hospital Building 41 during the San Fernando earthquake. The original building was designed for lateral loads of only 10% of the building weight, while the earthquake was strong enough to probably induce lateral loads of more than 50% of building weight. However, the building only experienced minor structural damage, indicating no significant inelastic behavior in the crucial structural components. Rutenberg et al. (1980) performed nonlinear dynamic analysis on models with the nonlinearity occurring due to partial uplift of the structure and soil-structure interaction. The findings of this study indicated that the structure

experienced lower shear forces and moments due to the beneficial effects of soil-structure interaction. The first attempt at investigating the dynamic behavior of flexible rocking structures was the experimental study by Muto et al. (1960) on a single mass attached through a flexural member to a rigid and flexible foundation. They investigated the criteria for overturning under dynamic loads. It was determined that the amplitude of ground motion required to overturn the model is proportional to the ratio of width of base to the height of the structure. They also proposed a 'law of similarity' by which the observations from the model could be extended to the actual structures. In the context of multi-storey frames, Clough and Huckelbridge (1977) tested a three-storey frame, as shown in Figure 2.3. The column was untyed at the base and framed into the foundation base through a pin, with guiding rollers which allowed vertical translation of the column. The bases of the columns were perfectly cushioned with impact pads made of neoprene and steel plates. Tests were conducted to study the variation in the response of a conventional fixed-base frame from a rocking frame. The results confirmed greater displacements but much lesser accelerations and member forces in case of the rocking frames. The influence of stiffness of the neoprene pads and inclusion of vertical ground motions was seen to be negligible on the global response.

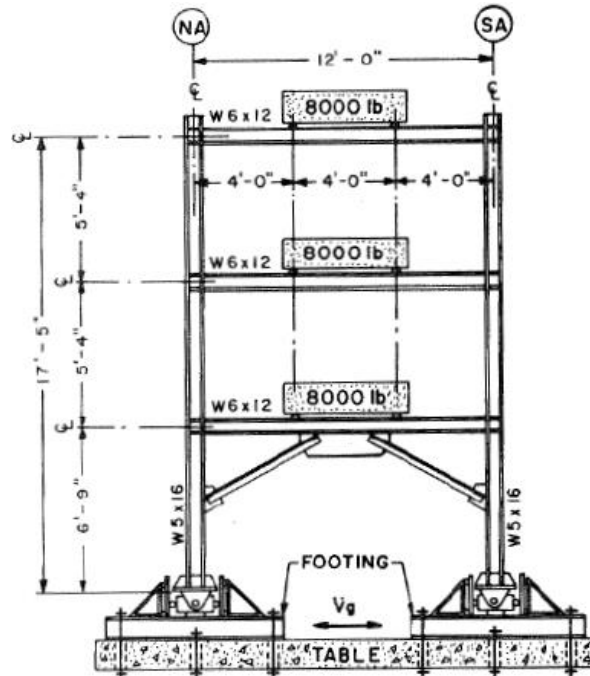
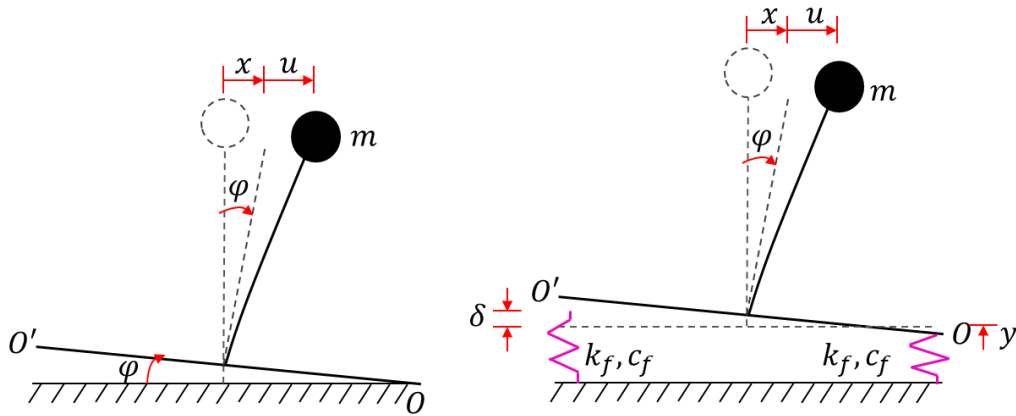


Figure 2.3 Three-storey rocking frame prototype [from Clough and Huckelbridge (1977)]

Expanding on the work of Muto et al. (1960), Meek (1975) used the models to reveal the beneficial effect of foundation tipping in reducing the transverse displacements in the structure. Later, Meek (1978) also investigated braced core multi-storey buildings and concluded that tipping greatly reduces the base shear and moment, offering a favorable design. Yim and Chopra (1985) studied multi-storey structures on two different types of foundation, i.e. two-spring type and multiple-spring Winkler type. The authors developed a simplified procedure for reasonably estimating the maximum earthquake induced forces and deformations in the structure using earthquake response spectrum. This was followed by a similar study by Psycharis (1991) in which the effect of base uplift on the maximum response of a SDOF structure was explored. The study presented an empirical formulation for estimating the maximum earthquake deformation for flexible structures on rigid foundation, using classical response spectrum. The formulation could

be extended for the case of flexible foundation also, under certain considerations based on classical soil-structure interaction theory. Figure 2.4 shows the systems considered in the study. When compared with the procedure of Yim and Chopra (1985), this method was much more efficient, especially in short period ranges.



**Figure 2.4** Systems used for investigation, with rigid foundation (left) and flexible foundation (right) [after Psycharis (1991)]

More recently, Acikgoz and DeJong (2012) and Oliveto et al. (2003) examined the overturning stability of flexible rocking structures by accounting for large displacements in their formulation of the governing equations of motion. The interaction of structural elasticity and rocking response yielded a complex dynamic response. To avoid intricacy in geometry, researchers avoided Newtonian Mechanics and employed Lagrange's Formulation to form the governing equations of motion. The whole motion of the structure comprised of two phases, (i) full contact phase and (ii) rocking phase. As shown in Figure 2.5, the analytical model has a mass  $m$ , stiffness  $k$ , viscous damping coefficient  $c$  and the Lagrangian parameters are  $R$  and  $\beta$ . The governing equations of motion that were derived are as follows.

$$\ddot{u} + 2\zeta\omega_n\dot{u} + \omega_n^2u = -\ddot{u}_g(t) \quad [2.5]$$

$$\begin{aligned} \ddot{u} + 2\left(\frac{R_0}{B}\zeta\right)\left(\frac{R_0}{B}\omega_n\right)\dot{u} + \left(\frac{R_0}{B}\omega_n\right)^2u \pm \frac{R_0^2}{B}\left(\dot{\theta} + \frac{H\dot{u}}{R_0^2}\right)^2 \\ = \pm \frac{R_0}{B}\left(\ddot{u}_g \sin(\mp\alpha + \theta) + g \cos(\mp\alpha + \theta)\right) \end{aligned} \quad [2.6]$$

$$\ddot{\theta} + \frac{H}{R_0^2}\ddot{u} \mp \frac{2B}{R_0^2}\left(\dot{\theta} + \frac{H\dot{u}}{R_0^2}\right)\dot{u} = -\frac{1}{R_0}\left(\ddot{u}_g \cos(\pm\alpha - \theta) + g \sin(\pm\alpha - \theta)\right) \quad [2.7]$$

where  $\ddot{u}_g$  is the horizontal ground acceleration,  $\omega_n = \sqrt{k/m}$  is the natural frequency of the structure and  $\zeta = c/2\sqrt{k \cdot m}$  is the damping factor.

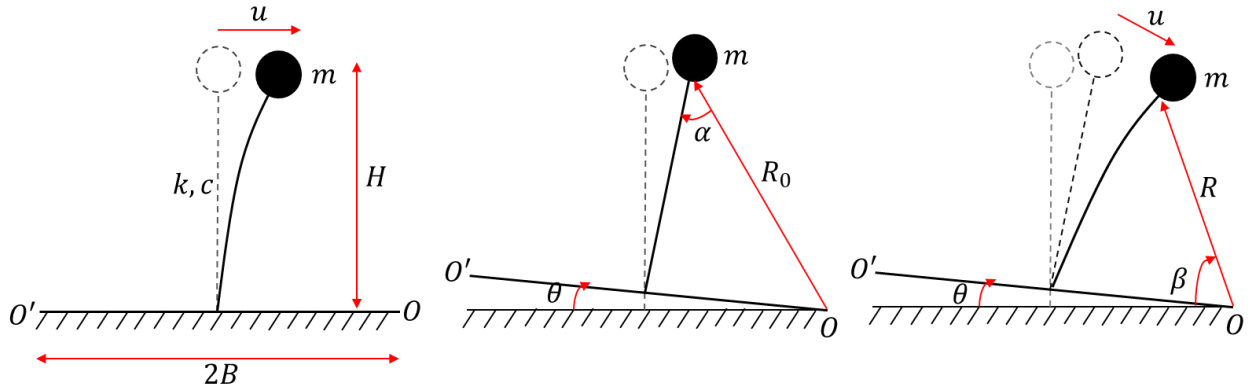


**Figure 2.5 Analytical model of flexible rocking structure [after Acikgoz and DeJong (2012)]**

As shown in Figure 2.5, all the mass of the structure has been assumed to be concentrated at the top while formulating the governing equations of motion. Subsequently, this model was subjected to further studies wherein researchers pointed to the inaccuracy of its results when compared with the experimental findings. Ma (2010a) in his doctoral research refined the former model by accounting for mass at the base as well, which was a better simulation of experimental results. Recently, Truniger et al. (2014) re-explored this model and further generalized it by also including

mass of the column, by treating it as a continuous dynamic system. Figure 2.6 shows the different flexible rocking structural models.

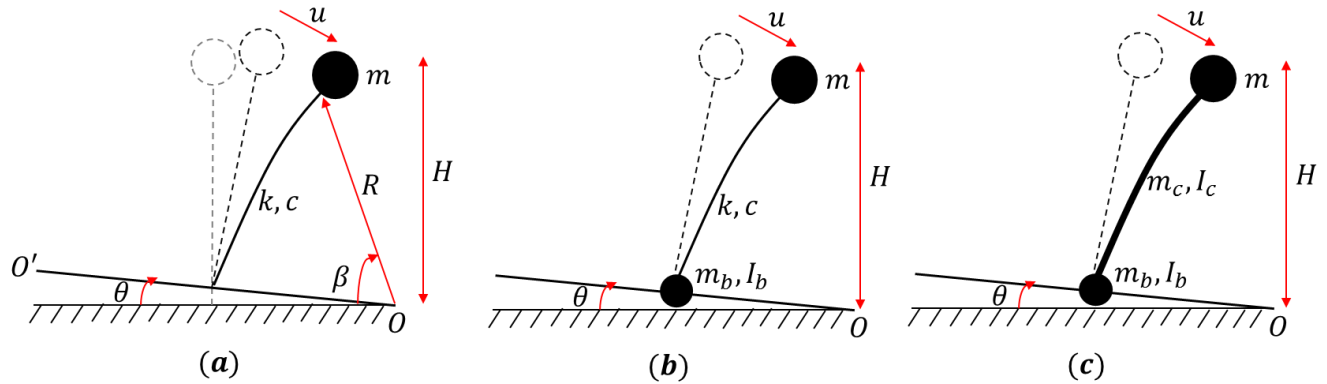
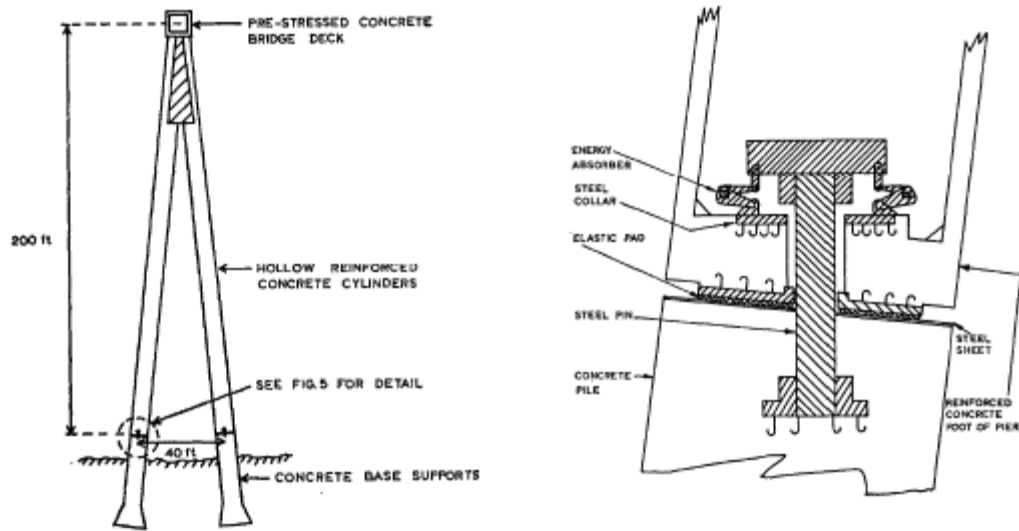


Figure 2.6 Different models of flexible rocking structure; (a) Acikgoz and DeJong (2012); (b) Ma (2010a); (c) Truniger et al. (2014)

## 2.3 Controlled Rocking System

### 2.3.1 Early Developments

Beck and Skinner (1974) conducted the earliest feasibility study of controlled rocking systems. As shown in Figure 2.7, an A-shaped reinforced concrete bridge pier was designed, with columns allowed to “step” in order to limit stresses below yield values and enhance its seismic resistance. A numerical model of a 200 feet tall pier was developed and nonlinear time history analysis was conducted using 1940 El Centro earthquake record. It was observed that for nominal viscous damping of about 3%, the peak displacement was considerably higher than an elastic fixed base structure. However, including the effects of supplemental energy-absorbing devices reduced the peak displacement, but still being slightly higher than the corresponding fixed-base structure.



**Figure 2.7 “Stepping” reinforced concrete bridge pier [from Beck and Skinner (1974)]**

Kelly and Tsztoo (1977) further examined the three storey uplifting frame proposed by Clough and Huckelbridge (1977), to study the effect of adding additional energy dissipating devices in them. Rectangular mild steel bars were employed which were subjected to plastic torsion when the frame uplifted from the foundation. Shaking table tests of the different variants of the frame, i.e. fixed-base, uplifting frame without additional energy dissipating devices and uplifting frame with the new energy dissipating devices were conducted. For one ground motion, the uplifting frame with the devices reduced the peak displacements to be similar to the fixed base frame, while limiting the internal forces in the structure as well. However, for another ground motion, the peak displacements of the uplifting frame with the devices was observed to be considerably higher than the other two variants. Hence, these tests were inconclusive about the effect of the inclusion of these devices.

### **2.3.2 Controlled Rocking Precast Concrete Wall**

The Precast Seismic Structural Systems (PRESSSS) Research Program was initiated as a joint research collaboration between US and Japan to conduct extensive experimental testing of precast concrete construction in seismic zones (Priestley 1991). The research aimed at developing design guidelines, connection detailing and technology that would foster acceptance of precast concrete construction for seismic applications. The traditional “strong connection” concept which ensured monolithic action between the precast components was difficult to achieve owing to the intricate detailing required. Hence, Priestley et al. (2000) explored four alternative types of ductile connections, which not only localized damage to the connections but were cheaper to repair after the earthquake as well. The different ductile frame systems tested were (a) Hybrid post-tensioned connection, (b) Pre-tensioned connection, (c) Tension-compression yielding gap connection and (d) Tension-compression yielding connection. The culmination of the 10-year long research program was a large scale testing of a 60 percent scale prototype of a five storey precast concrete building (shown in Figure 2.8) under simulated ground motions. The building design employed Direct Displacement Based Design procedure (Priestley et al. 2007), for a chosen target drift of 2% under design seismic intensity according to UBC (Uniform Building Code). The results were favorable with minimal damage, even at drifts reaching as high as 4.5%.



**Figure 2.8 Elevation view of the 5 storey prototype [from Priestley et al. (2000)]**

Wada et al. (2009) proposed a rocking wall system as a viable retrofit solution for reinforced concrete frames in Japan. As shown in Figure 2.9, the design scheme required strong rocking walls to be attached to the moment frames to control the displacement profile and thus suppress other unwanted failure modes like weak stories at intermediate stories. The rocking walls were pinned at the base to accommodate higher rocking displacements and supplemental steel dampers were installed to enhance the energy dissipating capacity of the building. To demonstrate the efficacy of this retrofit scheme, the seismic performance of the building before and after the retrofit was compared by conducting extensive nonlinear time history analyses. These analyses concluded that the retrofit technique was successful in predicting the mode of failure with much more certainty, hence leading to a performance-driven seismic design.

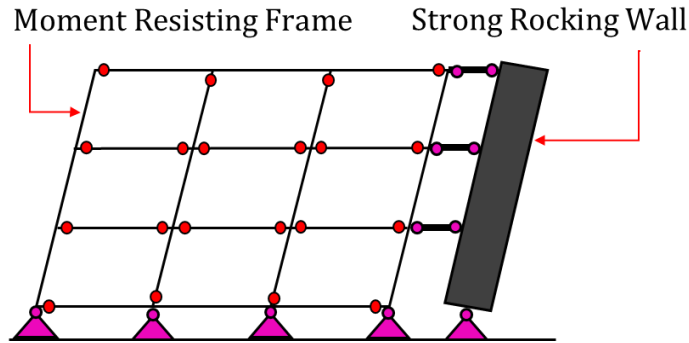
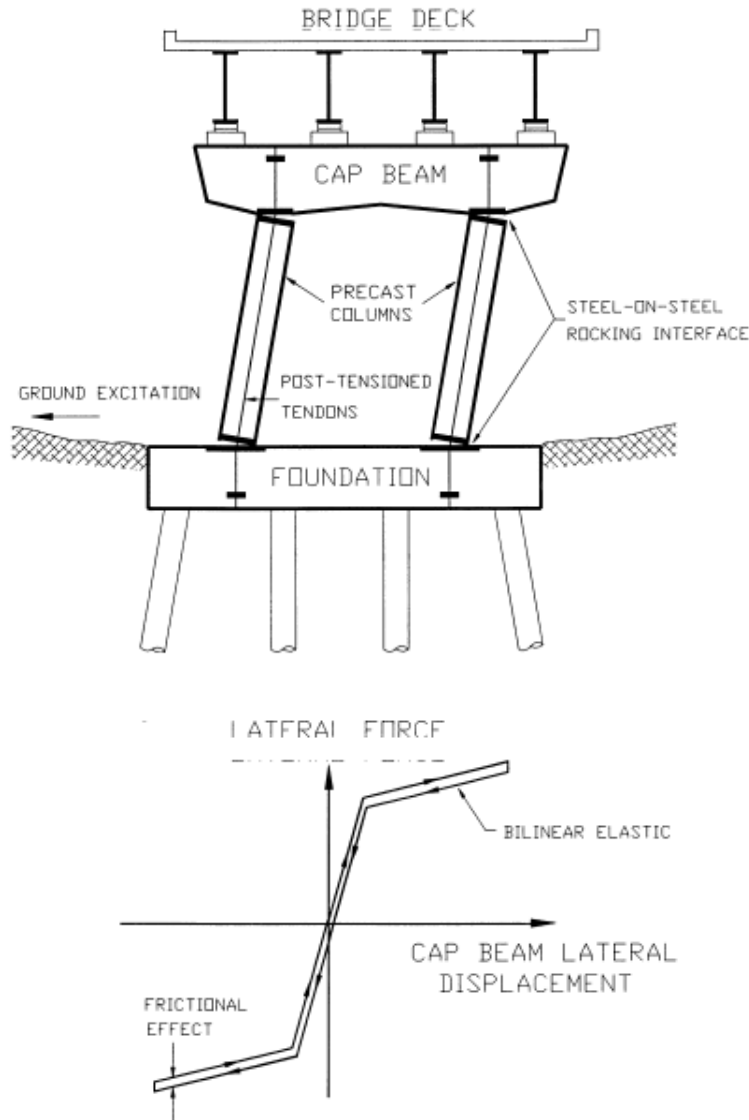


Figure 2.9 Moment frame with rocking wall [after Wada et al. (2009)]

### 2.3.3 Controlled Rocking Bridge Pier

Mander and Cheng (1997) explored the benefits of controlled rocking in bridge piers made up of modular (precast) beam and column elements. The individual columns were intentionally allowed to rock at the top and bottom edges, by discontinuing the vertical reinforcement bars in them. The only source of energy dissipation sought to control the peak displacement was the energy lost due to impact at the end of each rocking cycle. This energy loss was converted to an equivalent viscous damping based on Housner (1963). Vertical post tensioning was introduced to increase the lateral strength and also to provide additional energy dissipation on yielding. Figure 2.10 shows the sketch of the bridge pier column and its ideal force-deformation response. The authors summed up all these recommendations in a displacement-based design methodology called '*Damage Avoidance Design (DAD)*'. To validate the proposed methodology, a full scale precast concrete bridge column was designed and tested. Static tests confirmed the model verified the established kinematics of the rocking column, i.e. force-deformation response. Cyclic tests with large displacement demands were imposed and no damage to the column or foundation was observed.



**Figure 2.10 Sketch of rocking bridge column and ideal force-deformation response [from Mander and Cheng (1997)]**

More recently, Pollino and Bruneau (2007) presented a similar solution for retrofitting steel bridges. The truss piers were designed to allow rocking about its foundation, while displacement-based passive energy dissipaters such as buckling restrained braces were placed at uplifting locations to provide additional energy dissipation while controlling the peak response of the pier. The bridge relied completely on its self-weight to provide the required restoring force to ensure

self-centering was retained. Subsequently, a capacity-based design procedure for such structures was proposed. This design procedure aims to achieve a controlled ductile response through incorporation of several performance constraints like self-centering, demands on BRB and maximum force demands on the remaining structure. In a follow-up study, Pollino and Bruneau (2008) investigated the consequences of impact and uplift on the dynamic response of the pier. Simple linear-elastic mass-spring models were developed in the pursuit of quantification of the excitement of vertical modes of vibration which would amplify the axial force demand on the non-ductile elements. Methods to predict these dynamic amplification factors were proposed which were suitably verified by nonlinear time history analyses.

#### **2.3.4 Controlled Rocking Shear Wall**

Ajrab et al. (2004) proposed and implemented the concept of rocking shear walls for wall-frame structures. The rocking shear walls were designed using *DAD* (Mander and Cheng 1997), but with supplemental energy dissipation devices also installed. This study investigated the effect of various parameters on the structural performance and concluded that draped configurations of PT tendons are more effective than straight configurations to improve the inter-storey drift profile and beam-column rotations. Figure 2.11 represents the six storey prototype that was used to verify the design guidelines and also study the sensitivity of the different parameters on the overall response.

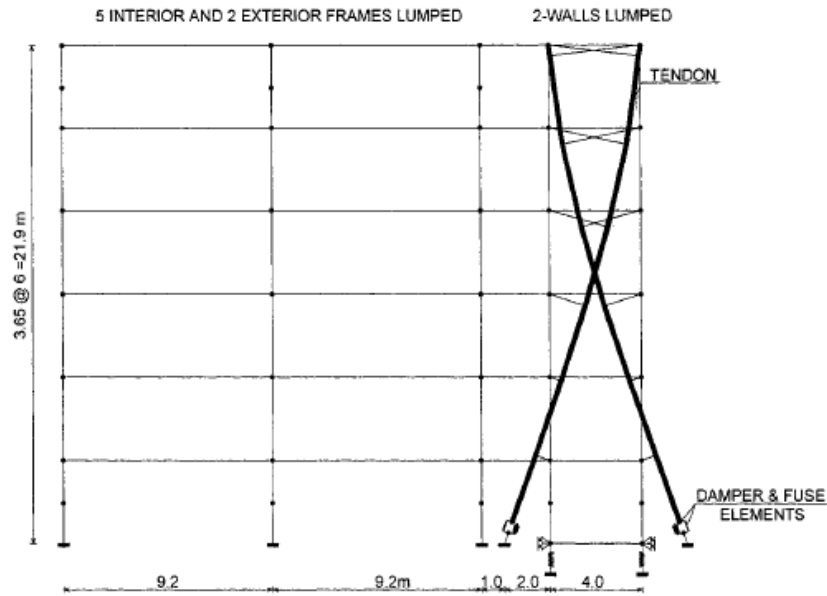


**Figure 2.11 Finite element model of the wall-frame prototype [from Ajrab et al. (2004)]**

Ozaki et al. (2010) exploited the controlled rocking mechanism to improve the seismic performance of steel plate shear walls. They developed a novel rocking multi-storied shear wall system with hold down fasteners which acted as energy dissipaters while the shear wall panels rocked. Statically loaded experiments were conducted to characterize the seismic performance of the different fuse specimens used. The fuse panels with butterfly shape and rhomboid slits were seen to have greater energy absorbing capacity than the ones with rectangular shape and rectangular slits. Furthermore, analytical models of the rocking shear wall system were developed and investigated using nonlinear time history analysis which demonstrated the successful reduction of drift angle and negligible residual drift in case of this novel system.

## **2.3.5 Controlled Rocking Steel Frame**

### **2.3.5.1 Self-Centering Concentrically Braced Frame**

Bolstered by the successful implementation of controlled rocking mechanism to various seismic force resisting systems, researchers started focusing on its application in steel frame systems. The study by Ricles et al. (2001) is considered the earliest attempts to incorporate the benefits of controlled rocking into steel moment frames. The research initially intended to develop new moment connections to tackle the brittle failure of connections in the pre-1994 Northridge earthquake moment frames. The new connection did not require field welding and utilized high strength steel post-tensioned strands placed horizontally along the beam. Friction at the contact surfaces provided shear resistance and the yielding of the seat-angles contributed to the energy dissipation at the connection while gap-opening mechanism occurred at the beam-column interface. Figure 2.12 shows the proposed connection called the PT steel connection. A corresponding numerical model of the connection was developed and analyzed to verify if it simulates the experimental results accurately. Finally, to confirm its application in buildings, a six storey prototype building was modeled with the new PT steel connections. Nonlinear time history analyses yielded promising results wherein the lateral displacements and storey shears were considerably reduced when compared with the former welded connections.

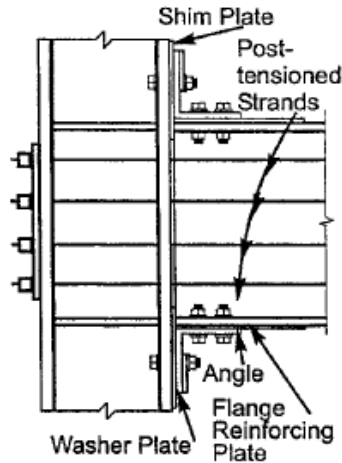


**Figure 2.12 Proposed PT steel moment connection [from Ricles et al. (2001)]**

After witnessing the failure of CBFs and BRBFs to restore normal functioning of the structure after the earthquake, a large research collaboration between Lehigh, Princeton and Purdue Universities gave way to an improved CBF with self-centering capability and called it a self-centering concentrically braced frame (SC-CBF) (Roke et al. 2006). The expected lateral force-deformation response of this system was presented using static equilibrium equations. This gave the intended limit states which later assisted in developing a performance-based design of such systems. As shown in Figure 2.13 the various limit states are: tension column decompression, yielding of PT members, yielding of frame members and finally failure of frame members. Various configurations of SC-CBFs have been identified with different locations and amount of PT and presence of energy dissipation devices. Analytical models based on a preliminary design using the performance limits already defined were investigated to verify if they comply with the set targets.

Further investigation by Sause et al. (2006) identified the flaw in the design procedure which led to undesirable response of the SC-CBF and thus failed to achieve the performance objectives. They demonstrated through dynamic analysis that the total overturning moment from all the modes

could be effectively represented by the first mode response alone. However, this was not the case with the base shear. The total base shear from all modes did not depend on the first mode response and hence required the contribution of higher modes as well. The study recommended the use of energy dissipaters all along the height of the frame to reduce the higher mode effects.

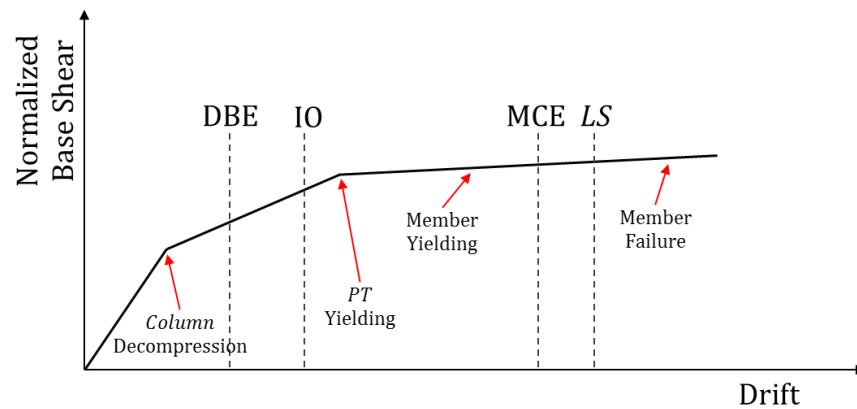


**Figure 2.13 Proposed limit states, performance levels and seismic hazard intensities [after Roke et al. (2006)]**

The latest study by Sause et al. (2014) validated the performance of SC-CBF through extensive hybrid simulations of a four storey 60% scaled prototype. The test structure showed desirable performance under DBE level earthquakes with the maximum peak drift of 1.4%. The structure was essentially damage-free with only minor wear of the replaceable brass shim plates. However, MCE level earthquakes had a maximum peak drift of 3.9% and led to the yielding of PT elements. After the PT bars yielded, some of its prestress was lost which could influence the response of the structure in case it is not re-tensioned. The study further continued the tests with yielded PT to quantify the structural response in the face of aftershocks immediately following the main earthquake. DBE level aftershock ground motion was applied to the structure with partial yielded PT which still showed desirable performance without any significant amplifications of drift. A consecutive aftershock ground motion was again applied to this structure with further additional

yielding of PT to observe the structural response in the case of complete loss of prestress in the PT. The structural response was still positive with no signs of significant damage or drift amplifications.

### 2.3.5.2 Base Plate Yielding System

Midorikawa et al. (2002) proposed a novel system called Base Plate Yielding (BPY) system, which comprised of a weak base plate at the bottom of the steel column that yielded on being subjected to a severe earthquake allowing the column to uplift and rock. The hysteretic behavior of the base plate also contributed to the energy dissipation capacity of the system. No supplemental PT system was required as the gravity load of the frame alone was responsible to retain self-centering of the frame. Figure 2.14 shows the schematic BPY system with a close view of the components of the weak base plate. An analytical model of a five-storey one bay frame was developed for three different criteria of the base; conventional fixed-base, simple rocking base and weak base plate. Dynamic analysis indicated the superior performance of BPY systems in terms of storey shear and roof displacements when compared to fixed-base and simple rocking structures.

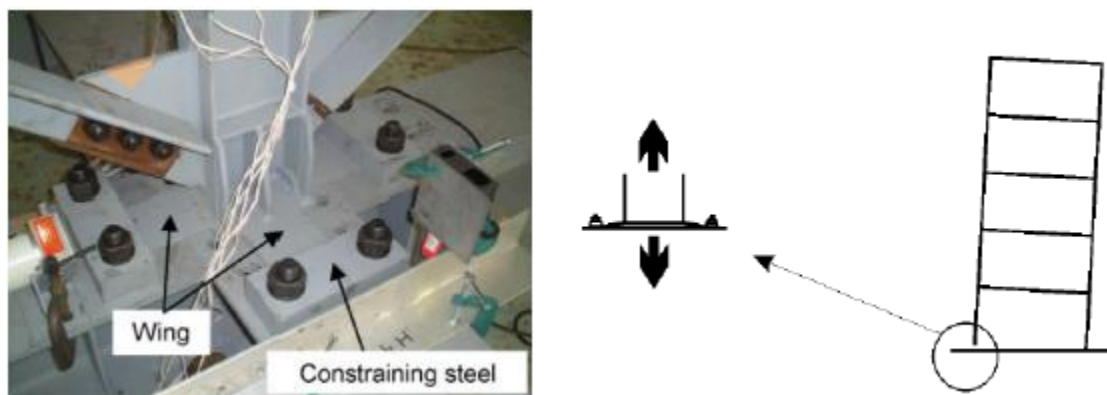


Figure 2.14 Base Plate Yielding (BPY) system [from Midorikawa et al. (2006)]

In a follow-up study, Midorikawa et al. (2003) carried out extensive shake table tests of the three models described previously and compared. The study indicated that the base shear and storey shear of BPY system was considerably lesser than the fixed-base counterpart. Even under extremely high input accelerations, the maximum roof displacement of the BPY system was lesser than that of the simple rocking frame while being almost comparable to the fixed-base system also. These results were verified again by a similar shake table study by Midorikawa et al. (2006), wherein a half scale prototype of a three-storey braced frame with yielding base plate was investigated. When compared with a fixed-base frame, the column base shear of the BPY system was seen to be reduced to almost 50%, but still having comparable roof displacements. This was attributed to the energy dissipation due to the yielding base plate. Also, the vertical impact forces in a BPY system was seen to be negligible and can conveniently be ignored while computing the column axial forces.

In a separate study, Azuhata et al. (2006) investigated and proposed that seismic performance of BPY systems can be improved by attaching conventional and adaptive viscous dampers at the column base besides yielding base plates. Adaptive viscous dampers allow for adjusting the damping coefficient based on the sign of vertical velocity at the uplifting part, so that they do not restrain the structure from uplifting but dissipate the seismic energy when the structure is landing. Numerical analyses of a building frame subjected to 1995 Kobe NS ground motion were carried out to demonstrate the efficiency of these added dampers. The analyses show that the adaptive dampers prove to be more efficient compared to the conventional dampers in controlling the displacement response of the structure without significantly increasing the overturning moment in the structure.

### 2.3.5.3 Viscously Damped Rocking Braced Frame

Tremblay et al. (2008a) examined an innovative braced frame shown in Figure 2.15, designed to rock at its base when subjected to severe ground shaking. The column bases are equipped with vertically oriented viscous dampers which control the maximum response by dissipating seismic energy, while reducing the impact forces induced by columns hitting the foundation. The study investigated the seismic response of the frame through analytical and experimental work. The system was able to limit the base overturning moment and lateral forces experienced while sustaining design ground motions without considerable damage. However, the results also indicated that as the building height increased, the axial force demand in the first storey braces amplified due to the influence of higher modes.

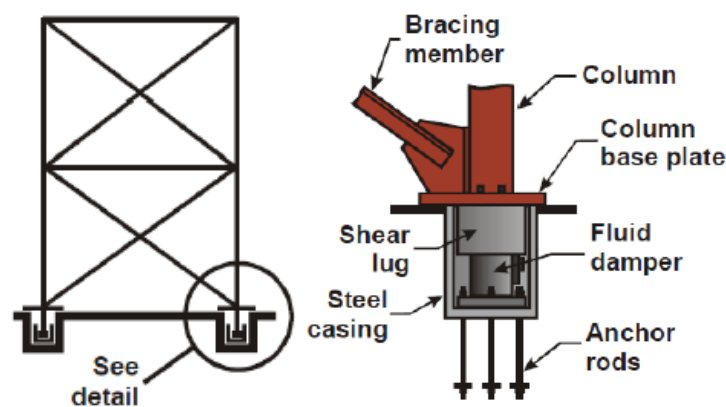


Figure 2.15 Viscously damped rocking braced frame [from Tremblay et al. (2008a)]

### 2.3.5.4 Controlled Rocking Frame with replaceable energy-dissipating fuses

As a joint research collaboration between University of Illinois at Urbana-Champaign, Stanford University and E-Defense Shaking Table Facility in Miki, Japan, Hajjar et al. (2008) proposed a novel controlled rocking frame as shown in Figure 2.16. The frame consisted of three major components; frame members that were intended to stay elastic throughout the seismic activity, PT

tendons contributing to self-centering of the system and replaceable energy dissipating elements that act as fuses against the sudden surge of input seismic energy. The project comprised of several phases which included conceptual design, component development and validation of these novel self-centering systems through comprehensive experimental and analytical studies. An ancillary study by Hall et al. (2010) investigated the sensitivity of some particular design variables on the response on the controlled rocking frame. The selected design variables are as follows.

$$(i) \quad \textit{Geometric Parameter} = \textit{Frame Width} / \textit{Fuse Width}$$

$$(ii) \quad \textit{Strength Parameter} = \textit{Overturning Resistance} / \textit{Design Overturning Moment}$$

$$(iii) \quad \textit{Self - Centering Parameter} = \textit{Post - tensioning Resistance} / \textit{Fuse Resistance}$$

One of the most important finding of this study was that the fuse was central and essential component that greatly influenced overall global behavior. The authors thus recommend to use fuses that have stable hysteresis over multiple cycles of seismic excitation and also possess fairly high shear deformation capacity.

This study was followed by a series of experimental testing of selected configurations of yielding shear plates with slits to act as fuses shown in Figure 2.17 (Ma et al. 2010a). This study tested a total of eleven steel shear plate fuse specimens, out of which five had slits dividing the plate into rectangular links and the remaining six had diamond-shaped slits creating butterfly-shaped links. Quasi-static cyclic testing revealed that the butterfly-link shear plate performed comparatively better, with the thin-plate and thick-plate fuses sustaining about 35% and 37% shear deformation until fracture. The shear plates with rectangular slits, on the other hand, showed stable hysteresis up to 5% shear deformation, after which severe pinching due to lateral-torsional buckling was observed.

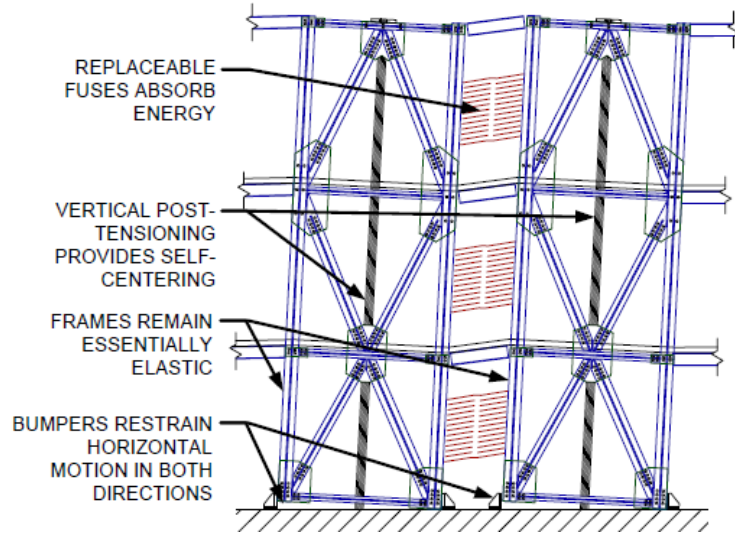


Figure 2.16 Controlled rocking with replaceable energy dissipating fuses [from Hajjar et al. (2008)]

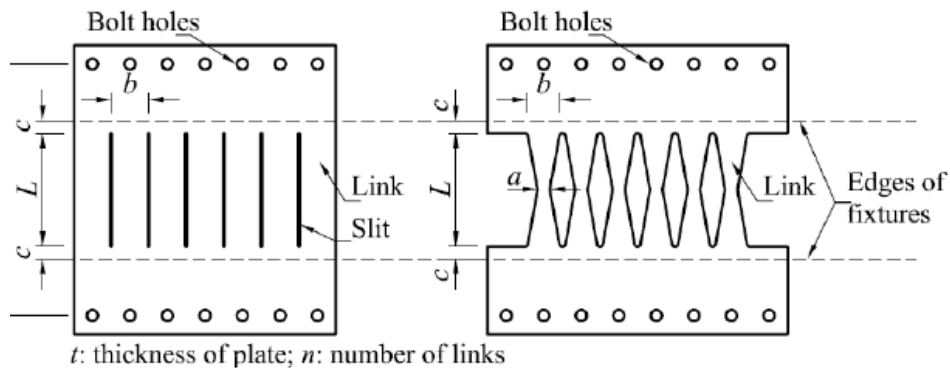


Figure 2.17 Fuse configurations [from Ma et al. (2010a)]

Eatherton et al. (2010) conducted quasi-static cyclic and hybrid simulation tests on half-scale single and dual controlled rocking frame configurations. The configuration where the initial pretension in the PT and fuse yield strength were considered equal, the frame performed exceptionally well with negligible residual displacement for a maximum roof drift of 3% which was more than the code-prescribed value considered for MCE level earthquakes. Hybrid simulations included investigating the system dynamic response and assisted in defining critical

limit states for the different components of the controlled rocking frame. In a companion paper, Ma et al. (2010b) presented the results of large (two-thirds) scale dynamic shaking table tests of the controlled rocking frame prototypes. The system performance was reliable when subjected to MCE level drift ratios of almost 3%. There was no damage observed in any of the components and the system successfully self-centered post the ground shaking. These tests confirmed the viability of these systems in achieving virtually damage-free state, even in the face of severe ground shaking. Numerical models were developed which were able to simulate the test results with great accuracy.

#### **2.4 Existing Applications of Controlled Rocking Systems**

One of the earliest structures to be built with the intension of incorporating rocking mechanism against lateral loads was the South Rangitikei Rail Bridge of New Zealand, which was completed in 1981. As shown in Figure 2.18, the piers in the transverse direction of this viaduct bridge were designed to deliberately rock by detaching them from the supports and introducing hysteretic dampers to provide additional damping.



**Figure 2.18 South Rangitikei Rail Bridge with a close up of the rocking piers [from Ma (2010a)]**

Another major application of rocking in bridges was the retrofit scheme for the North approach of the Lions' Bridge in Vancouver, Canada (Dowdell and Hamersley 2000). It was observed that the spectral accelerations of 1/475-year earthquakes were high enough to induce pull-out of the columns from the concrete foundation and cause rocking. Hence, the designers proposed a retrofit scheme where the force-limiting benefits of rocking mechanism were used to provide a robust and cost-effective design alternative.

Kilmore Street Medical Centre in Christchurch, New Zealand was built using coupled steel rocking frames as shown in Figure 2.19 (Latham et al. 2013). The frames used macalloy post tensioning bar systems and a combination of hysteretic and viscous dampers at the base and at upper locations to couple the frames.



Figure 2.19 Kilmore Street Medical Centre [from Latham et al. (2013)]

## 2.5 Existing Design Methodologies for Controlled Rocking Steel Frames

Most of the design methodologies for controlled rocking frames that exist comprise of three main tasks:

- (i) Compute the minimum rocking base shear and corresponding base overturning moment using any available method like the equivalent static force procedure.
- (ii) Proportion the fuse yield strength and initial PT force and design them accordingly.
- (iii) Capacity design of frame members for the maximum force exerted by the PT and fuse.

The first two tasks are generic with minor variations in the different design methodologies discussed here. As shown already, higher modes influence the rocking response to a considerable extent and hence need to be accounted for in the capacity design strategy to accurately estimate the force demands in the system. This section summarizes the various design procedures developed for controlled rocking steel frames, with a special focus on their respective capacity design strategies.

Roke et al. (2009) presented a probability-based design framework to conservatively estimate the force demands on the members of a SC-CBF. Nonlinear dynamic analysis revealed that the member capacities safely exceeded the design demands due to higher modes introduced by rocking response. Following steps summarize the member design procedure.

- (i) Modal decomposition of a linear elastic fixed-base SC-CBF model is conducted. From this, the first-mode lateral force distribution is obtained.
- (ii) This first-mode lateral force distribution is then scaled up to the level corresponding to PT yielding and applied to the model to determine the first mode member force demands.
- (iii) For higher mode contribution, the lateral force distribution for each of the desired mode is determined using corresponding values of pseudo-acceleration from design response spectrum. The member modal-force demand,  $r_{a,n}$  (where  $a$  is the member and  $n$  is the mode number), is quantified from a linear elastic analysis using the lateral force distribution for its corresponding mode.

- (iv) The modal force demand obtained in (iii) is then amplified using load factor,  $\gamma_n$  obtained from probabilistic analysis of the results of nonlinear analyses.  $\gamma_n$  is taken as 1.15 for the first mode and 2.0 for the remaining modes.
- (v) The final design force demand on the member,  $r_{a,design}$  is computed by combining the modal force demands using the Complete Quadratic Combination (CQC) method (der Kiureghian 1981) by suitably accounting for the correlation between the modal responses of the SC-CBF. This is given by the following equation:

$$r_{a,design} = \left[ \sum_{i=1}^N \sum_{j=1}^N \rho_{ij} (\gamma_i r_{a,i}) (\gamma_j r_{a,j}) \right]^{0.5} \quad [2.8]$$

Where  $N$  is the number of modes considered and the coefficient  $\rho_{ij}$  accounts for the correlation between modal responses and is given by:

$$\rho_{ij} = \begin{cases} 1, & i = j \\ 0.25, & i \neq j \end{cases} \quad [2.9]$$

Eatherton and Hajjar (2010) observed that designing the controlled rocking frames in accordance with the ASCE code guidelines with inverted triangular lateral load profile, was inefficient and yielded undesirable response. The higher modes were seen to be dominant in the frame which caused unpredictable amplification of column force demands as high as 5 times and brace axial force demands as high as 12 times. Hence, they formulated a capacity design approach wherein the frame members were designed for the worst case among multiple lateral load profiles as shown in Figure 2.20. These member force demands were then amplified by suitable amplification factors to account for the dynamic effects and higher modes. These amplification factors were obtained from extensive nonlinear time history analysis and were defined as the ratio of axial force demand to the design axial force. This capacity design procedure was proven to be

successful in estimating the force demands in the columns, but still underestimated the force demands in the braces by a factor of 2.7 at the MCE seismic level.

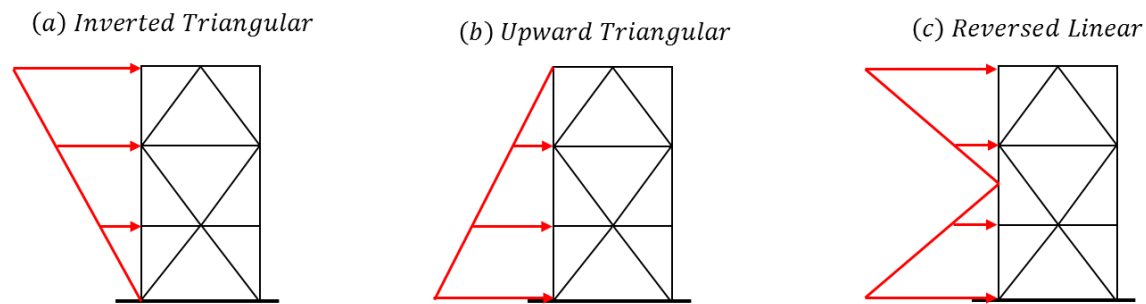


**Figure 2.20 Proposed lateral load profiles [after Eatherton and Hajjar (2010)]**

Ma (2010b) proposed a comparatively robust design methodology that was consistent with the current seismic code force-based design and also encompassed elements of DDBD (Priestley et al. 2007). The procedure starts off by estimating the design rocking base shear and base overturning moment assuming a force-reduction factor ( $R$ ) of 8, corresponding to that of an EBF. This system strength is then allocated to the PT and fuse components assuming a relevant self-centering parameter value. Once the individual component strengths are determined and designed accordingly, the system pushover relationship is established. A target displacement based on rigid rocking motion of the frame is assumed and secant stiffness based on the system pushover is estimated. A calibration factor  $\lambda = 1.8$  is used to amplify the system stiffness recognizing the inherent nature of rocking frames to be stiffer during earthquake. The resultant amplified or effective stiffness is then used to estimate the effective fundamental period of the structure. The peak spectral-displacement is read off the 5% damped displacement spectrum. This is compared with the initial target displacement assumed to see if it is within acceptable tolerance level. Otherwise, this exercise is iterated until the final displacement is reasonably close to the target.

Once the frame drift prediction is achieved, next step is to predict the manifestation of the lateral loads in the frame as observed in the shake table tests. The peak storey shear distribution is approximated through an empirical formulation represented as:

$$V_{max} = \frac{M_{b,max}}{H_{eff}} \quad [2.10]$$

$$V_{top} = \frac{1.1 \times V_{max}}{\sqrt{n}} \quad [2.11]$$

where  $M_{b,max}$  represented the maximum base overturning moment corresponding to the maximum forces that could develop in the PT and fuse,  $H_{eff}$  was taken to be equal to frame width and  $n$  represented the number of stories. Equations [2.10] and [2.11] show that the design shear envelope could be approximated as a linear function of the height of the frame as shown in Figure 2.21.

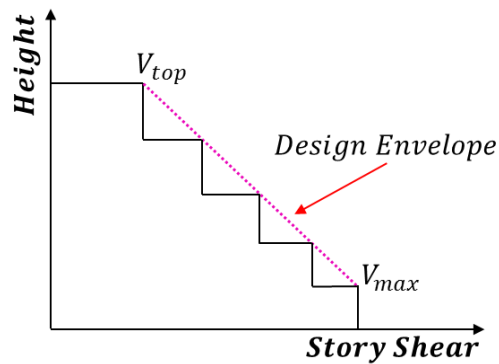


**Figure 2.21 Storey shear distribution envelope [after Ma (2010b)]**

In pursuit of a modern performance-based design for controlled rocking steel frames, Wiebe and Christopoulos (2013) developed a framework that could efficiently design steel frames by accurate prediction of frame member force demands due to higher modes. Besides this, novel mechanisms were introduced which could reduce the influence of higher modes and were directly incorporated into the design procedure. Through analytical models, the designed frames were

shown to conform to the displacement targets chosen as performance levels at two different seismic intensities. The first step of the design process is to proportion the base rocking joint by appropriately selecting amount and location of PT and fuse. This step includes calculation of minimum rocking base shear of an equivalent SDOF system using the force-reduction factor ( $R$ ) from the charts generated by the study through nonlinear dynamic analyses. The remaining hysteretic parameters of the intended flag-shaped hysteresis are also assumed. Similar to the other methodologies, the obtained system strength is equated to the contributions of the PT and fuse to assist their designs. The second step of the design process is critical and involves combining the modal contributions of storey shear and overturning moment envelopes ( $V_{max}$  and  $M_{max}$ ). Empirical equations representing these modal contributions, as a function of overstrength base overturning moment resistance ( $M_{b,max}$ ); height of each storey above the base ( $z$ ); total height of the frame  $H$ ; tributary seismic mass  $W_{trib}/g$  and the 5% damped spectral accelerations at one-third and one-fifth of the fundamental periods of the structure ( $S_a(T_1/3)$  and  $S_a(T_1/5)$ ), are given by:

<b>Storey Shear:</b>	$V_{1,max}(z) = \frac{3}{2} \left( \frac{M_{b,max}}{H} \right) \left[ 1 - \left( \frac{z}{H} \right)^2 \right]$	[2.12]
	$V_{2,max}(z) = 0.1265[\alpha_i S_a(T_1/3)] \left( \frac{W_{trib}}{g} \right) \left  \cos 4.49 \left( \frac{z}{H} \right) + 0.217 \right $	[2.13]
	$V_{3,max}(z) = 0.0297[\alpha_i S_a(T_1/5)] \left( \frac{W_{trib}}{g} \right) \left  \cos 7.73 \left( \frac{z}{H} \right) - 0.1283 \right $	[2.14]

<b>Overturning Moment:</b>	$M_{1,max}(z) = M_{b,max} \left[ 1 - \frac{3}{2} \left( \frac{z}{H} \right) + \frac{1}{2} \left( \frac{z}{H} \right)^2 \right]$	[2.15]
	$M_{2,max}(z) = 0.0282[\alpha_i S_a(T_1/3)] \left( \frac{W_{trib}}{g} \right) H \left  \sin 4.49 \left( \frac{z}{H} \right) + 0.976 \left( \frac{z}{H} \right) \right $	[2.16]
	$M_{3,max}(z) = 0.00384[\alpha_i S_a(T_1/5)] \left( \frac{W_{trib}}{g} \right) H \left  \sin 7.73 \left( \frac{z}{H} \right) - 0.991 \left( \frac{z}{H} \right) \right $	[2.17]

Provisions for two supplemental mechanisms to suppress the response of higher modes that were proposed included introducing multiple rocking joint and the use of Self-Centering Energy Dissipative (SCED) brace initially developed by Christopoulos et al. (2008). The beneficial effects of these mechanisms were validated through nonlinear dynamic analysis.

The most recent study by Pollino (2015) considered a rocking braced frame (RBF) with a combination of displacement-dependent steel yielding device and velocity dependent viscous damper that could virtually eliminate the need for PT and still show propensity for self-centering. The design procedure for RBFs requires establishing its nonlinear static force-deformation behavior with the contributions of all its components. Then the effective time period at design displacement and total equivalent damping of the RBF system in the primary rocking mode is computed. This information assists in estimating the peak RBF displacements using response spectrum analysis. Finally, the capacity design procedure for frame member demands requires the Square Root of Sum of Squares (SRSS) modal combination of the force demand from the primary

rocking mechanism and the force demands from higher modes. It has been noted that the higher mode brace forces can be as high as 2-3 times the force computed from the rocking mode only.

## **2.6 Summary**

This chapter discussed how allowing the structures to rock about the foundation leads to reduced internal forces in the structure, while providing stability against overturning in the event of strong earthquakes. This theory led to the development of controlled rocking systems with post-tensioned elements and supplemental damping devices. These systems are able to achieve reliable performance with self-centering, for greater seismic resilience. A few performance-based design methodologies were proposed for such systems. However, all the design methodologies discussed thus far either require complex modal analysis or the estimation of the structural time period or the force-reduction factor for calculating the design forces for the structure. Hence, there is a need of an alternative design procedure, which is simple yet robust and can efficiently design such novel SFRSs. To promote its implementation in the structural design office, the proposed design procedure should be computationally inexpensive, performance-based and non-iterative.

## **Chapter 3: Equivalent Energy Design Procedure (EEDP)**

This chapter discusses an alternative design procedure for CR-CBFs, called Equivalent Energy-based Design Procedure (EEDP). Section 3.1 briefly introduces the development of energy-based design methodologies. Then, Section 3.2 comprehensively explains EEDP and its design steps through the application in CR-CBFs.

### **3.1 Development of Energy-based Design Methodologies**

For the past 70 years that seismic provisions have been incorporated in the various building codes, a force-based design approach has been adopted which ensures suitable strength in the building to resist the action of the earthquakes. The obtained member sizes which satisfy strength requirement are then evaluated to check if they comply with the drift limits. If not, the exercise needs to be repeated until both strength and drift limits are satisfied. However, it was later realized that this may not be the best strategy to achieve optimum performance, which is not directly proportional to strength (Priestley 2000). The advent of ‘Performance Based Earthquake Engineering’ required design procedures to incorporate performance objectives rather than strength to ensure minimized damage and greater seismic resilience. It was widely recognized that ‘*structural displacements*’ serve as the direct damage indicators in the structure and hence can be critical to the analysis of performance. Therefore, conforming to the pre-determined displacement targets became central to all the design methodologies that were developed. Energy-based design procedures seek to address these flaws in the force-based design procedure, with robust formulations that may lead to efficient structural designs.

Energy-based design concepts have been around for five decades. It was first introduced by Housner (1956) at the First World Conference on Earthquake Engineering. He described the energy fed into the structure by the earthquake as  $E_i$ , a part of which is dissipated through damping,  $E_\xi$ , while the remaining is stored in the structure in the form of kinetic and strain energy,  $E_k$  and  $E_a$  respectively. The strain energy can be further split into elastic strain energy,  $E_s$ , and hysteretic energy,  $E_h$ , depending on whether the elastic limit is exceeded or not. This concept was further elaborated by Uang and Bertero (1988) who represented this as an energy balance equation as:

$$E_i = E_\xi + E_k + E_a = E_\xi + E_k + E_s + E_h \quad [3.1]$$

Goel and Chao (2008) pointed out that using the energy balanced Equation [3.1] can be cumbersome and often delays the design process in practice. Using Housner's concepts, they developed a practical design procedure called Performance Based Plastic Design (PBPD) which was efficient and accounted for the inelastic structural behavior directly. The method required a pre-selected target drift and an admissible yield mechanism to completely define the performance objectives to be achieved through controlled damage within the structure. Choosing the target drift prior to design process ensured that the design process was non-iterative. One of the key advantages of this method was that it didn't require employing coefficients like force-reduction factor ( $R$ ), or the deflection amplification factor ( $C_d$ ). Also, PBPD completely eliminated the need of complex nonlinear time-history analyses during the design phase. This method has been successfully applied to many of the code pre-qualified SFRSs like MRFs, CBFs, EBFs and special truss moment frames (STMF).

## 3.2 Equivalent Energy Design Procedure (EEDP) and its application in CR-CBF

Yang et al. (2016) improved the PBPD methodology to design novel high-performance fused SFRSs such as CR-CBFs to achieve different performance objectives at different shaking intensities. They named this design method Equivalent Energy-based Design Procedure (EEDP). Extensive nonlinear analyses on novel systems like spine fused frames, fused truss moment frames, have been developed and validated using this methodology. This section explains the basic derivation of EEDP and the steps involved in the design procedure that can be used to design CR-CBF.

### 3.2.1 Rocking Mechanism of CR-CBF

In order to properly design the CR-CBF using EEDP, a plastic (rocking) mechanism is needed. To simplify the design procedure, a separate gravity load resisting system is developed. Hence, the CR-CBF can be designed without considering the gravity loads. Figure 3.1(a) shows the deformed configuration of CR-CBF when the frame is not rocking and Figure 3.1(b) shows the deformed configuration of CR-CBF when the frame uplifts and rocks about the rocking toe. In these figures,  $\Delta$  indicates the system roof drift ratio (RDR) and  $F$  is the external force acting on the center of mass  $m$ . The global mechanism for CR-CBF is a series combination of two separate mechanisms; frame deformation (*Frame+PT*) and energy dissipation mechanism of (*ED*) through rocking at the base of frame.

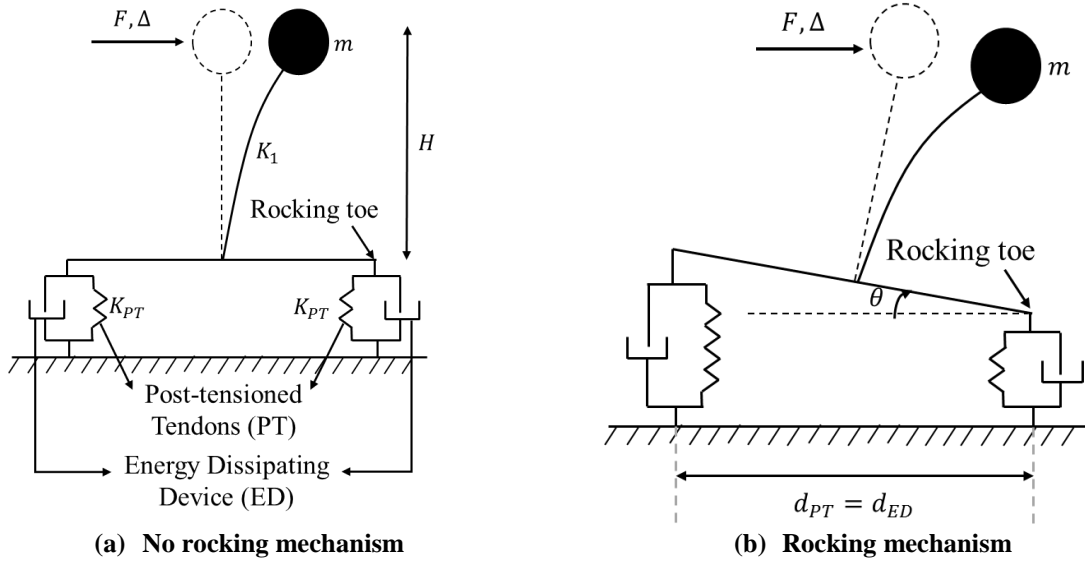


**Figure 3.1 Two degrees-of-freedom representation of a CR-CBF**

**FRAME+PT-** Figure 3.2(a) shows the force-deformation response of the frame members. It indicates that the frame is designed to remain elastic with a lateral stiffness  $K_1$ . Figure 3.2(b) shows the component force-deformation response of the PT. The PT tendons have an axial stiffness,  $K_{PT}$ , and are initially pre-tensioned to a force  $F_{PT,0}$ .  $d_{PT}$  represents the lever arm of PT from the rocking toe. The frame and PT act in series to provide a nonlinear restoring force component through gap opening mechanism at the base. In order to initiate rocking, the overturning moment needs to exceed the resisting moment provided by  $F_{PT,0}$ . The external force corresponding to the overturning moment is called minimum rocking base shear,  $F_1$ , which is calculated by Equation [3.2]. Prior to uplifting, the frame behavior dictates the system response of (Frame+PT) because the PT is not engaged. The RDR which corresponds to  $F_1$  is  $\Delta_1$  and can be calculated by Equation [3.3]. As  $F$  continues to increase after uplift, the PT starts to elongate which increases the frame flexibility since  $K_{PT}$  is practically assumed to be less than  $K_1$ . The system is nonlinear but still elastic at this stage. The post-uplift stiffness of the system,  $K_2$ , is the series combination of the

stiffness of frame and PT and can be calculated by Equation [3.4]. It should be noted that  $K_{PT}$  is the local stiffness of the PT and needs to be transformed to the global coordinates. Eventually,  $F_2$ , calculated by Equation [3.5] is reached at yielding of PT (denoted by  $F_{PT,y}$ ). Ignoring strain hardening and other second-order effects in the PT after yielding, the (Frame+PT) system loses its load bearing capacity after reaching  $F_2$  and becomes perfectly plastic. The RDR corresponding to  $F_2$  is  $\Delta_2$  and is calculated by Equation [3.6]. Figure 3.2(c) shows the final (Frame+PT) system force-deformation response with the design parameters defined thus far.

$$F_1 = \frac{F_{PT,0} \times d_{PT}}{H} \quad [3.2]$$

$$\Delta_1 = \frac{F_1}{K_1 \cdot H} \quad [3.3]$$

$$K_2 = \left[ \frac{1}{K_1} + \frac{1}{K_{PT} \left( \frac{d_{PT}}{H} \right)^2} \right]^{-1} \quad [3.4]$$

$$F_2 = \frac{F_{PT,y} \times d_{PT}}{H} \quad [3.5]$$

$$\Delta_2 = \frac{F_2 - F_1}{K_2 \cdot H} + \Delta_1 \quad [3.6]$$

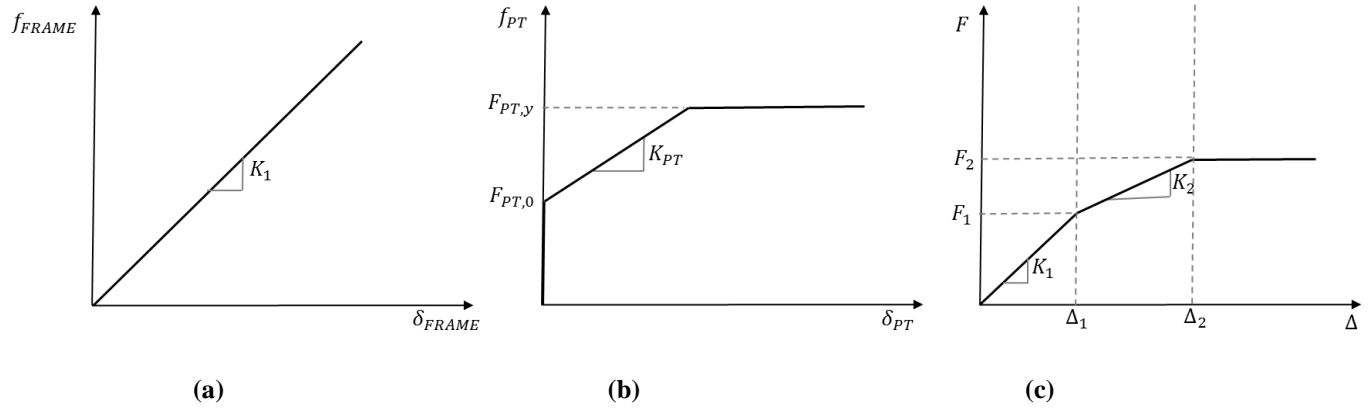


Figure 3.2 (a) Local force-deformation response of *Frame*; (b) Local force-deformation response of *PT*; (c) Global force-deformation response of (*Frame+PT*)

**ED-** Figure 3.3 shows the ED local force-deformation response. It is assumed that ED has a rigid and perfectly plastic response. The design slip load for ED is  $F_{ED}$ . ED doesn't have stiffness contribution to the system and is intended to dissipate the earthquake energy as soon as column uplift occurs.  $d_{ED}$  represents the lever arm of ED from the rocking toe.

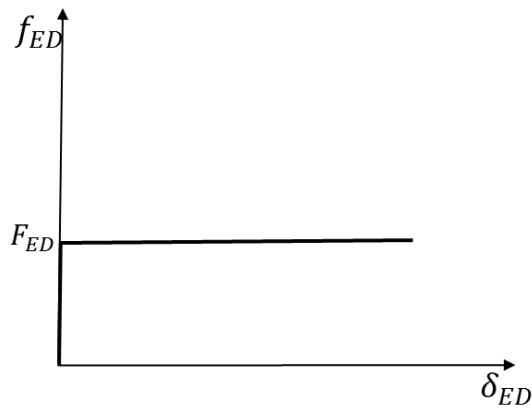


Figure 3.3 Local force-deformation response of ED

**FRAME+PT+ED-** Finally, all the components of a CR-CBF act together to give a final trilinear force-deformation relationship as shown in Figure 3.4. This is modified from the trilinear response

of the (Frame+PT) system to incorporate *ED*. The modified minimum rocking base shear,  $F_y$ , is calculated by Equation [3.7]. The ultimate strength,  $F_p$ , is calculated by Equation [3.9]. These parameters include the effects of ED. Similarly, the RDRs are modified with the addition of *ED*, i.e.,  $\Delta_1$  increases to  $\Delta_y$  and  $\Delta_2$  increases to  $\Delta_p$ , which are calculated by Equation [3.8] and Equation [3.10] respectively. Finally,  $\Delta_u$  is the ultimate RDR.

$$F_y = \frac{F_{PT,0} \times d_{PT} + F_{ED} \times d_{ED}}{H} \quad [3.7]$$

$$\Delta_y = \frac{F_y - F_1}{K_1 \cdot H} + \Delta_1 \quad [3.8]$$

$$F_p = \frac{F_{PT,y} \times d_{PT} + F_{ED} \times d_{ED}}{H} \quad [3.9]$$

$$\Delta_p = \frac{F_u - F_2}{K_2 \cdot H} + \Delta_2 \quad [3.10]$$

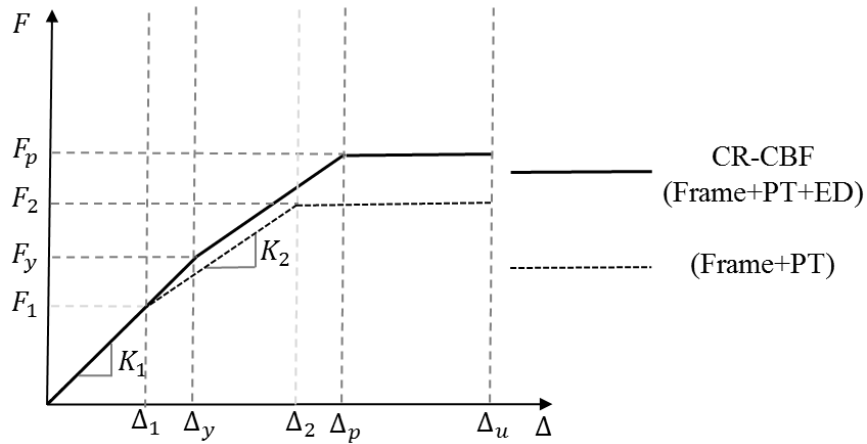


**Figure 3.4 System force-deformation response of CR-CBF**

### 3.2.2 Overview of EEDP for CR-CBF

EEDP is a non-iterative, performance-based design procedure which is targeted to achieve multiple performance objectives at different seismic hazard intensities. Unlike the existing design methodologies for controlled rocking frames, EEDP doesn't require intricate modal analysis nor estimation of fundamental period of structure or force-modification factors for the calculation of design base shears. Figure 3.5 shows the concept of EEDP. The solid line represents the equivalent nonlinear single degree-of-freedom (ENLSDOF) system of CR-CBF. The dashed line represents the equivalent linear single degree-of-freedom (ELSDOF) system. EEDP relates the energy stored in the ELSDOF system (elastic energy,  $E_a$ ) to the energy dissipated by the ENLSDOF system (elastic strain energy,  $E_s$ , and hysteretic energy,  $E_h$ ). In the figure, the ordinate represents base shear,  $F$ , which is calculated by multiplying pseudo acceleration,  $S_a$ , by the structural mass,  $m$ . The abscissa represents RDR,  $\Delta$ , which is obtained by normalizing the roof displacement by the structural height,  $H$ . Equation [3.11] shows the relationship between RDR and spectral displacement of an ELSDOF system.  $F_e$  signifies the corresponding base shear.

$$\Delta_e = (C_0 S_d) / H \quad [3.11]$$

where  $C_0$  is the coefficient that is used to modify  $S_d$  of an ELSDOF system to the roof displacement of a multiple DOF system (ASCE/SEI 41-06 2007).

EEDP determines the response of the ENLSDOF system using five keys design parameters.  $F_y$  and  $F_p$  are the yielding and ultimate base shears of the ENLSDOF system, respectively.  $\Delta_y$  and  $\Delta_p$  are the RDRs of the ENLSDOF system which correspond to the base shears  $F_y$  and  $F_p$ , respectively.  $\Delta_u$  is the ultimate RDR. The trilinear force-deformation response of a CR-CBF allows it to have a specific desired progression of limit states chosen for this thesis, as shown in

Figure 3.6. Each of these limit states is associated to a discrete performance objective at a designated seismic hazard intensity.

- (i) At the low seismic shaking intensity, also known as the Service Level Earthquake (SLE), the CR-CBF is expected to remain elastic and damage-free, which achieves the Immediate Occupancy (IO) performance objective.
- (ii) At the medium seismic shaking intensity, also known as Design Basis Earthquake (DBE), the primary SFRS (ED) are expected to yield as soon as the frame uplifts and protect the remaining structure. With only the ED devices yielded, the system is considered to achieve Life Safety (LS). The ED are structural fuses in CR-CBF, which are designed to dissipate the sudden surge of earthquake energy. The strategic location of ED assists in their efficient inspection and repair after the earthquake, without affecting the functionality of the building.
- (iii) At the high seismic shaking intensity, also known as Maximum Credible Earthquake (MCE), the secondary SFRS (Frame+PT) is designed with PT to yield to prevent the structure from collapse. Hence, Collapse Prevention (CP) performance objective is achieved. After the earthquake, the yielded PT can be suitably repaired either by re-tensioning or replacing. It should be noted, that at the CP performance level, only the ED devices and the PT are yielded, while the remaining frame members shall remain elastic. This ensures low structural damage levels leading to quicker post-earthquake rehabilitation process.

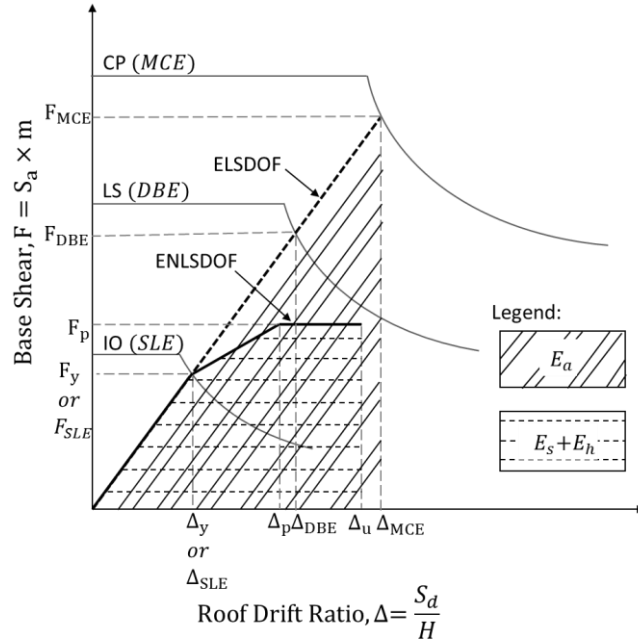


Figure 3.5 Concept of Equivalent Energy Design Procedure (EEDP)

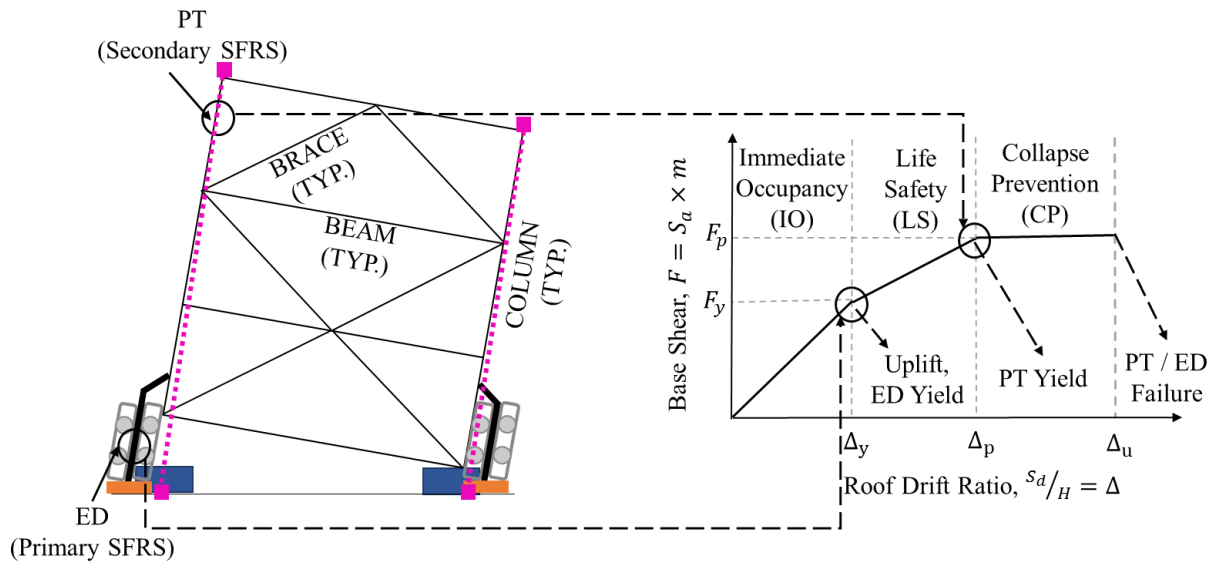


Figure 3.6 Limit states and performance levels of a CR-CBF

The following steps are involved in implementing EEDP methodology in a design office.

- (i) Select performance objectives under different seismic hazard intensities.

- (ii) Select yielding RDR  $\Delta_y$  to compute  $F_y$  and  $T$ .
- (iii) Select plastic RDR  $\Delta_p$  to compute  $\gamma_a$  and  $F_p$ .
- (iv) Calculate  $\gamma_b$  and ultimate RDR  $\Delta_u$ .
- (v) Distribute design base shears between primary and secondary SFRSs.
- (vi) Select yielding mechanisms and design structural members.

### **3.2.2.1 Select Performance Objectives under different Seismic Hazard Intensities**

The first step of EEDP is to select different performance objectives for the structure under different seismic hazard intensities. The three different hazard intensities (SLE, DBE and MCE) can be based on regional seismic codes or from probabilistic seismic hazard analysis. For this study, the performance objectives for CR-CBFs corresponding to the chosen target seismic hazard intensities have already been explained in Figure 3.6.

### **3.2.2.2 Select Yielding RDR $\Delta_y$ to Compute $F_y$ and $T$**

Structural and non-structural components within the prototype can tolerate a specific amount of lateral roof drift ratio before experiencing damage (or uplift in this case). The designer needs to select this parameter, called the yielding roof drift ratio or  $\Delta_y$ . The goal of this step is to ensure that EEDP designed CR-CBF prototype behaves like an elastic fixed-base CBF when subjected to earthquakes with intensities lower or equals to SLE. In other words, it is expected that the system will experience a median roof drift ratio close to the selected  $\Delta_y$  when subjected to ground motions at SLE hazard level. Once the shaking intensity exceed the SLE shaking, the CBF is designed to uplift, while the ED starts to dissipate the earthquake energy. Once SLE hazard curve and  $\Delta_y$  have

been identified, the yielding base shear,  $F_y$ , can be identified from the intersection of SLE hazard curve and  $\Delta_y$ . It should be noted that, at this intersection, the fundamental period,  $T$ , can be calculated using the following equation.

$$T = 2\pi \sqrt{\frac{(\Delta_y H)/C_o}{F_y/m}} \quad [3.12]$$

### 3.2.2.3 Select Plastic RDR $\Delta_p$ to Compute $\gamma_a$ and $F_p$

The next step of EEDP is to select the second yielding point on the trilinear force-deformation relationship, called the plastic roof drift ratio or  $\Delta_p$ . When the prototype is excited by ground motions of intensities equal to DBE, only the primary SFRS (ED) should yield. While the median roof drift ratio should be close to the selected  $\Delta_p$ . Once DBE hazard level is exceeded, the secondary SFRS (Frame+PT) are designed to be engaged, where the PT are designed to yield. EEDP relates the energy stored by the ELSDOF system between the SLE and DBE hazard intensities,  $\Delta E_{E1}$ , to the energy dissipated by the ENLSDOF system,  $\Delta E_{NM1}$ , as shown in Equation [3.13]. To account for the difference in these energies, an energy modification factor,  $\gamma_a$ , is used.

$$\Delta E_{E1} = \Delta E_{NM1} \times \gamma_a \quad [3.13]$$

where  $\Delta E_{E1} = \frac{H}{2}(F_{SLE} + F_{DBE})(\Delta_{DBE} - \Delta_{SLE})$ ;  $\Delta E_{NM1} = \frac{H}{2}(F_y + F_p)(\Delta_p - \Delta_y)$ ;  $F_{SLE}$  is the elastic base shear of the ELSDOF system at SLE shaking intensity;  $F_{DBE}$  is the elastic base shear of the ELSDOF system at DBE shaking intensity;  $\Delta_{SLE}$  is the roof drift ratio of the ELSDOF system at SLE shaking intensity;  $\Delta_{DBE}$  is the roof drift ratio of the ELSDOF system at DBE shaking intensity.

$\gamma_a$  is the energy modification factor of the ENLSDOF system from  $\Delta_y$  to  $\Delta_p$ . As a result of comprehensive nonlinear dynamic time-history analyses, several charts have been generated which provide the value of  $\gamma_a$  for different structural periods  $T$  and choice of  $\mu_p$  (obtained by normalizing the choice of  $\Delta_p$  by the already chosen  $\Delta_y$  in *Step 2*). These plots have been reproduced in Figure 3.7.

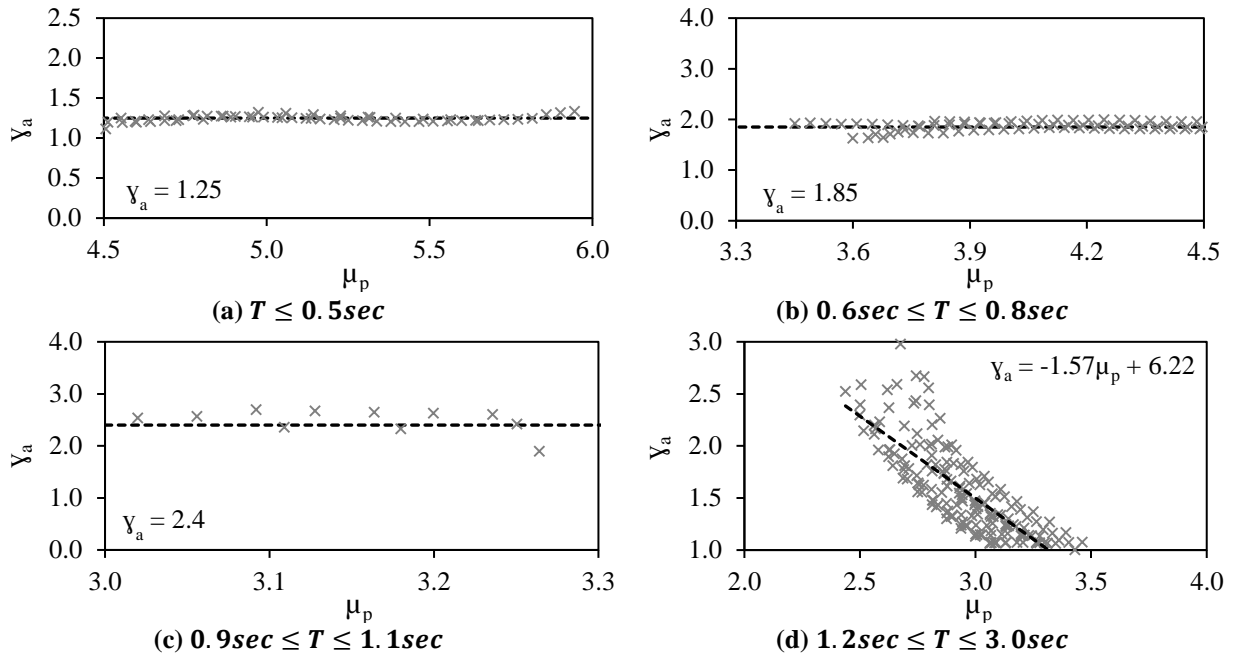


Figure 3.7 Energy modification factor  $\gamma_a$  [plots from Yang et al. (2016)]

In this step, equating work-energy equation gives the ENLSDOF system ultimate base shear,  $F_p$ , as represented by Equation [3.14].

$$F_p = \frac{2 \times \Delta E_{E1}}{\gamma_a H (\Delta_p - \Delta_y)} - F_y \quad [3.14]$$

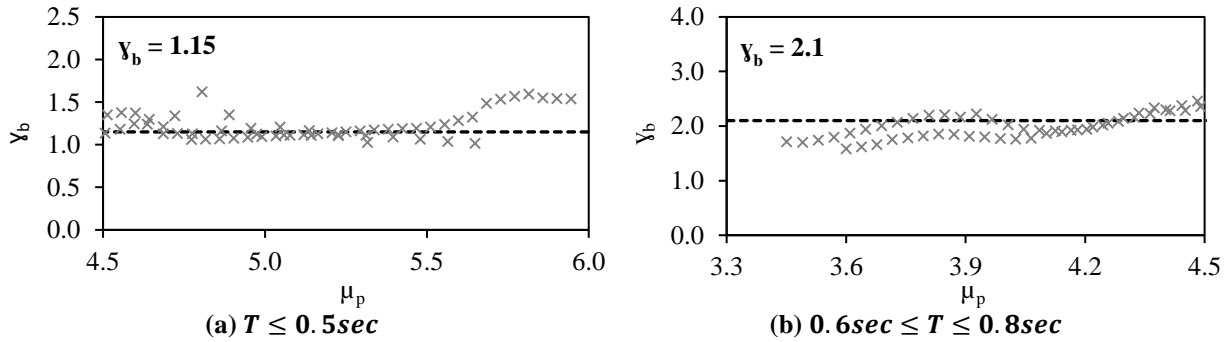
### 3.2.2.4 Calculate $\gamma_b$ and Ultimate RDR $\Delta_u$

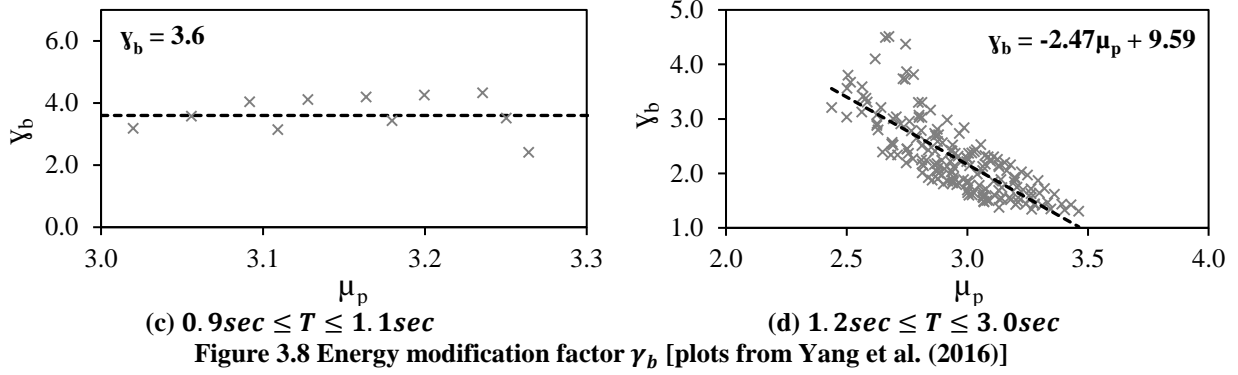
To fully define the trilinear backbone, ultimate drift ratio  $\Delta_u$  is computed corresponding to MCE hazard level. In EEDP, the CR-CBF system is assumed to be perfectly plastic after  $\Delta_p$  and should not experience any strength degradation prior to reaching  $\Delta_u$ . The system should exhibit median RDR close to the computed  $\Delta_u$  when subjected to ground motions at MCE hazard level. Similar to the previous step, the energy dissipated by the ENLSDOF system,  $\Delta E_{NM2}$  is a fraction  $\gamma_b$  of the energy stored by the ELSDOF system,  $\Delta E_{E2}$ , between DBE and MCE as represented by Equation [3.15].

$$\Delta E_{E2} = \Delta E_{NM2} \times \gamma_b \quad [3.15]$$

where  $\Delta E_{E2} = \frac{H}{2} (F_{DBE} + F_{MCE})(\Delta_{MCE} - \Delta_{DBE})$ ;  $\Delta E_{NM2} = F_p H (\Delta_u - \Delta_p)$ ;  $F_{MCE}$  is the elastic base shear of the ELSDOF system at MCE shaking intensity;  $\Delta_{MCE}$  is the RDR of the ELSDOF system at MCE shaking intensity.

$\gamma_b$  is the energy modification factor of the ENLSDOF system from  $\Delta_p$  to  $\Delta_u$ . Similar to  $\gamma_a$ , charts have also been generated for  $\gamma_b$  and have been reproduced in Figure 3.8.





In this step of EEDP, designers can look up  $\gamma_b$  and use Equation [3.16] to calculate  $\Delta_u$ .

$$\Delta_u = \frac{\Delta E_{E2}}{\gamma_b H F_p} + \Delta_p \quad [3.16]$$

### 3.2.2.5 Distribute Base Shears between Primary and Secondary SFRSs

Once the complete force-deformation response of the ENLSDOF system is established by EEDP, it needs to be distributed among the primary and secondary SFRSs. As already discussed previously, the response of CR-CBF depends on the combined responses of ED and (Frame+PT). Hence, the system strength defined by EEDP thus far needs to be distributed into both these subsystems to estimate their design yielding strengths. To ensure optimum performance of the structure while retaining the self-centering capability of the frame under the SLE, the restoring moment due to PT should be greater than or equal to the moment due to ED (Chancellor et al. 2014; Eatherton et al. 2010; Wiebe and Christopoulos 2013). This is represented by Equation [3.17]. Then, substituting the maximum value of  $(F_{ED} \times d_{ED})$  from Equation [3.7] in [3.17], the design slip load of ED can be computed by Equation [3.18].

$$F_{PT,0} \times d_{PT} \geq F_{ED} \times d_{ED} \quad [3.17]$$

$$F_{ED} = \frac{F_y \times H}{2 \times d_{ED}} \quad [3.18]$$

With the value of  $F_{ED}$  known, the value of initial pre-tensioning force  $F_{PT,0}$  can be calculated from Equation [3.7], as shown by Equation [3.19]. Finally, the design yield load of the PT can be computed by using the value of  $F_{ED}$  from Equation [3.18] and substituting it in Equation [3.9]. This is represented by Equation [3.20].

$$F_{PT,0} = \frac{(F_y \times H) - (F_{ED} \times d_{ED})}{d_{PT}} \quad [3.19]$$

$$F_{PT,y} = \frac{(F_p \times H) - (F_{ED} \times d_{ED})}{d_{PT}} \quad [3.20]$$

### 3.2.2.6 Select Yielding Mechanisms and Design Structural Members

The last step of the EEDP process is to select a plastic mechanism and to design the yielding members (ED and PT) using admissible yielding mechanisms and capacity design of the remaining non-yielding members. Since the mechanisms are defined for multiple DOF system, the design base shears need to be distributed across the height of the structure. As pointed out by several researchers, one of the primary concerns in designing systems like CR-CBFs is their propensity to excite higher modes which jeopardises the force-limiting mechanism offered by controlled rocking. Hence, the capacity design of frame members using code-based vertical distribution of base shear has proven to be inefficient in capturing the influence of higher modes. To tackle this deficiency, the vertical distribution of design base shears in the structure is assumed to be based on Equation [3.22], by Chao et al. (2007). They performed a series of nonlinear dynamic analyses on different steel moment frames using 21 ground motions from the SAC (SEAOC, ATC, CUREe) Los Angeles region (FEMA-355C 2000). They proposed a new distribution of base shear across

the height of the multi-degree of freedom (MDOF) system. This distribution was quite different from the conventional code-based distribution which was derived based on elastic mode shapes. The proposed shear distribution account for the inelastic force demand across the height of the structure and the influence of higher modes more accurately:

$$\beta_i = \frac{V_i}{V_n} = \left( \frac{\sum_{j=1}^n w_j h_j}{w_n h_n} \right)^{0.75T-0.2} \quad [3.21]$$

where  $\beta_i$  represents the normalized storey shear distribution with respect to top storey shear,  $V_n$ ;  $w_j$  and  $h_j$  are the weight and height of  $j^{\text{th}}$  storey respectively;  $w_n$  and  $h_n$  are the weight and height of top storey respectively. Using this, the lateral force distribution across the height of the structure can be obtained as:

$$F_i = \lambda_i V_y \quad [3.22]$$

where

$$\lambda_i = (\beta_i - \beta_{i+1}) \left( \frac{w_n h_n}{\sum_{j=1}^n w_j h_j} \right)^{0.75T-0.2} \quad [3.23]$$

Once all the yielding members have been designed, the remaining structure is capacity designed under the influence of the expected strength of the yielding components, after suitably accounting for any material strain hardening.

### 3.2.2.6.1 Seismic Demand on ED

Using the yielding mechanism shown in Figure 3.6 and the vertical base shear distribution from Equation [3.22], energy equilibrium is established by equating the external work done by the base shear on the deformed mechanism to the internal work done by the ED. The solution of the

equation yields the seismic demand on the ED, as shown by Equation [3.24]. This is simply calculated from Equation [3.18] by substituting  $F_y$  with its vertical distribution.

$$F_{ED} = \frac{\sum_{i=1}^n (\lambda_i \times F_y \times h_i)}{2 \cdot d_{ED}} \quad [3.24]$$

where  $h_i$  is the height of the  $i^{th}$  storey above the base.

### 3.2.2.6.2 Seismic Demand on PT

The seismic demand on the PT is calculated similar to that of the ED. The initial pre-tensioning force,  $F_{PT0}$ , is computed by substituting the base shear in Equations [3.19] with its vertical distribution and the value of  $F_{ED}$  from Equation [3.24]. Finally, the maximum demand on the PT,  $F_{PT,y}$ , is computed by substituting the base shear in Equation [3.20] with its vertical distribution and the value of  $F_{ED}$  from Equation [3.24].  $F_{PT0}$  and  $F_{PT,y}$  are given by Equations [3.25] and [3.26], respectively.

$$F_{PT0} = \frac{\sum_{i=1}^n (\lambda_i \times F_y \times h_i) - (F_{ED} \times d_{ED})}{d_{PT}} \quad [3.25]$$

$$F_{PT,y} = \frac{\sum_{i=1}^n (\lambda_i \times F_p \times h_i) - (F_{ED} \times d_{ED})}{d_{PT}} \quad [3.26]$$

With the demands on both the ED and PT known, the required configurations of the friction dampers and PT tendons can be estimated. Thus, the design of both the primary and secondary SFERS is accomplished at this step.

### 3.2.2.6.3 Capacity Design of Frame Members

The CR-CBF shall be designed such that the frame members shall never yield. This is achieved by capacity design of the frame elements under the maximum expected forces exerted by the yielding elements. Any of the capacity design approaches that have been explained in the previous

chapter can be used here. Figure 3.9 shows a preliminary 3-storey CR-CBF configuration and the free body diagrams (FBDs) of the joints. Based on the FBD in Figure 3.9(b), the force  $F_{PT,max}$  is transferred as a shear and moment in the 3<sup>rd</sup> storey beam:

$$V_{f,beam3} = F_{PT,max} \quad [3.27]$$

$$M_{f,beam3} = \frac{(2 \times F_{PT,max})L}{4} \quad [3.28]$$

Figure 3.9(c) shows the FBD of joint B and is used to calculate the axial compressive force in the 3<sup>rd</sup> storey braces. This is summarized as shown in Equation [3.29].

$$C_{f,brace3} = \frac{R_B}{2 \times \sin\theta} = \frac{F_{PT,max}}{\sin\theta} \quad [3.29]$$

Figure 3.9(d) shows the FBD of joint D. It can be seen that the 2<sup>nd</sup> storey braces shall be designed to carry the same load as the 3<sup>rd</sup> storey braces. The 2<sup>nd</sup> storey beam acts as a tension tie and the design axial tensile force can be computed as:

$$C_{f,brace2} = C_{f,brace3} \quad [3.30]$$

$$T_{f,beam2} = (C_{f,brace3} + C_{f,brace2})\cos\theta \quad [3.31]$$

Figure 3.9(e) shows the FBD of joint G. As clearly indicated by the load path, the 1<sup>st</sup> storey beam isn't expected to take any load. The 1<sup>st</sup> braces shall be designed to carry the same load as the 2<sup>nd</sup> storey braces.

$$C_{f,brace1} = C_{f,brace2} \quad [3.32]$$

Finally, the base level beam shall resist the horizontal component of the 1<sup>st</sup> storey brace axial compression force, as shown in Figure 3.9(f).

$$T_{f,beam0} = (C_{f,brace3})\cos\theta \quad [3.30]$$

Once the design forces for beams and braces are computed, the last step is to estimate the columns design forces. The self-weight of the structure is very small compared to the large design forces and hence can be safely neglected while designing the columns. The columns are continuous over all the levels and shall resist the force PT in axial compression:

$$C_{f,columns} = F_{PT,max} \quad [3.31]$$

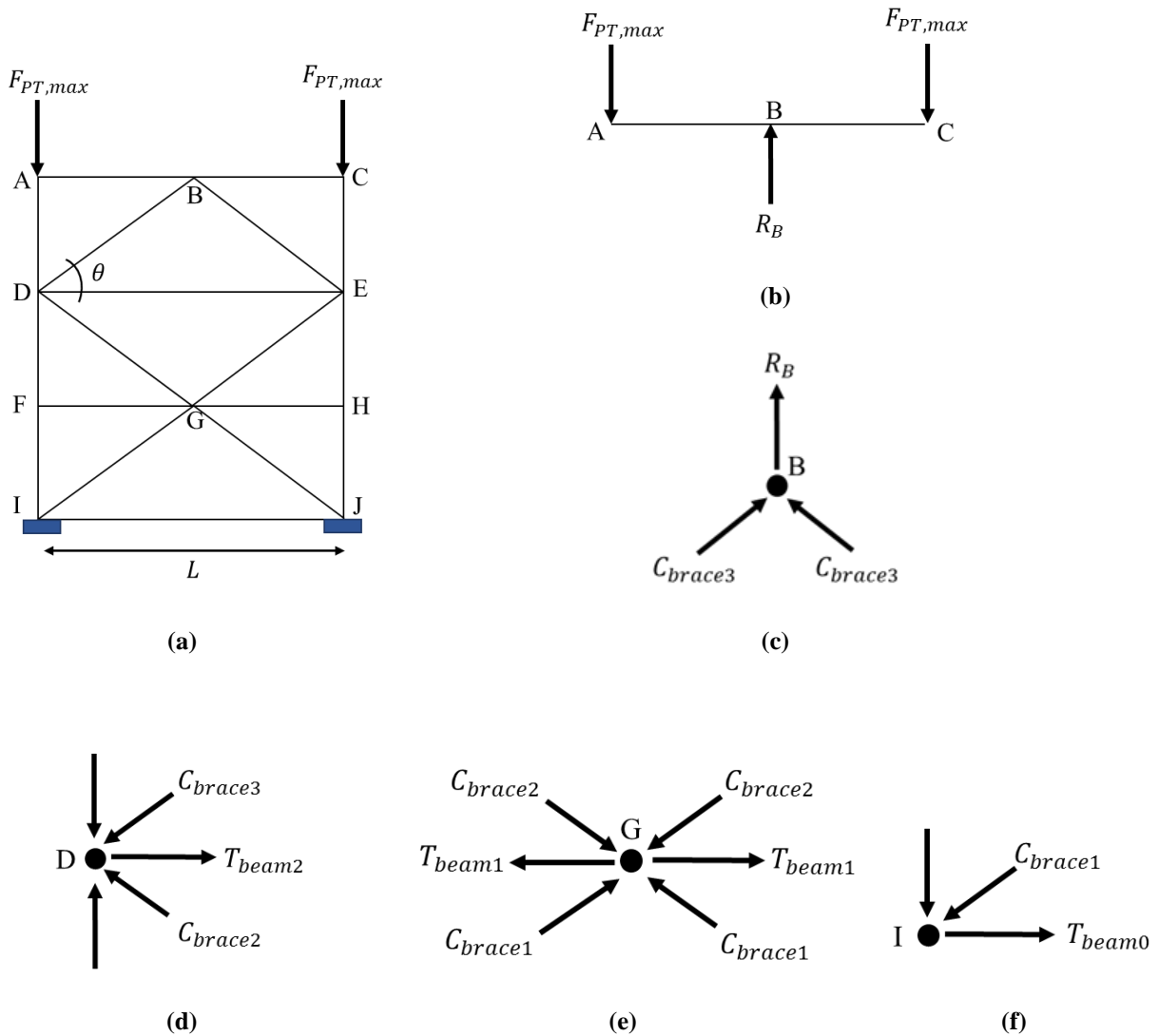


Figure 3.9 (a) Preliminary 3-storey CR-CBF configuration, (b) FBD of upper portion of frame, (c) FBD of joint B, (d) FBD of joint D, (e) FBD of joint G and (f) FBD of joint I

Finally, once all the frame member design force demands are determined, appropriate wide-flange sections are chosen to satisfy the requirements of ANSI/AISC 360-10 (2010). For flexural members, compact sections are selected which meet the criteria shown in Equation [3.32]. For these sections, only the limit states of yielding and lateral-torsional buckling are considered for calculating the nominal flexural strength. For compression members, the limit states of flexural buckling, torsional and flexural-torsional buckling are considered for calculating the nominal compressive strength, based on their slenderness ratio.

$$\frac{b_f}{2t_f} \leq 0.38 \sqrt{\frac{E}{F_y}} \text{ and } \frac{h_c}{t_w} \leq 3.76 \sqrt{\frac{E}{F_y}} \quad [3.32]$$

Where  $b_f$ : flange width;  $t_f$ : flange thickness;  $E$ : modulus of elasticity;  $F_y$ : minimum yield stress of steel;  $h_c$ : height of web and  $t_w$ : web width.

## **Chapter 4: Prototype Design and Numerical Modelling**

The focus of this chapter is to apply the EEDP methodology as presented in Chapter 3 to two prototype buildings with CR-CBFs of varying heights to validate the methodology can be efficiently used to design the CR-CBFs. Section 4.1 briefly summarizes the prototype building geometry and loading summary. Section 4.2 summarizes the procedure for selection of seismicity and hazard intensities for the chosen building prototypes. Section 4.3 presents the design calculations for both the prototypes. Finally, Section 4.4 presents the development and calibration of numerical models.

### **4.1 Description of the Prototype Buildings**

The prototype buildings being discussed here are adopted from the ATC-76 project (NIST 2010). This model was evaluated using the FEMA P695 (2009) methodology to quantify the building seismic performance factors. A 3-storey and 6-storey variant of the prototype building are considered. Figure 4.1 shows the floor plan and the elevation of the considered prototypes. Only the CR-CBF, which is the SFRS, is presented here. Table 4.1 summarizes the gravity loads used for the seismic design of the structure. The seismic weight of the roof is 1447 kips and that of all other floor is 2270 kips per floor.

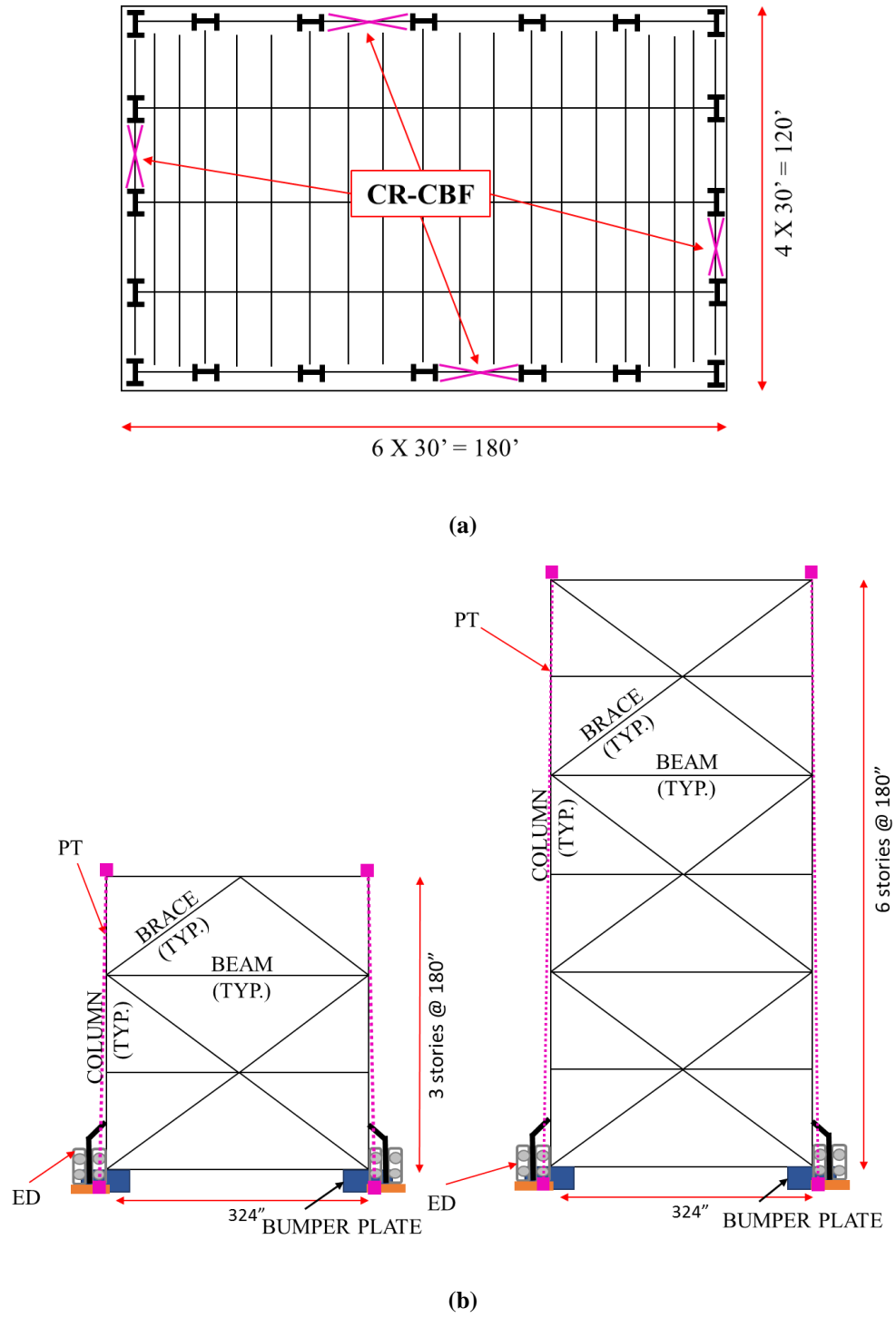


Figure 4.1 (a) Floor plan and (b) Elevation of the 3-storey and 6-storey CR-CBF prototypes

**Table 4.1 Gravity loads for CR-CBF prototypes**

<b>Category</b>	<b>Gravity Load (psf)</b>
<b>Roof Loading</b>	
Roofing and Insulation	7
Metal deck and Concrete filling	47
Steel framing and Fireproofing	8
Ceiling	3
Mechanical/Electrical	2
<b>TOTAL</b>	<b>67</b>
<b>Floor Loading</b>	
Metal deck and Concrete filling	47
Steel framing and Fireproofing	13
Partition walls	20
Ceiling	3
Mechanical/Electrical	2
<b>TOTAL</b>	<b>85</b>

This thesis assumes that the CR-CBF is decoupled from the gravity framing surrounding the SFRS. All the gravity load shall be transferred by a separate gravity system. Details of the gravity frame design is not presented in this research. Previous research such as the one presented by Eatherton and Hajjar (2010) can be used. In this configuration, shear plates were installed to connect the beam to the rocking frame and bending along their weak axis, this allows the transfer

of shear forces while allowing uninterrupted uplifting motion of the controlled rocking frame. In another configuration, the shear plates were replaced by yoke with sliders, which also served the same purpose. Preventing the SFRS from carrying any gravity load also ensured that the impacts did not excite any vertical modes leading to unwarranted damage of its components.

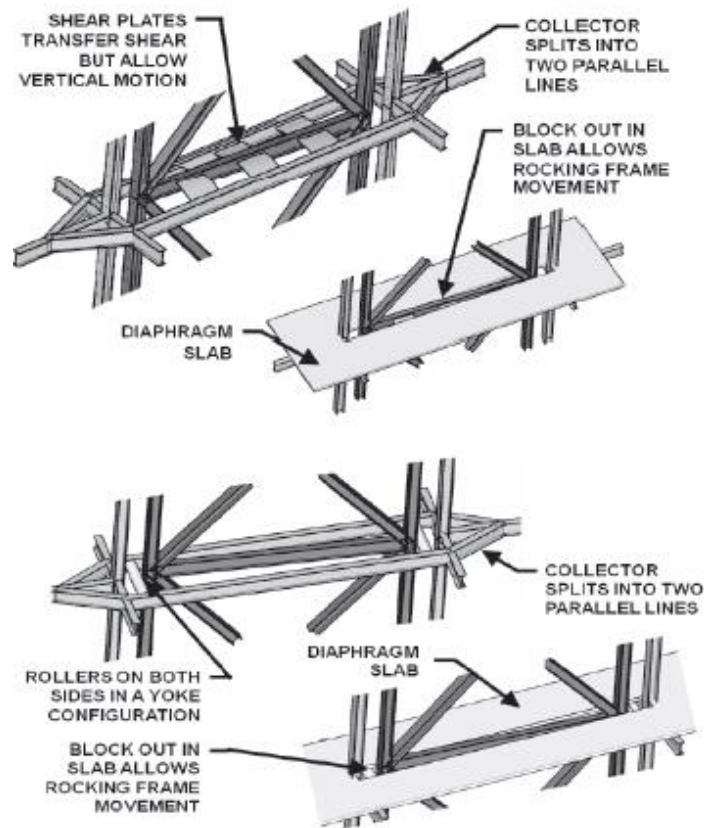


Figure 4.2 Proposed connections between gravity frame and controlled rocking frame[from Eatherton and Hajjar (2010)]

## 4.2 Seismicity and Hazard Selection for the Prototype Site

The prototype buildings are assumed to be located in Berkeley, California, United States. The proximity of the Hayward Fault to the site makes it a region of high seismicity. Table 4.2 summarizes the parameters used to define the design acceleration spectrum corresponding to DBE

hazard level according to ASCE/SEI 7-10 (2010). The MCE and SLE hazard level spectra are then linearly scaled from DBE using scale factors of 1.5 and 0.25, respectively. All the three design spectra are shown in Figure 4.3. The corresponding probability of exceedance is 2% in 50 years for MCE, 10% in 50 years for DBE and 70% in 50 years for SLE.

**Table 4.2 Parameters to define design acceleration spectrum**

<b>Parameter</b>	<b>Value</b>
S <sub>s</sub> , MCE level 5% damped spectral acceleration at short periods	2.307 g
S <sub>1</sub> , MCE level 5% damped spectral acceleration at a period of 1 sec	0.958 g
Soil Class	C
F <sub>a</sub> , short-period site coefficient	1.0
F <sub>v</sub> , long-period site coefficient	1.3
T <sub>L</sub> , long-period transition period	8 sec
S <sub>DS</sub> , DBE level 5% damped spectral acceleration at short periods	1.538 g
S <sub>DI</sub> , DBE level 5% damped spectral acceleration at a period of 1 sec	0.830 g

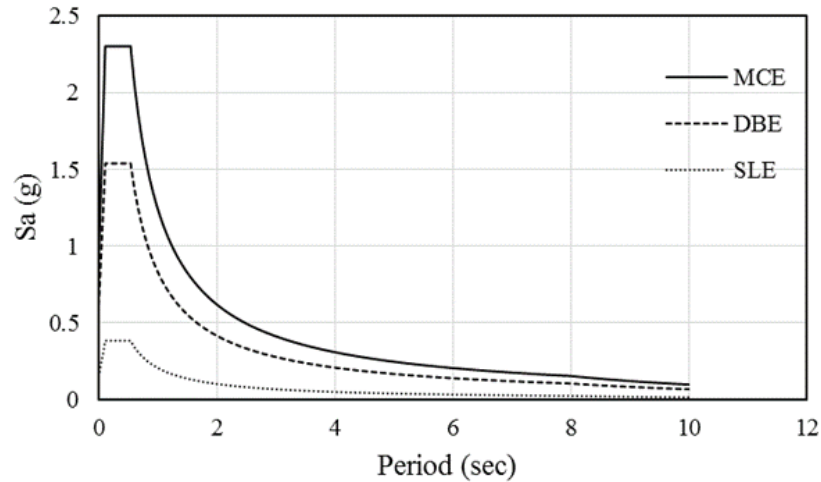


**Figure 4.3 Design acceleration spectra for Berkeley, USA**

### 4.3 Prototype Design Summary

This section briefly summarizes the CR-CBF designs that were developed according to the design methodology discussed in Chapter 3. Detailed calculations for the prototype designs are presented in the Appendix. As indicated previously, the CR-CBFs are not designed to carry any gravity load, hence the bay width of the both the prototype frames is reduced to 27 feet in order to fit between the gravity columns of the building. The storey height of both the prototypes is 15 feet. For primary SFRS, ED shall comprise of friction dampers installed at column bases on both ends of the frame. As a part of the secondary SFRS, PT shall be placed along the column lines and extend over the full height of both the prototypes. Unbonded mono-strand post-tensioning system are used for the 3-storey prototype, while post-tensioning bars shall be used for the 6-storey prototype. The properties of the post tensioning system are summarized in Table 4.3, as given by the manufacturer (DSI 2006).

**Table 4.3 Post-tensioning parameters [from DSI (2006)]**

<b>Building</b>	<b>Type of PT</b>	<b>Yield Strain</b>	<b>Modulus of Elasticity</b>	<b>Yield Stress</b>	<b>Ultimate Stress</b>
3-storey	Strand	0.0087	28000 ksi	243 ksi	270 ksi
6-storey	Bar	0.004	29700 ksi	120 ksi	150 ksi

### 4.3.1 3-Storey Prototype

The 3-storey prototype has a total height of 45 feet and a bay width of 27 feet. Hence,  $d_{PT}$  and  $d_{ED}$  are equal to 45 feet and 27 feet, respectively. Table 4.4 shows the parameters required by EEDP to design this frame. The building has two CR-CBFs in each orthogonal direction. Hence, the seismic weight  $W$  per frame in each direction is 2994 kips. Figure 4.4 represents the force-deformation backbone of the system, computed using the parameters of Table 4.4. Figure 4.5 shows the final layout. Detailed calculations are presented in the Appendix A.

**Table 4.4 EEDP design parameters for 3-storey prototype**

<b>Parameter</b>	<b>Value</b>	<b>Remark</b>
$W$	2994 kips	Given
$C_0$	1.30	From ASCE/SEI 41-06 (2007)
$\Delta_y$	0.15%	User defined
$F_y$	0.3845*W	From Figure 4.4
$\Delta_p$	0.90%	User defined
$T$	0.4 sec	From Equation [3.12]

Parameter	Value	Remark
$\gamma_a$	1.25	From Figure 3.7
$F_p$	0.5421*W	From Equation [3.14]
$\gamma_b$	1.15	From Figure 3.8
$\Delta_u$	1.83%	From Equation [3.16]

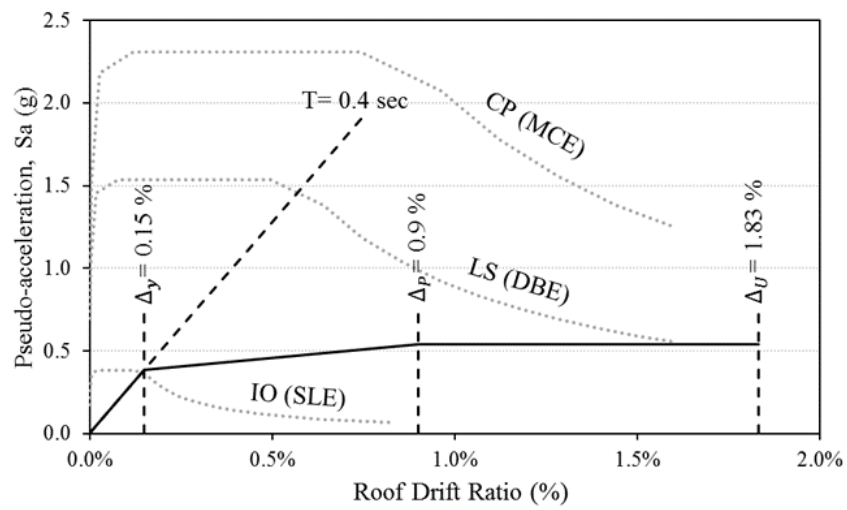
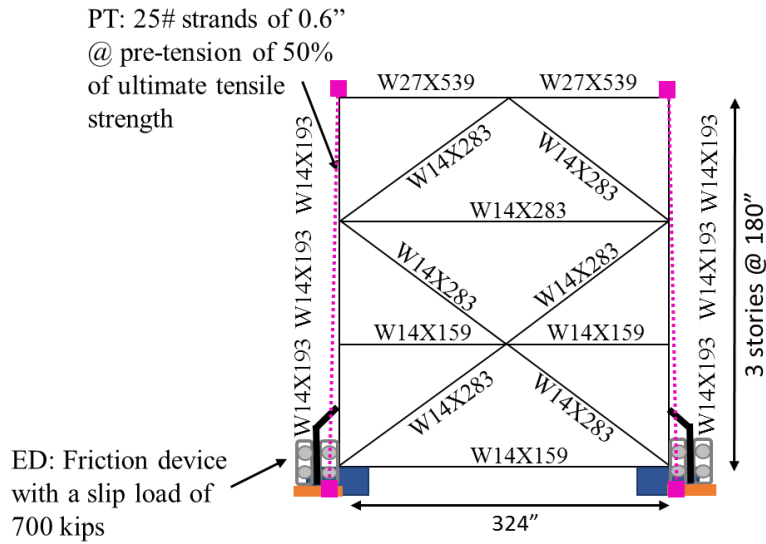


Figure 4.4 EEDP force-deformation backbone of 3-storey CR-CBF prototype



**Figure 4.5 Final layout of 3-storey CR-CBF prototype**

### 4.3.2 6-Storey Prototype

The 6-storey prototype has a total height of 90 feet and a bay width of 27 feet. Hence,  $d_{PT}$  and  $d_{ED}$  are equal to 90 feet and 27 feet, respectively. Table 4.5 shows the parameters required by EEDP to design this frame. The building has two CR-CBFs in each orthogonal direction. Hence, the seismic weight  $W$  per frame in each direction is 6400 kips. Figure 4.6 represents the force-deformation backbone of the system, computed using the parameters of Table 4.5. Figure 4.7 shows the final layout of the prototype with the chosen sections satisfying the requirements of ANSI/AISC 360-10 (2010), designed using EEDP. Detailed calculations are presented in the Appendix B.

**Table 4.5 EEDP design parameters for 6-storey prototype**

Parameter	Value	Remark
$W$	6400 kips	Given
$C_0$	1.42	From ASCE/SEI 41-06 (2007)
$\Delta_y$	0.22%	User defined
$F_y$	$0.2525*W$	From Figure 4.4
$\Delta_p$	0.92%	User defined
$T$	0.8 sec	From Equation [3.12]
$\gamma_a$	1.85	From Figure 3.7
$F_p$	$0.3872*W$	From Equation [3.14]
$\gamma_b$	2.1	From Figure 3.8
$\Delta_u$	1.61%	From Equation [3.16]

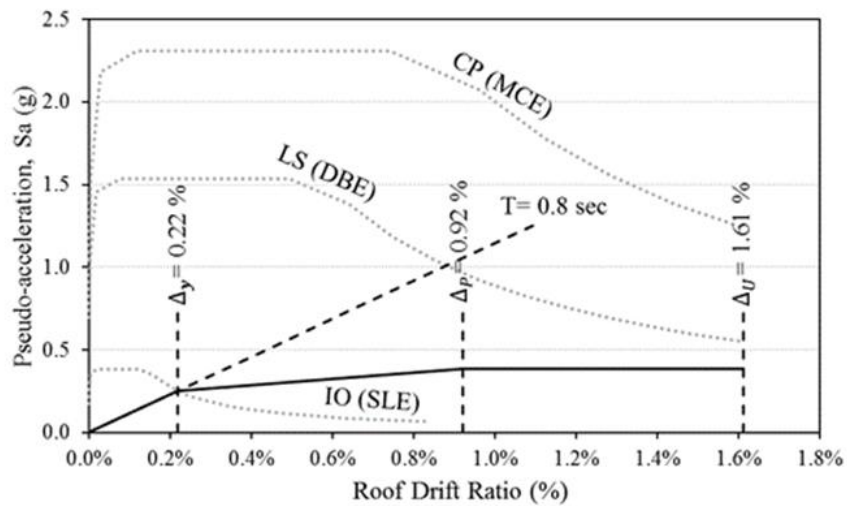


**Figure 4.6 EEDP force-deformation backbone of 6-storey CR-CBF prototype**

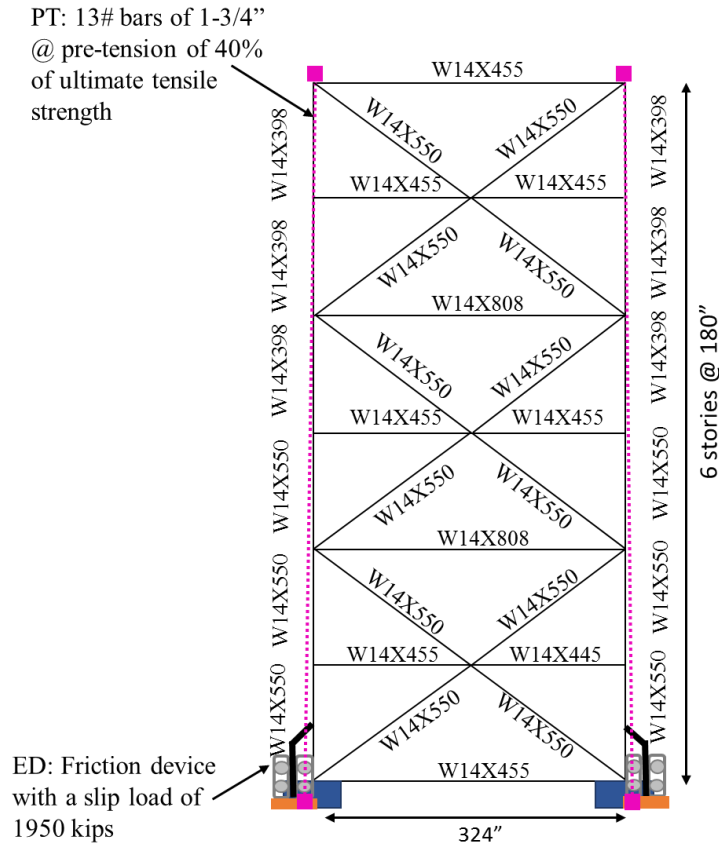


**Figure 4.7 Final layout of 6-storey CR-CBF prototype**

#### 4.4 Numerical Modelling of the Prototypes

This section describes the details of the development and calibration of the finite element models of the prototypes designed in the previous sections. These models are developed using OpenSees (2010). In this section, firstly, an overview of the numerical model is presented with the approach undertaken to simulate each component of the CR-CBF. Subsequently, the time period of the model is compared against that estimated by the EEDP to ensure comparable structural stiffness of both the design phase and modelling phase.

#### 4.4.1 Overview of the Model

Figure 4.8 shows the CR-CBF model with suitable descriptions of the elements modelled therein. All the wide-flange sections are assumed to be (ASTM A992/ A992M-11 2015) steel material and are modelled with  $f_y = 50$  ksi. Expected yield strength  $R_y f_y = 55$  ksi is used to account for any possible overstrength factors (ANSI/AISC 341-10 2010). All the beams and columns are modelled using “elastic beam-column” elements. The brace members are modelled using elastic “truss” elements. All these members are assumed to be pin-connected. Corotational transformation is applied to account for large geometric transformation. The PT tendons are modelled as nonlinear corotational truss elements. The material model for PT strands is based on quasi-static tests conducted on controlled rocking frames by Eatherton and Hajjar (2010). In these tests, the PT tendons were observed to attain ultimate stress values at approximately 1% strain. After the ultimate stress value is reached, the PT tendons start to show loss of strength up to 5% strain, at which the stress becomes zero. Similarly, the material model for PT bars is based on experimental testing on DYWIDAG tension coupons by Horan (2002). The average value of ultimate strain and fracture strain were approximately 0.9% and 7.5% respectively. A “hysteretic” material with the parameters from these experimental tests along with those given in Table 4.3 are used to define the stress-strain backbone. A “steel 02” or “Giuffré-Menegotto-Pinto” (Filippou et al. 1983) material with a very large yielding stress is implemented in series with the “hysteretic” material to impart the required prestressing force to the PT system. In addition to this, a “rigid” material with no load bearing capacity in compression is added in series to the primary PT material, to avoid the tendons from buckling under compression when the PT yields and loses its pretension significantly. The friction dampers (ED) are modelled using zero-length elements with a primary “elastic perfectly plastic” material. It has default modulus of elasticity of that of steel and suitable

yield strength corresponding to the ED design slip load. The friction dampers do not show any significant strength deterioration even after repeated hysteretic cycles. However, based on the assumption in a similar study by Ma (2010b), the friction dampers shall lose all their load-bearing capacity as soon as RDR exceeds 10% , which also indicates global structural collapse. This RDR serves as the ultimate limit state for the surrounding gravity system and represents a severe life-threatening situation requiring immediate evacuation. This loss in strength is steep and may be due to the damper plates losing complete contact to generate any frictional force. A “minmax” material is used to define a maximum allowable strain to the primary material implemented for the ED. Finally, base connections (bumpers) are modelled using zero-length “gap” elements in vertical and horizontal direction. Both these elements are modelled by “elastic no-tension” material. High compression stiffness of 10000 kip/in. is used for the vertical elements, this value is obtained from the shake table tests of a controlled rocking frame conducted by Eatherton and Hajjar (2010). The stiffness of the horizontal elements in compression is 44550 kip/in. which is obtained based on the stiffness of the shear bumpers (Midorikawa et al., 2006). These elements together simulate the contact points between the frame and the foundation and are responsible for transferring the base shear to the frame, while preventing the sliding motion and thus allow unconstrained rocking motion. All of the seismic mass is lumped at the frame nodes. Rayleigh damping of 5% at the first two modes are used.

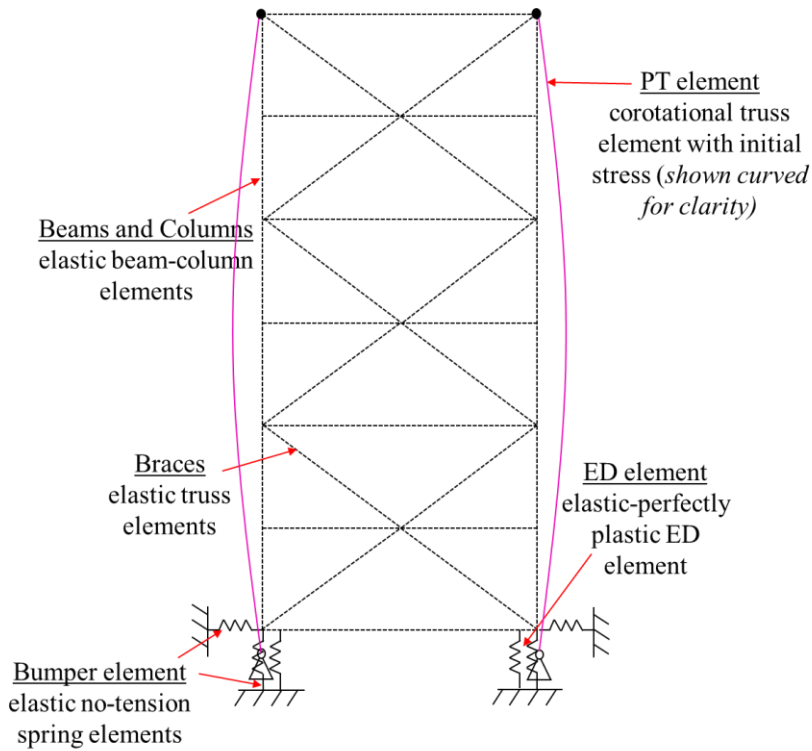


**Figure 4.8 Schematic representation of finite element model of CR-CBF**

#### 4.4.2 Comparison of Design and Model Time Period

Table 4.6 shows the comparison of the vibration periods of both the prototypes calculated using EEDP and OpenSees model. The results show that the first mode vibration period calculated using EEDP is within 15% of the predicted model. This shows the period prediction as presented in Equation [3.12] is very robust.

**Table 4.6 Comparison of design and model time period**

Building	EEDP	Finite Element	Ratio
3-storey	0.4	0.36	1.11
6-storey	0.8	0.72	1.14

## Chapter 5: Seismic Performance Assessment of CR-CBF

This chapter presents the results of the nonlinear time history analysis using a suite of ground motions of varying hazard intensities. The goal of this exercise is to confirm that the prototypes can successfully achieve the set performance targets and thus justify that EEDP can be used efficiently to design CR-CBF at different shaking intensities. Section 5.1 demonstrates the procedure of the selection and scaling of ground motions used in this study. Section 5.2 presents the seismic response of the 3-storey and 6-storey prototypes subjected to these scaled ground motions. Section 5.3 shows the comparison of the structural response of CR-CBF with that of a conventional Buckling Restraint Brace Frame (BRBF).

### 5.1 Selection and Scaling of Ground Motions

The initial step prior to execution of nonlinear dynamic analysis is the appropriate selection and scaling of the ground motions. This selection depends primarily on the location of the prototype buildings and the predominant source of earthquake hazard. The prototype building presented in this study is assumed to be located in Berkeley, California, United States. The seismic hazard at this site is dominated by the Hayward strike-slip fault which has a potential of generating magnitude  $M_w = 7$  earthquakes (UCB 2003). To find the appropriate ground motions for the site, the ground motions records were selected from PEER Strong Motion Database (PEER, 2010) with magnitude  $M_w$  between 6.5 and 7.5, distance to the fault within 10 miles and shear wave velocity at 30 meters below grade ( $V_{s30}$ ) between 1200 ft./sec and 2500 ft./sec (which is classified as Class C soil in ASCE/SEI 7-10 (2010)). The ground motions are then amplitude scaled using the guidelines of ASCE/SEI 7-10 (2010), where the mean of the scaled ground motions are selected

not to fall below the target spectrum by 10% within the period range of  $0.2T - 1.5T$ . The smaller value in the period range is defined to account for the higher mode effect, while the larger value is defined to account for period lengthening. To avoid over scaling of the ground motions, the scale factors are limited between 0.1 and 5. Table 5.1 presents the summary of the ground motions selected for this study. Figure 5.1 shows the ground motion scaling used for the three selected hazards for both prototype models.

**Table 5.1 List of ground motions with their scaling factors**

G.M. Name	Year	Magnitude	NGA#	Station	Scale factor (3-storey)			Scale factor (6-storey)		
					SLE	DBE	MCE	SLE	DBE	MCE
Friuli, Italy	1976	6.5	125	Tolmezzo	0.2	1.0	1.4	0.5	1.8	2.7
Gazli, USSR	1976	6.8	126	Karakyr	0.5	2.1	3.2	0.3	1.2	1.8
Tabas, Iran	1978	7.35	139	Dayhook	0.4	1.7	2.6	0.5	2.1	3.1
Morgan Hill	1984	6.19	451	Coyote Lake Dam	0.4	1.7	2.6	0.2	1.0	1.4
Morgan Hill	1985	6.19	459	Gilroy Array	0.5	1.9	2.9	0.5	2.0	3.0
Nahanna, Canada	1985	6.76	495	Site 1	0.3	1.3	1.9	0.4	1.7	2.5
Nahanna, Canada	1989	6.76	496	Site 2	0.5	1.9	2.8	0.6	2.5	3.8
Loma Prieta	1989	6.93	741	BRAN	0.4	1.7	2.6	0.3	1.1	1.7
Loma Prieta	1989	6.93	753	Corralitos	0.4	1.8	2.7	0.3	1.2	1.8
Loma Prieta	1992	6.93	802	Saratoga- Aloha Ave	0.3	1.0	1.5	0.6	2.3	3.5
Cape Mendocino	1992	7.01	825	Cape Mendocino	0.6	2.4	3.6	0.2	0.9	1.3
Landers	1992	7.28	879	Lucerne	0.3	1.4	2.1	0.6	2.3	3.5
Northridge	1994	6.69	1013	LA Dam	0.6	2.6	3.9	0.4	1.6	2.3
Kobe, Japan	1995	6.9	1111	Nishi- Akashi	0.2	1.0	1.5	0.6	2.4	3.6

G.M. Name	Year	Magnitude	NGA#	Station	Scale factor (3-storey)			Scale factor (6-storey)		
					SLE	DBE	MCE	SLE	DBE	MCE
Northridge	1994	6.69	1004	Sepulveda VA Hospital	0.3	1.1	1.7	0.3	1.0	1.5
Northridge	1994	6.69	989	LA Dam	0.5	2.2	3.3	0.5	2.2	3.3
Chi-Chi, Taiwan	1999	7.62	1182	CHY006	0.2	0.7	1.1	0.4	1.6	2.5
Northridge	1994	6.5	983	Jensen Filter Plant	0.4	1.7	2.5	0.4	1.6	2.3
Chi-Chi, Taiwan	1999	7.62	1512	TCU078	0.4	1.6	2.4	0.5	2.0	3.0
Hector Mine	1999	7.13	1787	Hector	0.7	2.9	4.3	0.5	2.1	3.1

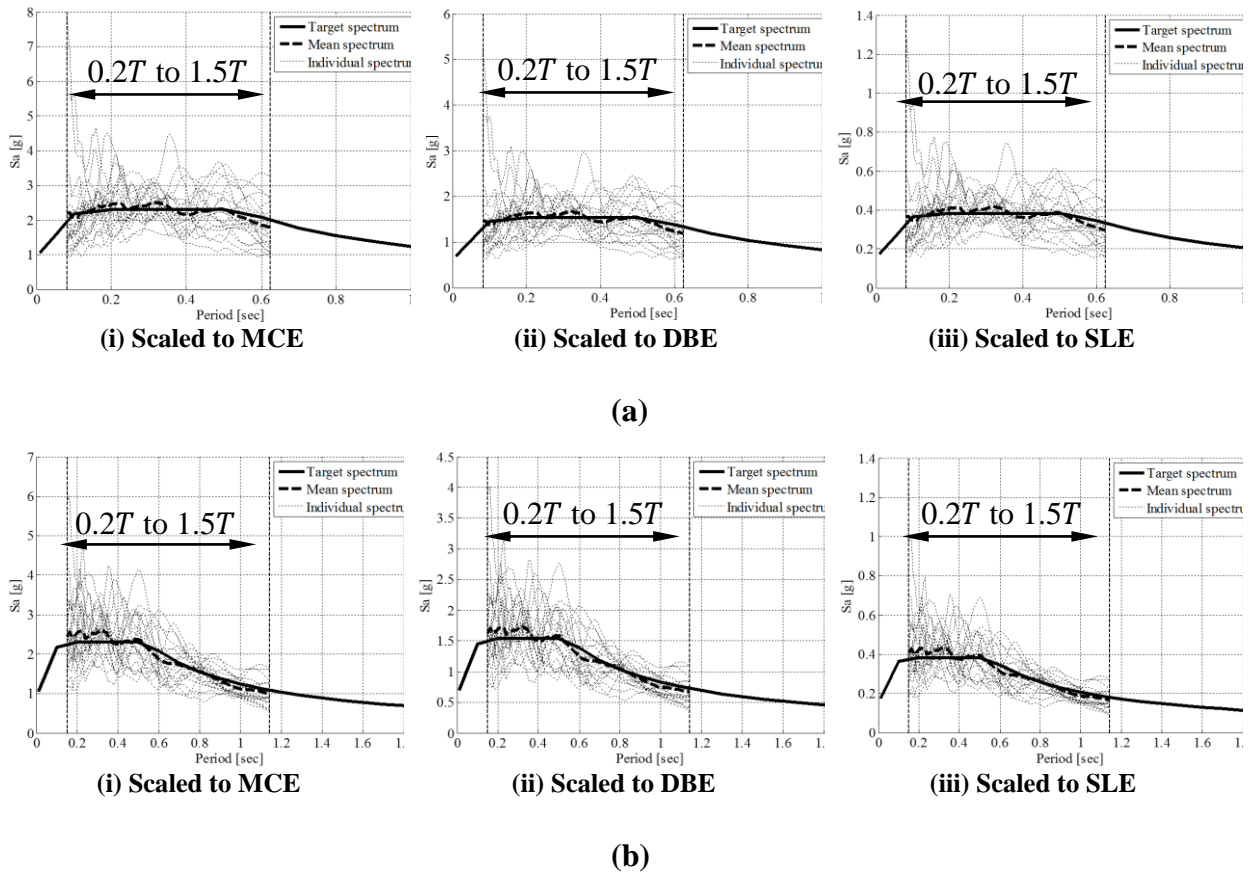


Figure 5.1 Response spectra of scaled ground motions for (a) 3-storey and (b) 6-storey prototype

## 5.2 Seismic Response of 3-storey and 6-storey Prototype Buildings

This section discusses the results of the nonlinear time-history analyses of the 3-storey and 6-storey prototype buildings, using the scaled ground motions presented in Table 5.1. Section 5.2.1, shows the plots of the peak forces in the yielding components. Section 5.2.2 evaluates the ability of EEDP to design prototype buildings to achieve the desired structural response. Section 5.2.3 investigates the residual displacements of the prototype buildings designed using EEDP.

### 5.2.1 Peak Forces in the ED and PT

Figures 5.2a and 5.2b show the median peak forces in both the yielding components (PT and ED) normalized by their respective design yield force. The results show that at the SLE hazard intensity, both the PT and ED are far below yielding. In fact, the peak PT force is at the initial prestressed force. This shows that these elements still behave elastically. This confirms that both prototype models are able to achieve the IO target performance as intended. For the DBE hazard intensity, PT for both models are precluded from yielding, while the ED reached the peak design force. This shows that both the prototypes are able to achieve the LS performance target. Lastly, for the MCE hazard intensity, both the PT and ED reached to its design yielding forces. It should be noted that PT and ED is assumed to keep its strength after yielding, in other words, do not show any strength deterioration/failure. Hence, the CR-CBF can achieve the CP performance level. Another important consideration for rocking frames is the phenomenon of *Global Uplift*, wherein the downward force in the PT (following loss of prestress due to yielding) is no longer able to overcome the upward force in the ED. This phenomenon leads to complete uplift of the frame and rotation about the ED without any action of PT. However, it is seldom seen in CR-CBFs, since the ED is placed at both corners of the frame, which prevents the occurrence of this phenomenon.

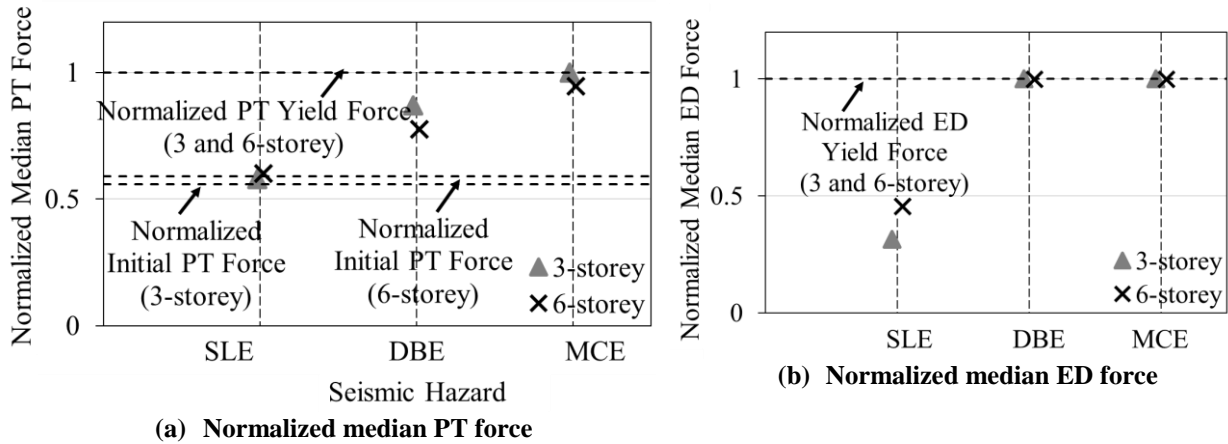
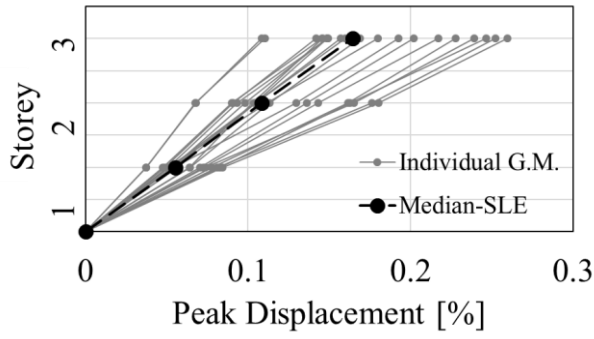


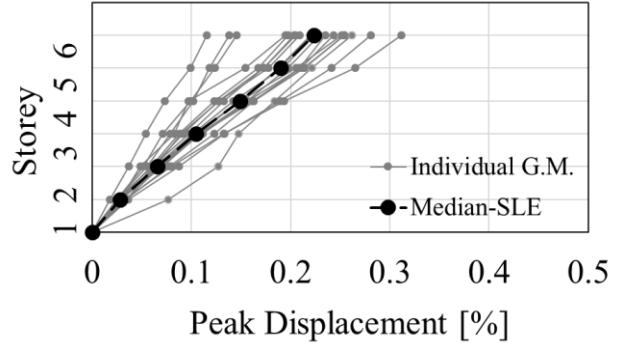
Figure 5.2 Normalized median forces in (PT) and (ED) due to various seismic hazard intensities

### 5.2.2 Peak Displacements

In this section, the peak displacements in the 3-storey and 6-storey prototype buildings are investigated and compared with the displacement targets chosen at the onset of the EEDP procedure. Figures 5.3, 5.4 and 5.5 show the peak displacements, normalized by the building height, for both the prototypes under SLE, DBE and MCE seismic hazard intensities, respectively. Figure 5.6 shows the medians of peak interstorey drift ratios (ISDR), for both the prototypes under all the three seismic hazard intensities. It also shows the medians of peak base rotation under different seismic hazard intensities by vertical lines at the base. The peak displacement envelopes have an approximately linear profile, which reaffirms that the seismic response of these systems is dominated by the rigid-body rocking motion. As evident in Figure 5.6, the lateral stiffness of the frames also contributes to these displacements making them slightly greater than their corresponding base-rocking displacements.

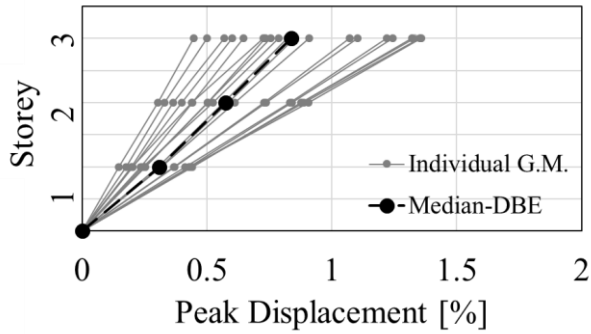


(a) 3-storey prototype- SLE

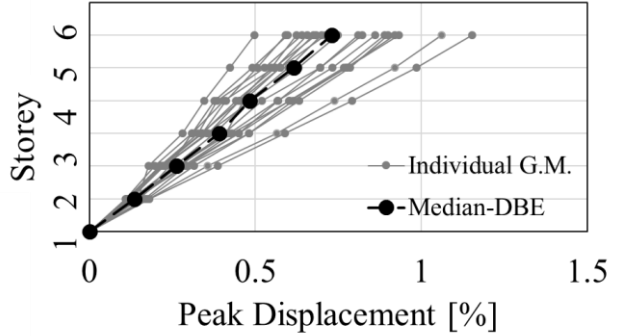


(b) 6-storey prototype- SLE

Figure 5.3 Peak displacements in (a) 3-storey and (b) 6-storey prototype under SLE seismic hazard intensity

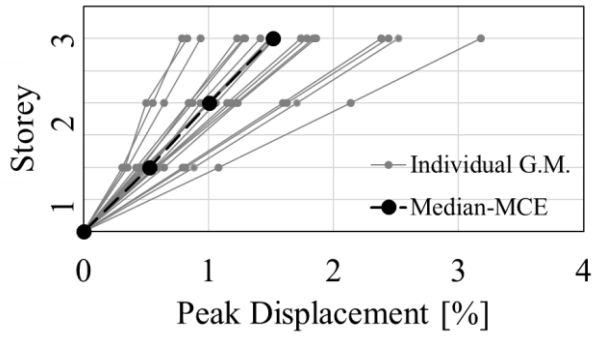


(a) 3-storey prototype- DBE

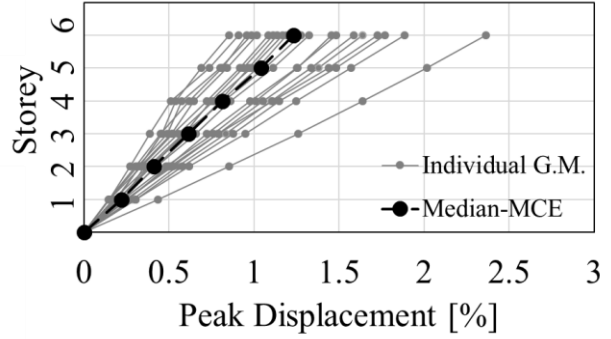


(b) 6-storey prototype- DBE

Figure 5.4 Peak displacements in (a) 3-storey and (b) 6-storey prototype under DBE seismic hazard intensity

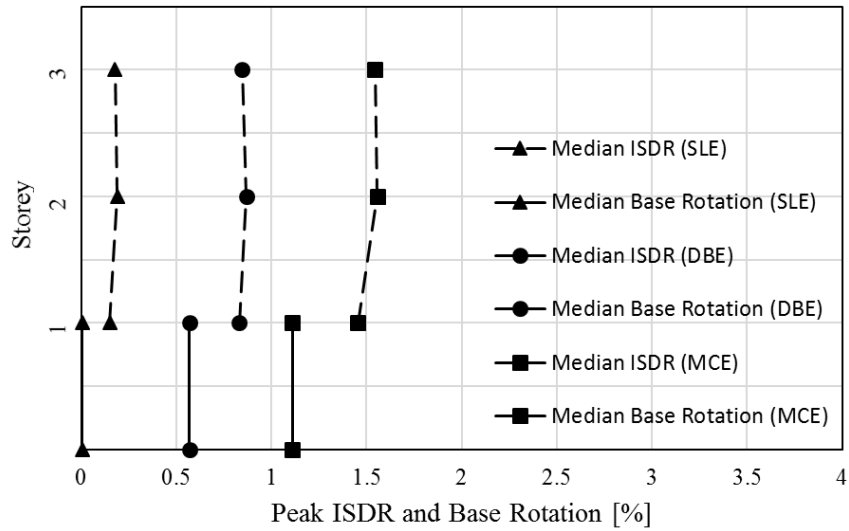


(a) 3-storey prototype- MCE

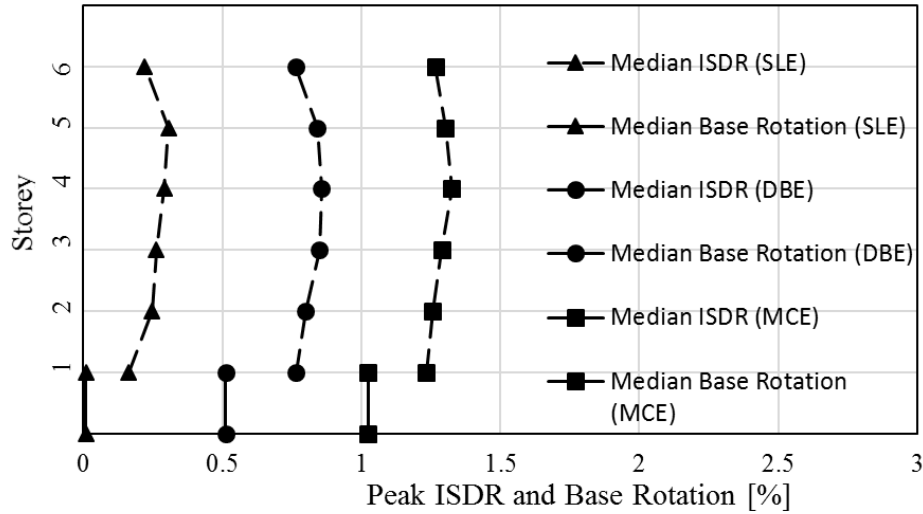


(b) 6-storey prototype- MCE

Figure 5.5 Peak displacements in (a) 3-storey and (b) 6-storey prototype under MCE seismic hazard intensity



(a)



(b)

**Figure 5.6 Peak median ISDR and base rotation in (a) 3-storey and (b) 6-storey prototype under all three seismic hazard intensities**

Figure 5.7 shows the comparison of the median RDRs obtained from the time history analysis and compared against the target RDRs initially selected. At the SLE hazard level, the median roof drift ratios of the 3- and 6-storey prototypes are approximately 0.15% and 0.22%, respectively. These values are very close to the targets ( $\Delta_y$ ). At the DBE hazard level, the median roof drift ratios are about 0.83% and 0.74% for the 3- and 6-storey prototypes, respectively. Finally, at the MCE hazard level, the median roof drift ratios are about 1.50% and 1.23% for the 3- and 6-storey prototypes, respectively. These values are lesser than the targets ( $\Delta_p$ ) and ( $\Delta_u$ ), shown in Figure 5.7, to indicate that the CR-CBFs designed by EEDP have conservative displacements.

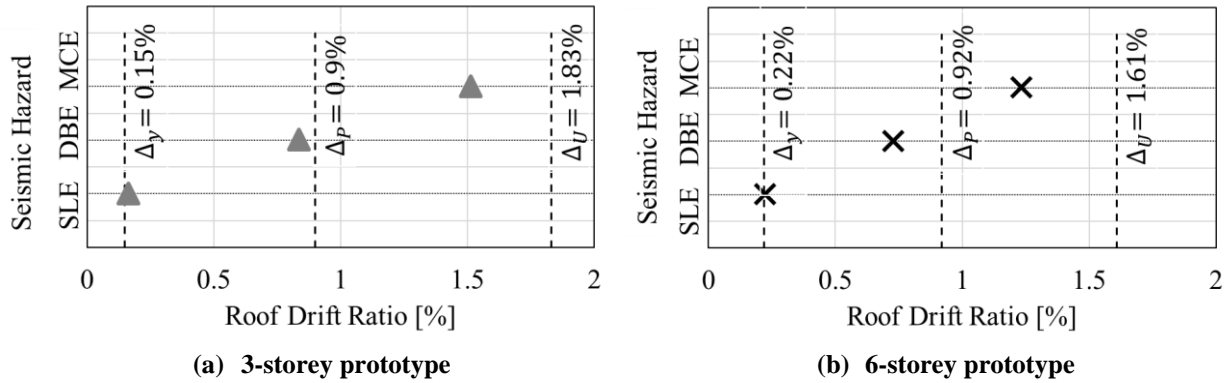


**Figure 5.7 Comparison of median and target roof drift ratios of (a) 3-storey and (b) 6-storey prototype under various seismic hazard intensities**

### 5.2.3 Residual Displacements

CR-CBFs are resilient SFRSs which are designed to have minimal residual deformation. Figure 5.8 shows the interstorey residual drift ratios (IRDRs) of the 3-storey and 6-storey prototype buildings at MCE hazard level. Referring to the previous research by McCormick et al. (2008), the value of permissible residual drift ratio is assumed to be 0.5%. The maximum median IRDR for the 3-storey prototype is observed at the roof with a value of 0.02%. Although two ground motions elicit IRDRs greater than the permissible limits for the 6-storey prototype, the median IRDRs are still safely within the permissible limit. The maximum median IRDR for the 6-storey prototype occurs at the fifth storey, with a value of 0.07%. These residual displacements can be easily removed by replacing the yielding components of the CR-CBF system, thereby expediting the post-earthquake re-occupation of the building, without affecting its functionality.

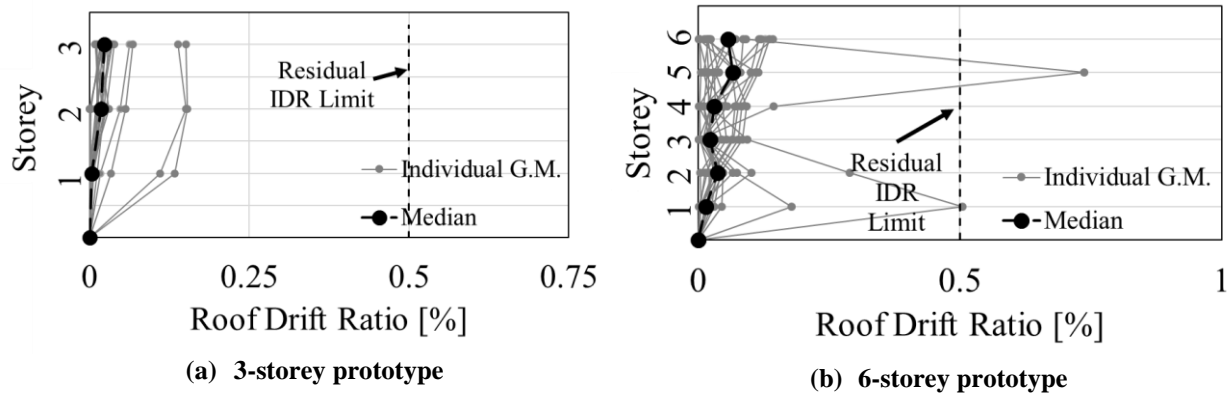


Figure 5.8 IRDRs of (a) 3-storey and (b) 6-storey prototype under MCE seismic hazard intensity

### 5.3 Comparison of Seismic Performance of CR-CBF with BRBF

To promote the application of CR-CBF in areas of high seismic activities, the seismic response of these systems is compared with a BRBF. Section 5.3.1 summarizes the BRBF prototype geometry and design strategy. Section 5.3.2 presents the comparative results of nonlinear dynamic analyses,

#### 5.3.1 Description of BRBF Prototype Geometry and Design

The BRBF prototypes considered in this study have a conventional chevron-braced concentrically braced configuration. For direct comparison, the geometric detailing of the BRBFs, such as storey height, bay width, seismic weight, etc., are assumed to be exactly the same as the CR-CBFs. Just like the CR-CBFs, both the three and six-storey BRBFs are assumed to be located in Berkeley, California. Hence, the hazards chosen for the analysis and design of these systems are also the same and can be obtained from Section 4.2. The seismic design procedure adopted for the BRBF prototypes is based on the conventional building code ASCE/SEI 7-10 (2010). Figure 5.9 shows the final design layout of the 3-storey and 6-storey BRBF prototypes. The BRBs are shown

with the required area,  $A_R$  (in<sup>2</sup>) and corresponding sections can be obtained from the manufacturers.

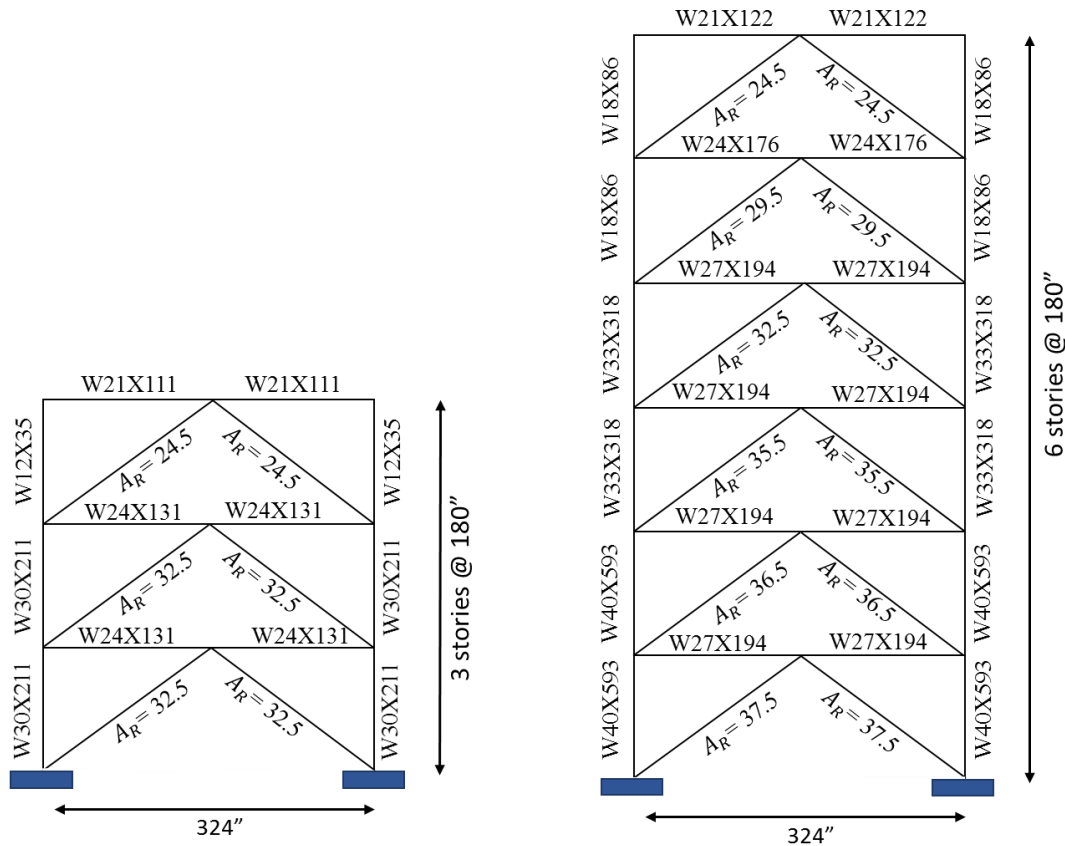


**Figure 5.9 Final design layout of 3-storey and 6-storey BRBF prototypes**

### 5.3.2 Seismic Response of Systems

The numerical models of the BRBF prototypes are generated using the same modeling approach as the CR-CBFs, as described in Section 4.4. The model time periods of both the 3-storey and 6-storey prototypes are very close to the design time periods of the CR-CBFs, i.e. 0.4 sec for 3-storey and 0.8 sec for 6-storey. Hence, the seismic response of these models are evaluated using nonlinear dynamic analyses using the same suite of ground motions, given in Table 5.1. The following

sections present the results of the analyses for the BRBF prototypes and compare them with the corresponding structural response parameters of the CR-CBFs.

### **5.3.2.1 Peak Displacements**

Similar to the CR-CBFs, the peak floor displacements of the BRBF prototypes are normalized by their respective building heights. Figure 5.9 shows the median values of the normalized peak floor displacements for ground motions presented in Table 5.1. The result shows that the median peak displacements in the 6-storey BRBF (Figure 5.10) are quite comparable to the median peak displacements of its CR-CBF (Figures 5.3, 5.4 and 5.5). But the median peak displacements in the 3-storey BRBF are slightly lower than its CR-CBF counterpart, particularly for DBE and MCE hazard intensities. However, major part of the displacements in CR-CBFs is due to rigid body rocking motion and not due to lateral deformations in the frame. In other words, the seismic response of CR-CBFs is due to geometric nonlinearity and not due to material nonlinearity. Hence, these greater displacements do not directly translate into any major structural damage in these systems. In fact, as already stated, one of the key advantages of using CR-CBFs is to preclude yielding and damage to the frame members at all seismic hazard intensities. On the other hand, both the BRBF prototypes exhibit significant yielding of the frame members. This would result in greater repair costs and downtime which adversely affect the building performance.

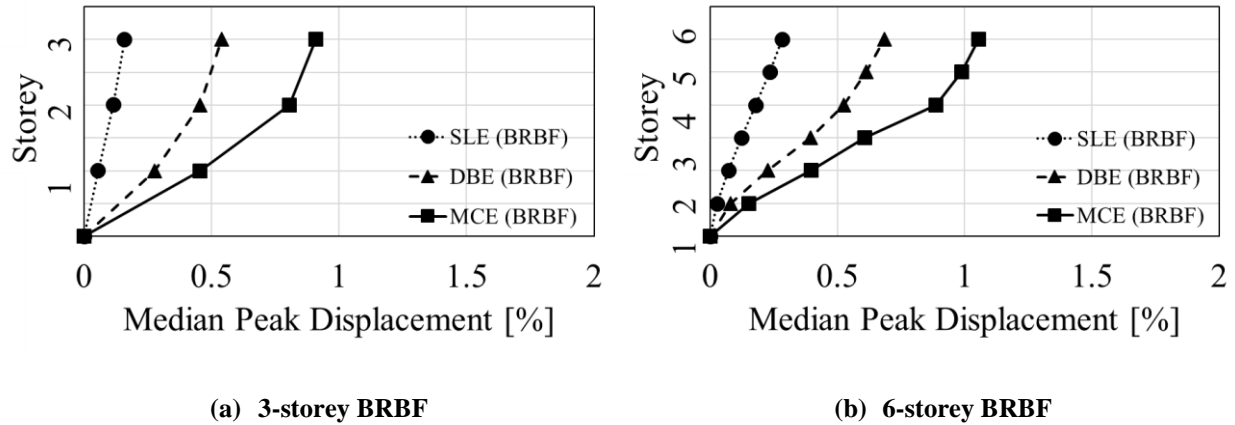
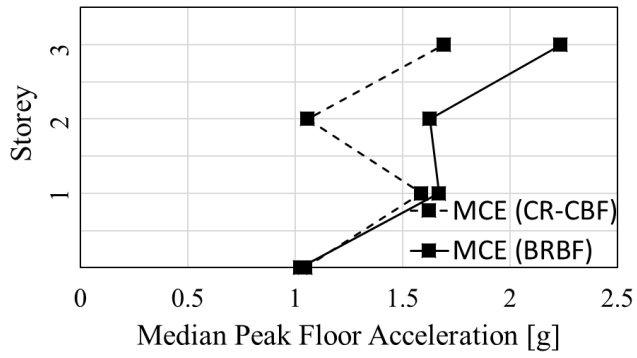
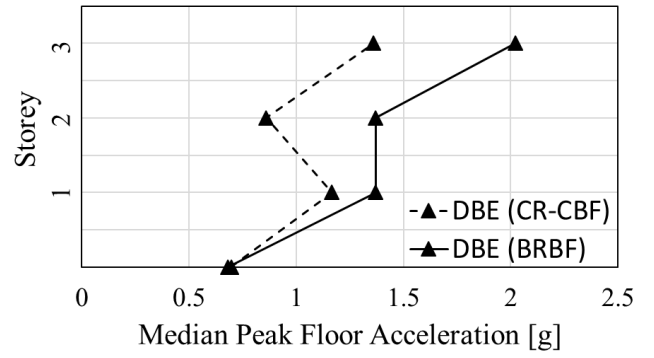
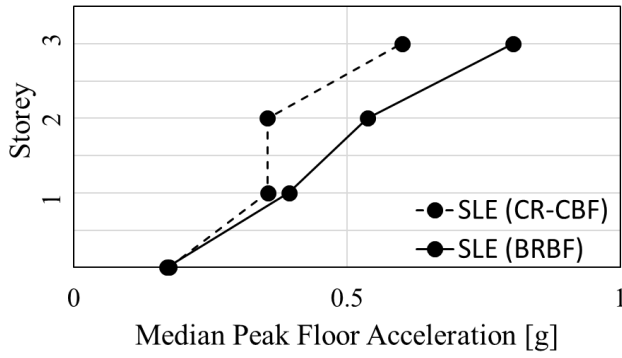


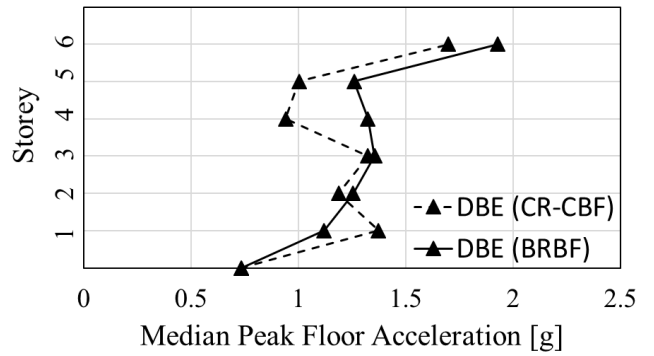
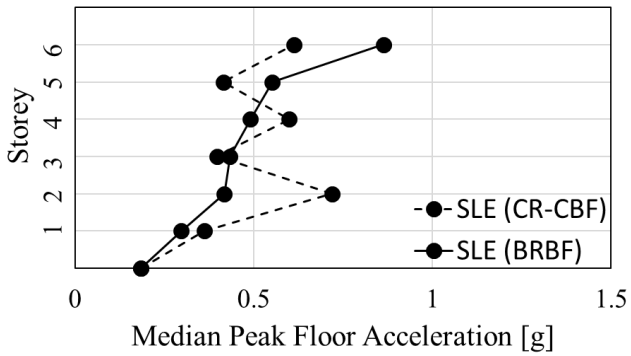
**Figure 5.10 Median of peak displacements in (a) 3-storey and (b) 6-storey BRBF prototypes under all three seismic hazard intensities**

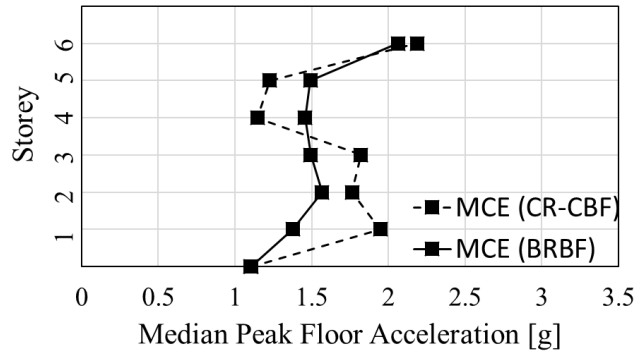
### 5.3.2.2 Peak Accelerations

The analysis of peak floor accelerations reveals the performance of non-structural performance and the estimation of diaphragm loads for design of collector beams for SFRSs. Figure 5.11 shows the comparison of median values of the peak floor accelerations between CR-CBF and BRBF prototypes, for all the 20 ground motions corresponding to each hazard intensity. In the case of 3-storey prototypes, the median peak floor acceleration of the BRBF system is generally higher (approximately 40% higher at the top storey) than that of the corresponding CR-CBF system. On the other hand, in the case of 6-storey prototypes, the variability of median peak floor accelerations across the height for both the systems is inconsistent. The observed trend is that the accelerations at the bottom three storeys of the CR-CBF prototype are higher than that of the BRBF prototype and vice-versa for the top three storeys. From these results, it is rather tough to establish a generalized conclusion about the comparison of floor accelerations in both the systems. More prototype designs of varying heights and configurations need to be considered for better understanding of this aspect.



(a)





(b)

**Figure 5.11 Comparison of median of peak floor accelerations in (a) 3-storey and (b) 6-storey CR-CBF and BRBF prototypes under all three seismic hazard intensities**

### 5.3.2.3 Residual Displacements

The evaluation of residual displacements in the structure reveals the extent of damage accumulation through yielding of structural components. Figure 5.12 shows the comparison between median IRDRs of the 3-storey and 6-storey CR-CBF and BRBF prototype buildings at MCE hazard level. Around the mid-height of the structures, the 3-storey BRBF prototype shows IRDR as high as 0.39%, while the 6-storey BRBF prototype shows a maximum of 0.31%. These values are considerably higher than the IRDRs in CR-CBFs. Although within the maximum permissible limit of 0.5%, the significant amount of residual displacements in these buildings heavily compromise the safety of occupants and the structural functionality of the buildings. Hence, BRBFs are highly vulnerable to damage and accumulation of residual displacements, which may require hefty repair works after a strong earthquake.

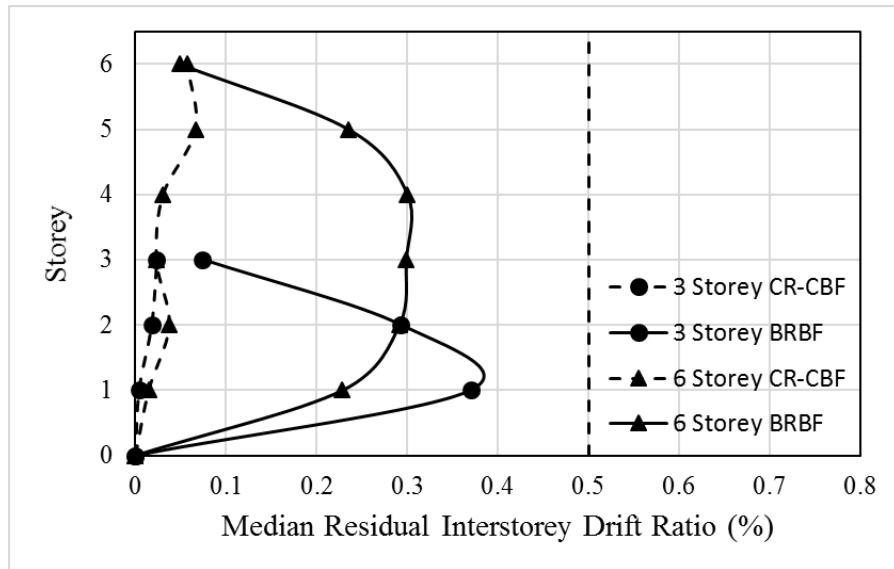


**Figure 5.12 Comparison of median IRDRs of 3-storey and 6-storey CR-CBFs and BRBF prototype under MCE seismic hazard intensity**

## Chapter 6: Collapse Margin of Safety Assessment of CR-CBF

In this chapter, the collapse margin of safety for CR-CBF system is assessed using the FEMA P695 (2009) procedure. The goal of this exercise is to ascertain that the system retains sufficient margin of safety against collapse under the MCE hazard level. Section 6.1 briefly discusses the FEMA P695 (2009) methodology which includes the various steps to be undertaken for comprehensive collapse margin of safety against collapse. Section 6.2 presents the results of the collapse safety assessment for the 3-storey and 6-storey CR-CBF prototypes.

### 6.1 Overview of Collapse Safety Assessment Methodology

The Applied Technology Council (ATC), under the direction of Federal Emergency Management Agency (FEMA), developed the FEMA P695 (2009) procedure. The primary objective of this methodology is to reliably quantify the global seismic performance factors (response modification coefficient,  $R$ , system overstrength factor,  $\Omega$ , and deflection amplification factor,  $C_d$ ) to be used in the seismic design of structures, resulting in a very low probability of collapse under severe (MCE) ground motions.

According to the methodology, the collapse margin of safety assessment of a structural system comprises of six major tasks as shown in Figure 6.1. They are:

- (i) ***Develop system concept:*** The procedure calls for a thoroughly defined concept for the SFRS, including the material of construction, mechanisms of inelastic energy dissipation, system configuration and intended range of applications.

- (ii) ***Design provisions and structural behavior:*** The procedure initiates by gathering all the relevant seismic design provisions that were employed in the design and detail of the SFRS and its components. These may include seismic provisions of ASCE/SEI 7-10 (2010) or other applicable building codes. The design requirements also include system test data, including information on material properties, nonlinear responses and force-deformation backbones. The structural system behavior is characterized through the use of “archetypes”. These structural archetypes only include limited yet vital parameters and configurations of the SFRS, whose performance directly reflects the collapse risk of the system. They may include building height, fundamental period, framing bay widths, connection detailing, hazard intensity, etc. These are classified into separate performance-groups, which sufficiently represent the possible variations in system behavior within the structural archetype.
- (iii) ***Develop nonlinear models:*** The structural archetypes define a range of intended structural applications and behavioral modes. Corresponding nonlinear numerical models are generated which include all possible strength deterioration mechanisms that could lead to collapse. The nonlinear models of the components should be calibrated using material test data to verify its ability to simulate the expected nonlinear behavior. The numerical models should be able to simulate all significant number of collapse modes possible in the structure.
- (iv) ***Assess collapse performance:*** Collapse safety assessment is performed by implementing both nonlinear static (pushover) and nonlinear dynamic (time history) analyses. The pushover analysis is used to statistically estimate the seismic performance factors as shown in Figure 6.2. The vertical axis represents 5% damped spectral acceleration values and the horizontal

axis represents the corresponding spectral displacement values for various fundamental periods. As shown in the figure, the FEMA P695 methodology defines these performance factors by relating them with MCE hazard spectra. Response modification coefficient,  $R$ , is defined as the ratio of spectral acceleration that would be developed in an equivalent linearly elastic system for DBE hazard intensity, to the design spectral acceleration. This can be related to the MCE spectral acceleration,  $S_{MT}$  and seismic response coefficient,  $C_s$  as represented by Equation [6.1]. The factor 1.5 in the Equation is consistent with the ASCE/SEI 7-10 guidelines, where DBE hazard intensity is two-thirds of MCE hazard intensity.

$$R = \frac{S_{MT}}{1.5 \times C_s} \quad [6.1]$$

The overstrength parameter,  $\Omega$ , is defined as the ratio of the maximum strength of the yielded system,  $S_{max}$ , to the design spectral acceleration or the seismic response coefficient,  $C_s$ .

$$\Omega = \frac{S_{max}}{C_s} \quad [6.2]$$

Deflection amplification factor,  $C_d$ , is defined as the ratio of DBE spectral displacement of the yielded system to the spectral displacement of the linearly elastic system corresponding to design seismic coefficient,  $C_s$ .  $C_d$  can be related to MCE spectral displacement of the linearly elastic system,  $SD_{MT}$ , and MCE spectral displacement of the yielding system using equal displacement rule, as given by:

$$1.5 \times C_d \times \frac{SD_{MT}}{1.5 \times R} = SD_{MT} \quad [6.3]$$

or

$$C_d = R \quad [6.4]$$

Nonlinear dynamic analysis is performed on the archetypes using a pre-defined suite of ground motions to evaluate the median collapse capacity of each archetype. Using this value, a

collapse fragility curve is generated which relates probability of collapse to spectral acceleration.

- (v) **Evaluate collapse margin:** For nonlinear collapse simulations, the methodology defines collapse level ground motions as the intensity at which at least half of the ground motions cause structural collapse, either through a sideways collapse mechanism or exceeding any critical limit state. As shown in Figure 6.2, the system collapse safety margin, or the collapse margin ratio (*CMR*) is defined as the ratio of the median spectral acceleration of the collapse intensity,  $\hat{S}_{CT}$  (or corresponding spectral displacement,  $SD_{CT}$ ), to the MCE spectral acceleration,  $S_{MT}$  (or corresponding spectral displacement,  $SD_{MT}$ ), at the fundamental period of the SFRS.

$$CMR = \frac{\hat{S}_{CT}}{S_{MT}} = \frac{SD_{CT}}{SD_{MT}} \quad [6.5]$$

An adjusted collapse margin ratio (*ACMR*) is then calculated to account for the influence of spectral shape, using spectral shape factor (*SSF*), given by:

$$ACMR = SSF \times CMR \quad [6.6]$$

To ensure the probability of collapse at  $S_{MT}$  is less than 10%, the value of *ACMR* needs to exceed a threshold value,  $ACMR_{10\%}$ . This threshold value is determined by taking into account different sources of uncertainties like ground motion record-to-record, design requirements, test data and modeling technique.

- (vi) **Documentation and Peer review:** The results of each of the steps in the process need to be thoroughly documented for the review and approval by an independent panel of peer reviewers.

Documentation should be comprehensive and include all the details of seismic design rules, range of applicability of the system, selection of structural system archetypes, results of performance evaluation and so on. Consultation with a team of experts for peer review is an indispensable part of the process at every step. The peer reviewers are responsible for assessing and commenting on the approach taken by the structural development team regarding quality of test data, development of system archetypes, nonlinear analysis strategy and the final selection of seismic performance factors.

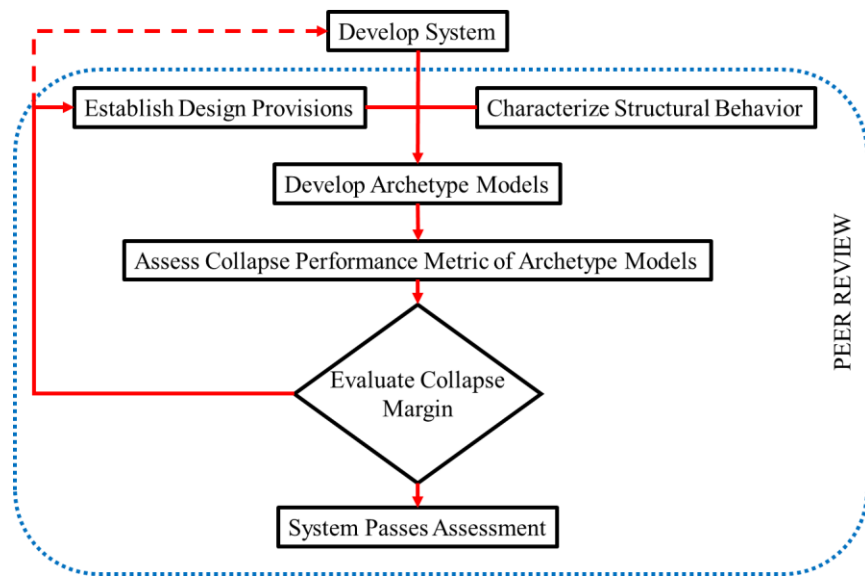


**Figure 6.1 FEMA P695 (ATC 63) collapse safety assessment procedure (after Deierlein et al. (2008))**

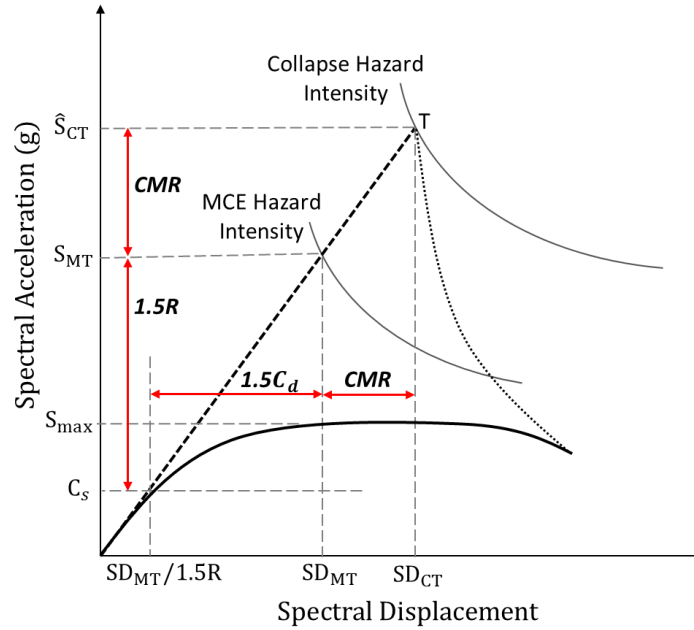


Figure 6.2 Seismic performance factors (from FEMA P695 (2009))

## 6.2 Evaluation of Collapse Safety for CR-CBF Prototypes

In this thesis, only the key aspects of the FEMA P695 (2009) methodology are implemented. Steps (i), (ii), (iv) and (v) are implemented fully. However, the system archetypes developed here constitute only a subset of the different archetypes required in step (iii). More archetypes and performance groups are needed for a comprehensive representation of system behavior. Step (vi) is out of scope for this study and is not implemented here. Despite lacking these steps, the limited version of the methodology implemented in this study suffices the purpose of investigating the system collapse safety performance.

The possible modes of structural collapse in a CR-CBF are: (i) Overturning of the rocking frame due to fracture of the designated yielding components, i.e. PT and ED; (ii) Excessive yielding or fracture of any other CBF member; (iii) Failure of bumpers at the base leading to failure at the rocking base; (iv) Failure of collector beams and subsequent failure of the gravity system

components attached to the SFRS. Firstly, the analysis of gravity system is out of scope of this study, and secondly, the study explicitly assumes the preclusion of damage or failure of the CBF members and base connections. As already assumed in Section 4.4, the criterion for structural collapse is assumed to be 10% RDR for both the prototypes. Hence, the collapse of CR-CBF is assumed exclusively to be due to mode (i) as soon as the RDR exceeds 10%. This assumption simplifies the modeling procedure but can be subjected to further verification to ascertain its general validity. The collapse analysis of CR-CBF requires almost identical numerical models as explained in Section 4.4. Since the yielding of frame members is precluded from this study, their material model shall remain elastic. Only the material models for PT and ED need to include the effects of strength degradation and subsequent fracture.

As explained in Section 6.1, the first step in the collapse-safety evaluation is to perform nonlinear static analysis using the numerical model. Figure 6.3 shows the pushover curve generated for both the 3-storey and 6-storey CR-CBF prototypes. According to FEMA P695 (2009), the period-based ductility,  $\mu_T$ , is defined as the ratio of  $RDR_u$  and  $RDR_y$ , which is 12 for the 3-storey prototype and 13 for 6-storey prototype. For both the prototypes, it can be clearly seen that both PT and ED do not yield prior to the performance objectives selected during the EEDP design phase as listed in Tables 4.4 and 4.5. In other words, EEDP designed CR-CBF prototypes practically achieve the stipulated performance objectives.

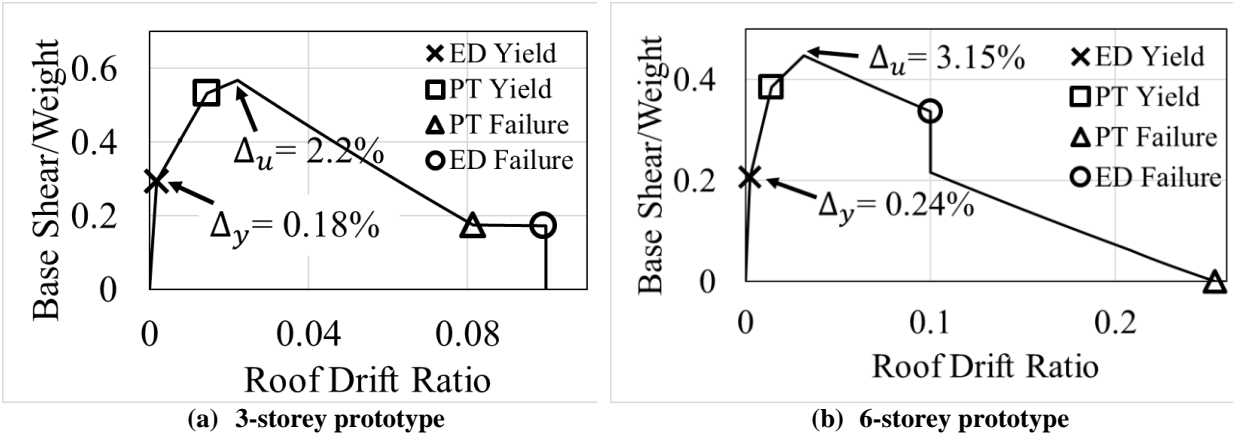


Figure 6.3 Pushover curves for (a) 3-storey and (b) 6-storey CR-CBF prototypes

The second step of the procedure is to perform incremental dynamic analysis (IDA) (Vamvatsikos and Cornell 2002). Two suites of ground motions are selected from PEER (2010); far-field and near-field as defined by FEMA P695 (2009). The methodology doesn't require the inclusion of near-field ground motion records for the collapse assessment. However, considering the high seismic risk for the prototype site in Berkeley, California, this study also considers the near-field ground motions for collapse assessment. The far-field suite includes twenty-two component pairs of horizontal ground motions from sites that are greater than or equal to 10 km from fault rupture. In this study, they are from twelve different earthquakes and are listed in Table 6.1. The near-field suite includes twenty-eight component pairs of horizontal ground motions from sites that are less than 10 km from fault rupture. In this study, they are six different ground motions and are listed in Table 6.2. Earthquakes of all fault types and pulse are considered. Only large-magnitude events greater than 6.0 are included in the record suites. To perform IDA, all these records shall be amplitude-scaled to match the MCE hazard intensity, using the procedure described in Section 5.1. During IDA, the records are scaled as a suite such that their median increases incrementally from 2% to 600% of the MCE intensity. For the 3-storey and 6-storey CR-CBF prototypes, the IDA curves of the individual ground motions as well the median IDA curve

of all the motions is given in Figure 6.4. RDR is selected as the demand measure (DM), and the ordinate is median spectral acceleration at the structural fundamental period as the ground motion intensity measure (IM). As stated already, the displacement criterion for structural collapse during IDA is assumed to be 10% RDR. Another important consideration during IDA is ignoring the apparent structural resurrection at a higher seismic intensity after already showing collapse at a previously lower seismic intensity. Hence to conservatively estimate the lowest IM triggering structural collapse, the portion of IDA curve above the first flatline is ignored (Vamvatsikos and Cornell 2002).

**Table 6.1 List of Far-Field ground motions (FEMA P695 2009)**

G.M. Number	G.M. Name	Year	Magnitude	NGA#	Record
1	San Fernando	1971	6.61	57	SFERN_ORR021
2					SFERN_ORR291
3	Imperial Valley	1979	6.53	164	IMPVALLH_H_CPE147
4					IMPVALLH_H_CPE237
5	Irpinia, Italy	1980	6.90	289	ITALY_A_CTR000
6					ITALY_A_CTR270
7	Corinth, Greece	1981	6.60	313	CORINTH_COR_L
8					CORINTH_COR_T
9	Loma Prieta	1989	6.93	755	LOMAP_CYC195
10					LOMAP_CYC285
11	Landers	1992	7.28	864	LANDERS_JOS000
12					LANDERS_JOS090
13	Landers	1992	7.28	881	LANDERS_MVH045
14					LANDERS_MVH135
15	Chi-Chi, Taiwan	1999	7.62	1184	CHICHI_CHY010_N
16					CHICHI_CHY010_W
17	Chi-Chi, Taiwan	1999	7.62	1198	CHICHI_CHY029_E
18					CHICHI_CHY029_N
19	Chi-Chi, Taiwan	1999	7.62	1484	CHICHI_TCU042_E
20					CHICHI_TCU042_N
21	Chi-Chi, Taiwan	1999	7.62	1500	CHICHI_TCU061_E
22					CHICHI_TCU061_N

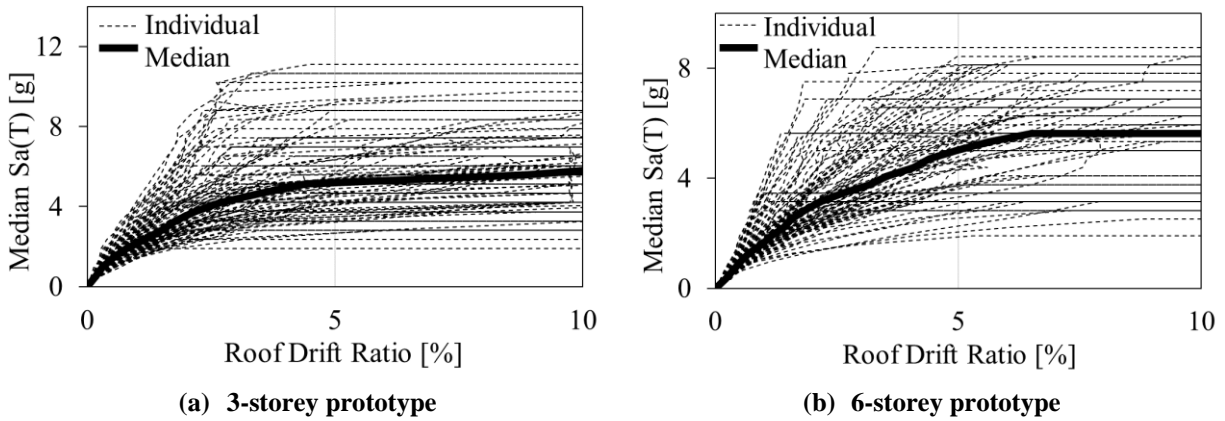
G.M. Number	G.M. Name	Year	Magnitude	NGA#	Record
23	Chi-Chi, Taiwan	1999	7.62	1533	CHICHI_TCU106_E
24					CHICHI_TCU106_N
25	Chi-Chi, Taiwan	1999	7.62	1541	CHICHI_TCU116_E
26					CHICHI_TCU116_N
27	Manjil, Iran	1990	7.37	1633	MANJIL_ABBAR_L
28					MANJIL_ABBAR_T
29	Cape Mendocino	1992	7.01	3750	CAPEMEND_LFS270
30					CAPEMEND_LFS360
31	Chuetsu-oki, Japan	2007	6.80	4841	CHUETSU_65004EW
32					CHUETSU_65004NS
33	Chuetsu-oki, Japan	2007	6.80	4843	CHUETSU_65006EW
34					CHUETSU_65006NS
35	Chuetsu-oki, Japan	2007	6.80	4850	CHUETSU_65013EW
36					CHUETSU_65013NS
37	Iwate, Japan	2008	6.90	5664	IWATE_MYG005EW
38					IWATE_MYG005NS
39	Iwate, Japan	2008	6.90	5783	IWATE_54026EW
40					IWATE_54026NS
41	Iwate, Japan	2008	6.90	5806	IWATE_55461EW
42					IWATE_55461NS
43	Darfield, New Zealand	2010	7.00	6971	DARFIELD_SPFSN17E
44					DARFIELD_SPFSN73W

Table 6.2 List of Near-Field ground motions (FEMA P695 2009)

G.M. Number	G.M. Name	Year	Magnitude	NGA#	Record
1	Irpinia, Italy	1980	6.90	285	ITALY_A_BAG000
2					ITALY_A_BAG270
3	Cape Mendocino	1992	7.01	828	CAPEMEND_PET000
4					CAPEMEND_PET090
5	Chi-Chi, Taiwan	1999	7.62	1182	CHICHI_CHY006_N
6					CHICHI_CHY006_W
7	Chi-Chi, Taiwan	1999	7.62	1193	CHICHI_CHY024_E
8					CHICHI_CHY024_N
9	Chi-Chi, Taiwan	1999	7.62	1489	CHICHI_TCU049_E
10					CHICHI_TCU049_N
11	Chi-Chi, Taiwan	1999	7.62	1490	CHICHI_TCU050_E
12					CHICHI_TCU050_N

G.M. Number	G.M. Name	Year	Magnitude	NGA#	Record
13	Chi-Chi, Taiwan	1999	7.62	1493	CHICHI_TCU053_E
14					CHICHI_TCU053_N
15	Chi-Chi, Taiwan	1999	7.62	1494	CHICHI_TCU054_E
16					CHICHI_TCU054_N
17	Chi-Chi, Taiwan	1999	7.62	1499	CHICHI_TCU060_E
18					CHICHI_TCU060_N
19	Chi-Chi, Taiwan	1999	7.62	1507	CHICHI_TCU071_E
20					CHICHI_TCU071_N
21	Chi-Chi, Taiwan	1999	7.62	1508	CHICHI_TCU072_E
22					CHICHI_TCU072_N
23	Chi-Chi, Taiwan	1999	7.62	1510	CHICHI_TCU075_E
24					CHICHI_TCU075_N
25	Chi-Chi, Taiwan	1999	7.62	1512	CHICHI_TCU078_E
26					CHICHI_TCU078_N
27	Chi-Chi, Taiwan	1999	7.62	1515	CHICHI_TCU082_E
28					CHICHI_TCU082_N
29	Chi-Chi, Taiwan	1999	7.62	1519	CHICHI_TCU087_E
30					CHICHI_TCU087_N
31	Chi-Chi, Taiwan	1999	7.62	1521	CHICHI_TCU089_E
32					CHICHI_TCU089_N
33	Chi-Chi, Taiwan	1999	7.62	1528	CHICHI_TCU101_E
34					CHICHI_TCU101_N
35	Chi-Chi, Taiwan	1999	7.62	1530	CHICHI_TCU103_E
36					CHICHI_TCU103_N
37	Chi-Chi, Taiwan	1999	7.62	1546	CHICHI_TCU122_E
38					CHICHI_TCU122_N
39	Parkfield	2004	6.00	4140	PARK2004_UP03090
40					PARK2004_UP03360
41	Parkfield	2004	6.00	4141	PARK2004_UP05090
42					PARK2004_UP05360
43	Parkfield	2004	6.00	4142	PARK2004_UP06090
44					PARK2004_UP06360
45	Parkfield	2004	6.00	4144	PARK2004_UP08090
46					PARK2004_UP08360
47	Parkfield	2004	6.00	4145	PARK2004_UP09090
48					PARK2004_UP09360
49	Parkfield	2004	6.00	4148	PARK2004_UP12090
50					PARK2004_UP12360
51	Montenegro, Yugoslavia	1979	7.10	4451	MONTENE_GRO_BSO000
52					MONTENE_GRO_BSO090
53	Iwate, Japan	2008	6.90	5656	IWATE_IWTH24EW

54					IWATE_IWTH24NS
55	Iwate, Japan	2008	6.90	5813	IWATE_44B71EW
56					IWATE_44B71NS



**Figure 6.4 IDA curves for (a) 3-storey and (b) 6-storey CR-CBF prototypes**

The third step of the FEMA P695 (2009) methodology requires the construction of collapse fragility curve from the IDA results. The collapse fragility curve represents the conditional probability of exceeding the collapse RDR limit state (10% for CR-CBF) for a given IM. The plot employs the curve fitting technique proposed by Ibarra and Krawinkler (2005). For each IDA curve shown in Figure 6.4, the spectral acceleration at collapse is obtained. Then the mean and standard deviation of the acceleration data are lognormally distributed to construct a collapse fragility curve as shown in Figure 6.5.

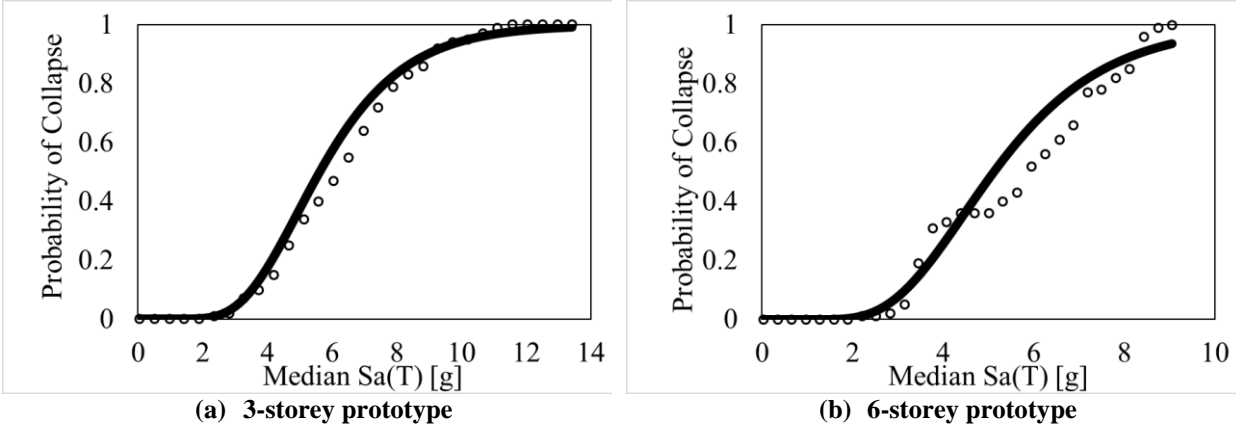


**Figure 6.5 Collapse fragility curves for (a) 3-storey and (b) 6-storey CR-CBF prototypes**

The final step of the FEMA P695 (2009) methodology is to determine whether  $ACMR$  of the CR-CBF prototypes is greater than the threshold limit  $ACMR_{10\%}$ . Firstly, the value of  $\hat{S}_{CT}$  for the 3-storey and 6-storey prototypes can be read off from collapse fragility curves given in Figure 6.5. Hence,  $\hat{S}_{CT}$  is 5.56g and 5.11g for 3-storey and 6-storey prototype, respectively. At the CR-CBF prototype fundamental period  $T$  (0.4 sec for 3-storey and 0.8 sec for 6-storey),  $S_{MT}$  is determined as 2.31g and 1.56g for the 3-storey and 6-storey prototype, respectively (ASCE/SEI 7-10 2010). Using Equation [6.5], the value of  $CMR$  is calculated to be 2.41 and 3.27 for the 3-storey and 6-storey prototype, respectively. Next,  $SSF$  for the CR-CBF prototypes is determined using  $T$  and  $\mu_T$  from Table 7-1b (FEMA P695 2009), which is 1.33 and 1.41 for 3-storey and 6-storey prototypes, respectively. Then,  $ACMR$  is calculated using Equation [6.6] and is 3.20 and 4.61 for 3-storey and 6-storey prototypes, respectively.

In order to determine the acceptable values of  $ACMR$  for 10% probability of collapse or  $ACMR_{10\%}$ , the total system collapse uncertainty,  $\beta_{TOT}$ , of the CR-CBF prototypes is required. Equation [6.7] is used to calculate  $\beta_{TOT}$  using uncertainty due to record-to-record variability in

ground motions ( $\beta_{RTR}$ ), quality ratings of design requirement ( $\beta_{DR}$ ), test data ( $\beta_{TD}$ ) and numerical model ( $\beta_{MDL}$ ).

$$\beta_{TOT} = \sqrt{\beta_{RTR}^2 + \beta_{DR}^2 + \beta_{TD}^2 + \beta_{MDL}^2} \quad [6.6]$$

Hence,  $\beta_{TOT}$  is computed to be 0.726 for both the CR-CBF prototypes; where  $\beta_{RTR}=0.40$  for  $\mu_T$  greater than 3;  $\beta_{DR} = \beta_{TD} = \beta_{MDL}= 0.35$  for fair quality rating to be conservative (FEMA P695 2009). Using the value of  $\beta_{TOT}$ , the accepted values of  $ACMR$  for 10% probability of collapse,  $ACMR_{10\%}$ , is determined as 2.53 for both the prototypes (FEMA P695 2009). Since the calculated values of  $ACMR$  are greater than the corresponding values of  $ACMR_{10\%}$ , the CR-CBF is proven to have an acceptable collapse performance.

## **Chapter 7: Conclusion**

This chapter summarizes the results, findings and potential areas for further research. Section 7.1 presents an overall summary of all the preceding chapters of this thesis. The methodology used, results of numerical analyses and keys findings in the evaluation of the seismic performance of CR-CBFs are also presented here. Based on this improved knowledge of CR-CBFs, Section 7.2 explores certain areas which would require further research.

### **7.1 Summary**

Current code-based conventional SRFs are designed to dissipate the earthquake energy through inelastic deformation which have proven to be inefficient and expensive to repair. With the advent of performance-based earthquake engineering, higher performance targets are being pursued to ensure improved performance and greater seismic resilience. This calls for novel seismic resilient structures. In this thesis, one such resilient structural system called CR-CBF is explored. To promote the use of such high performance systems, the robust and efficient EEDP methodology is employed to facilitate the design of this system. Unlike existing design methodologies, EEDP doesn't require the estimation of force-modification factors. EEDP is formulated to achieve multiple performance objectives at different hazard intensities. More importantly, it allows designers to size a structure that achieves the desired seismic performance without iterations.

In order to validate that the EEDP can be used to efficiently design CR-CBFs, two prototype office buildings were designs. Robust numerical models were built to simulate the physical response of these prototypes. Seismic performance of these models were analysed using nonlinear

dynamic analysis and the results show that the prototypes meet the performance targets selected. All the damage was concentrated in the yielding components, while the remaining components are protected. The median peak displacements in the structure were within the selected targets. To verify that these systems do not retain significant residual deformations, the structural response at the end of MCE ground motions was examined. The IRDR for both the prototypes was well within the maximum permissible limit. To further demonstrate the advantages of the using CR-CBFs, their seismic performance was compared with that of conventional code-based BRBF design. Nonlinear dynamic analysis of the BRBFs revealed extensive yielding of critical frame members and higher residual deformations in them, which can lead to hefty repair costs and considerable downtime.

Finally, to demonstrate that CR-CBFs have adequate collapse safety against earthquakes equivalent to the conventional SFRSs, FEMA P695 (2009) methodology is implemented. Both the prototypes show adequate margin of safety against collapse and further bolster confidence in these systems.

## **7.2 Future Research Needs**

During the course of this thesis, several intriguing research questions were identified which would require further investigation. This would surely reinforce confidence in CR-CBFs which show great promise in mitigating socio-economic losses associated with structural damage due to earthquakes. These topics for future research are thus summarized here.

- (i) This thesis focused on using only friction dampers as ED. However, several other devices such as self-centering braces, viscous dampers, metallic yielding dampers, etc. can be

considered as alternative energy dissipating elements. This entails additional laboratory testing of these elements subjected to asymmetric rocking motion.

- (ii) Alternative configurations of CR-CBFs with different locations of PT and ED can be studied. A parametric study could reveal the most economical configuration for a particular building height being considered.
- (iii) More prototype designs for buildings greater than 6 storeys need to be undertaken to validate the efficiency of EEDP in their design. Since rocking systems are influenced by higher mode effects, it needs to be verified that EEDP designed prototypes fulfil the requirement of keeping the frame members elastic while meeting the other performance objectives.
- (iv) The next step in designing such systems could be to allow controlled yielding of frame members and investigating its influence on the overall structural performance. The steel members have inherent ductility which could be utilized to increase the deformation capacity of the structure. However, structural residual deformations need to be examined closely to ensure they doesn't hamper the building functionality.
- (v) Further analytical and experimental study is required to determine the potential connections between the gravity system and CR-CBF to transfer the seismic forces as assumed in this thesis.

- (vi) Financial loss analysis and life-cycle cost analysis for these systems can be beneficial to understand the financial impact of different hazard levels on the structural system. It can also cater to structural engineers and owners to make crucial risk management decisions.
  
- (vii) While comparing CR-CBFs to BRBFs, certain specific structural performance parameters like peak displacements, peak accelerations and residual displacements have been discussed in this thesis. However, in order to compare the overall benefits and cost effectiveness, other key parameters that could be explored are material usage, initial and life-cycle costs, level of knowledge and expertise required for design and construction, etc.

## Bibliography

- Acikgoz, S., and DeJong, M. J. (2012). "The interaction of elasticity and rocking in flexible structures allowed to uplift." *Earthquake Engineering & Structural Dynamics*, 41(15), 2177–2194.
- Ajrab, J. J., Pekcan, G., and Mander, J. B. (2004). "Rocking wall-frame structures with supplemental tendon systems." *Journal of Structural Engineering*, 130(6), 895–903.
- ANSI/AISC 341-10. (2010). "Seismic provisions for structural steel buildings." *American Institute of Steel Construction, Chicago, IL., USA*.
- ANSI/AISC 360-10. (2010). "Specification for Structural Steel Buildings." *American Institute of Steel Construction, Chicago, IL., USA*.
- Architectural Institute of Japan. (1998). "Recommendation for enhancement of disaster mitigation in buildings and urban areas- Based on damage observed in 1995 Hyogoken-Nanbu earthquake." *Building Science (In Japanese)*, 113(1418), 9–24.
- ASCE/SEI 41-06. (2007). "Seismic Rehabilitation of Existing Buildings." *American Society of Civil Engineers, Virginia*.
- ASCE/SEI 7-10. (2010). "Minimum Design Loads for buildings and other Structures." *American Society of Civil Engineers, Virginia*.
- Aslam, M., Scalise, D. T., and Godden, W. G. (1980). "Earthquake rocking response of rigid bodies." *Journal of the Structural Division*, 106(2), 377–392.
- ASTM A992/ A992M-11. (2015). "Standard Specification for Structural Steel Shapes." *ASTM International, West Conshohocken, PA, 2015*.
- Azuhata, T., Midorikawa, M., and Ishihara, T. (2006). "Seismic response reduction of buildings by rocking structural systems with adaptive dampers." *Smart Structures and Materials*, 61691B\_1–61691B\_9.
- Beck, J. L., and Skinner, R. I. (1974). "The seismic response of a reinforced concrete bridge pier designed to step." *Earthquake Engineering & Structural Dynamics*, 2(4), 343–358.
- Berger, J., Buckle, I., and Greene, M. (2012). "The 2010 Canterbury and 2011 Christchurch New Zealand Earthquakes and the 2011 Tohoku Japan Earthquake : Emerging Research Needs and Opportunities THE U . S . NATIONAL SCIENCE FOUNDATION The 2010 Canterbury and the 2011 Christchurch New Zealand Earthquake." *CA: Earthquake Engineering Research Institute*.
- Bilham, R. (2009). "The seismic future of cities." *Bulletin of Earthquake Engineering*, 7(4), 839–887.
- Chancellor, N., Eatherton, M., Roke, D., and Akbas, T. (2014). "Self-Centering Seismic Lateral Force Resisting Systems: High Performance Structures for the City of Tomorrow." *Buildings*, 4(3), 520–548.
- Chao, S. H., Goel, S. C., and Lee, S. S. (2007). "A seismic design lateral force distribution based

- on inelastic state of structures.” *Earthquake Spectra*, 23(3), 547–569.
- Christopoulos, C., Filiatrault, A., and Folz, B. (2002). “Seismic response of self-centring hysteretic SDOF systems.” *Earthquake Engineering & Structural Dynamics*, 31(5), 1131–1150.
- Christopoulos, C., and Pampanin, S. (2004). “Towards performance-based design of MDOF structures with explicit consideration of residual deformations.” *ISET Journal of Earthquake Technology*, 41(440), 53–73.
- Christopoulos, C., Tremblay, R., Kim, H., and Lacerte, M. (2008). “Self-centering energy dissipative bracing system for the seismic resistance of structures: development and validation.” *Journal of Structural Engineering, ASCE*, 134(1), 96–107.
- Clough, R. W., and Huckelbridge, A. A. (1977). “Preliminary experimental study of seismic uplift of a steel frame.” *Earthquake Engineering Research Center, College of Engineering, University of California*.
- Deierlein, G. G., Liel, A. B., Haselton, C. B., Kircher, C. A., and Principal, K. (2008). “ATC-63 methodology for evaluating seismic collapse safety of archetype buildings.” *ASCE-SEI Structures Congress, Vancouver, BC*, 24–26.
- Dowdell, D. J., and Hamersley, B. A. (2000). “Lions’ Gate Bridge North Approach—Seismic retrofit.” *Proceedings of the 3rd International Conference on Behaviour of Steel Structures in Seismic Areas (STESSA 2000), Montreal, QC*, 319–326.
- DSI, (Dywidag Systems International). (2006). “DYWIDAG post-tensioning systems. Gormley, ON: DYWIDAG-Systems International Canada Ltd.”
- Eatherton, M., Hajjar, J., Ma, X., Krawinkler, H., and Deierlein, G. (2010). “Seismic design and behavior of steel frames with controlled rocking--Part I: Concepts and quasi-static subassembly testing.” *Structures Congress/North American Steel Construction Conference (NASCC), Orlando, FL., USA*.
- Eatherton, M. R., and Hajjar, J. F. (2010). “Large-scale cyclic and hybrid simulation testing and development of a controlled-rocking steel building system with replaceable fuses.” *Newmark Structural Engineering Laboratory, University of Illinois at Urbana-Champaign*.
- Eatherton, M. R., and Hajjar, J. F. (2011). “Residual drifts of self-centering systems including effects of ambient building resistance.” *Earthquake Spectra*, 27(3), 719–744.
- Erochko, J., Christopoulos, C., Tremblay, R., and Choi, H. (2010). “Residual drift response of SMRFs and BRB frames in steel buildings designed according to ASCE 7-05.” *Journal of Structural Engineering*, 137(5), 589–599.
- FEMA P695. (2009). “Quantification of building seismic performance factors.” *Federal Emergency Management Agency, Washington, DC*.
- FEMA, P. (2000). “Commentary for the Seismic Rehabilitation of Buildings.” *FEMA-356, Federal Emergency Management Agency, Washington, DC*.
- FEMA-355C. (2000). “State of the Art Report on Systems Performance of Steel Moment Frames Subject to Earthquake Ground Shaking – Program to Reduce the Earthquake Hazards of Steel

- Moment-Frame Structures.” *Federal Emergency Management Agency, Washington, DC.*
- Filippou, F. C., Popov, E. P., and Bertero, V. V. (1983). “Effects of Bond Deterioration on Hysteretic Behavior of Reinforced Concrete Joints – Report EERC 83-19.” *Earthquake Engineering Research Center.*
- Goel, S. C., and Chao, S. H. (2008). “Performance-based plastic design: earthquake-resistant steel structures.” *International Code Council, Washington, DC.*
- Hajjar, J., Eatherton, M., Deierlein, G., Ma, X., Pena, A., Krawinkler, H., and Billington, S. (2008). “Controlled rocking of steel frames as a sustainable new technology for seismic resistance in buildings.” *International Association of Bridge & Structural Engineering Symposium Congress Report.*
- Hall, K. S., Eatherton, M. R., and Hajjar, J. (2010). “Nonlinear behavior of controlled rocking steel-framed building systems with replaceable energy dissipating fuses.” *Newmark Structural Engineering Laboratory Report Series, (NSEL-026).*
- Hamburger, R. O., Krawinkler, H., Malley, J. O., and Adan, S. M. (2008). “Seismic design of steel special moment frames: a guide for practicing engineers.” *National Earthquake Hazards Reduction Program.*
- Horan, S. M. (2002). “Material modeling for unbonded post-tensioned precast concrete walls.” *M.S Thesis, Lehigh University.*
- Housner, G. W. (1956). “Limit design of structures to resist earthquakes.” *Proc. of 1st World Conference on Earthquake Engineering, EERI, University of California, Berkeley, 5-1-5-13.*
- Housner, G. W. (1963). “The behavior of inverted pendulum structures during earthquakes.” *Bulletin of the Seismological Society of America, 53(2), 403-417.*
- Ibarra, L. F., and Krawinkler, H. (2005). “Global collapse of frame structures under seismic excitations.” *Pacific Earthquake Engineering Research Center.*
- Iwata, Y., Sugimoto, H., and Kuwamura, H. (2006). “Reparability limit of steel structural buildings based on the actual data of the Hyogoken-Nanbu earthquake.” *Proceedings of the 38th Joint Panel. Wind and Seismic effects. NIST Special Publication, 1057, 23-32.*
- Kelly, J. M., and Tsztoo, D. F. (1977). “Earthquake simulation testing of a stepping frame with energy-absorbing devices.” *Earthquake Engineering Research Center, College of Engineering, University of California.*
- der Kiureghian, A. (1981). “A response spectrum method for random vibration analysis of MDF systems.” *Earthquake Engineering & Structural Dynamics, 9(5), 419-435.*
- Latham, D. A., Reay, A. M., and Pampanin, S. (2013). “Kilmore street medical centre: Application of a post-tensioned steel rocking system.” *Proceedings of Steel Innovations Conference.*
- Ma, Q. T. M. (2010a). “The mechanics of rocking structures subjected to ground motion.” *PhD Thesis, The University of Auckland, New Zealand.*
- Ma, X. (2010b). “Seismic design and behavior of self-centering braced frame with controlled

- rocking and energy-dissipating fuses.” *PhD Thesis, Stanford University, Stanford, CA.*
- Ma, X., Borchers, E., Pena, A., Krawinkler, H., Billington, S., and Deierlein, G. (2010a). “Design and behavior of steel shear plates with openings as energy-dissipating fuses.” *Internal Report, John A. Blume Earthquake Engineering Center, Stanford University.*
- Ma, X., Eatherton, M., Hajjar, J., Krawinkler, H., and Deierlein, G. (2010b). “Seismic design and behavior of steel frames with controlled rocking—Part II: Large scale shake table testing and system collapse analysis.” *Structures Congress/North American Steel Construction Conference (NASCC). Orlando, FL., USA.*
- Mahul, O., and White, E. (2012). “The economics of disaster risk, risk management, and risk financing.” *Earthquake Risk Insurance. Knowledge Note 6-2, IBRD- World Bank.*
- Makris, N., and Konstantinidis, D. (2003). “The rocking spectrum and the limitations of practical design methodologies.” *Earthquake Engineering & Structural Dynamics*, 32(2), 265–289.
- Mander, J. B., and Cheng, C. T. (1997). “Seismic resistance of bridge piers based on damage avoidance design.” *Technical Report NCEER, 97.*
- McCormick, J., Aburano, H., Ikenaga, M., and Nakashima, M. (2008). “Permissible residual deformation levels for building structures considering both safety and human elements.” *The 14th World Conference on Earthquake Engineering*, 12–17.
- Meek, J. W. (1975). “Effects of foundation tipping on dynamic response.” *Journal of the Structural Division, ASCE*, 101(7), 1297–1311.
- Meek, J. W. (1978). “Dynamic response of tipping core building.” *Earthquake Engineering & Structural Dynamics*, 6, 437–454.
- Midorikawa, M., Azuhata, T., Ishihara, T., Matsuba, Y., Matsushima, Y., and Wada, A. (2002). “Earthquake response reduction of buildings by rocking structural systems.” *In SPIE’s 9th Annual International Symposium on Smart Structures and Materials*, 4696(2002), 265–272.
- Midorikawa, M., Azuhata, T., Ishihara, T., Matsuba, Y., and Wada, A. (2003). “Shaking table tests on earthquake response reduction effects of rocking structural systems.” *SPIE’s 10th Annual International Symposium on Smart Structures and Materials*, 277–286.
- Midorikawa, M., Azuhata, T., Ishihara, T., and Wada, A. (2006). “Shaking table tests on seismic response of steel braced frames with column uplift.” *Earthquake Engineering & Structural Dynamics*, 35(14), 1767–1786.
- Muto, K., Umemura, H., and Sonobe, Y. (1960). “Study of the overturning vibrations of slender structures.” *Proceedings of the 2nd World Conference on Earthquake Engineering. Tokyo, Japan*, 1239–1261.
- NBCC. (2010). “National Building Code of Canada.” *National Research Council, Ontario, ON, Canada.*
- NIST, (National Institute of Standards and Technology). (2010). “Evaluation of the FEMA P695-methodology for quantification of building seismic performance factors.” *Report NIST GCR 10- 917-8. Gaithersburg, MD: National Institute of Standards and Technology.*

- Oliveto, G., Calio, I., and Greco, A. (2003). "Large displacement behaviour of a structural model with foundation uplift under impulsive and earthquake excitations." *Earthquake Engineering & Structural Dynamics*, 32(3), 369–393.
- OpenSees. (2010). "Open System for Earthquake Engineering Simulation [OpenSees] Framework – Version 2.5." *Pacific Earthquake Engineering Research Center*.
- Ozaki, F., Kawai, Y., Tankara, H., Okada, T., and Kanno, R. (2010). "Innovative damage control systems using replaceable energy dissipating steel fuses for cold- formed steel structures." *Twentieth international specialty conference on cold-formed steel structures*.
- PEER. (2010). "[http://peer.berkeley.edu/products/strong\\_ground\\_motion\\_db.html](http://peer.berkeley.edu/products/strong_ground_motion_db.html), [http://peer.berkeley.edu/products/strong\\_ground\\_motion\\_db.html](http://peer.berkeley.edu/products/strong_ground_motion_db.html) 2010 PEER Ground Motion Database – BETA version." *Pacific Earthquake Engineering Research Center*.
- Pollino, M. (2015). "Seismic design for enhanced building performance using rocking steel braced frames." *Engineering Structures*, Elsevier Ltd, 83, 129–139.
- Pollino, M., and Bruneau, M. (2007). "Seismic retrofit of bridge steel truss piers using a controlled rocking approach." *Journal of Bridge Engineering*, 12(5), 600–610.
- Pollino, M., and Bruneau, M. (2008). "Dynamic seismic response of controlled rocking bridge steel-truss piers." *Engineering Structures*, 30(6), 1667–1676.
- Priestley, M. J. N. (1991). "Overview of the PRESSS Research Programme." *PCI Journal*, 36(4), 50–57.
- Priestley, M. J. N. (2000). "Performance based seismic design." *Bulletin of the New Zealand Society for Earthquake Engineering*, 33(3), 325–346.
- Priestley, M. J. N., Calvi, G. M., and Kowalsky, M. J. (2007). "Direct displacement-based seismic design of structures." *2007 NZSEE Conference*.
- Priestley, M. J. N., Evison, R. J., and Carr, A. J. (1978). "Seismic response of structures free to rock on their foundations." *Bulletin of the New Zealand National Society for Earthquake Engineering*, 11(3), 141–150.
- Priestley, M. J. N., Sritharan, S., Conley, J., and Pampanin, S. (2000). "Preliminary Test Results from the PRESSS 5-Story Precast Concrete Building." *PCI Journal*, 44(6), 42–67.
- Psycharis, I. N. (1991). "Effect of base uplift on dynamic response of SDOF structures." *Journal of Structural Engineering*, 117(3), 733–754.
- Ricles, J. M., Sause, R., Garlock, M. M., and Zhao, C. (2001). "Post-tensioned seismic-resistant connections for steel frames." *Journal of Structural Engineering*, 127(2), 113–121.
- Roke, D., Sause, R., Ricles, J. M., and Gonner, N. (2009). "Design concepts for damage-free seismic-resistant self-centering steel concentrically-braced frames." *Structures Congress 2009*, 1421–1430.
- Roke, D., Sause, R., Ricles, J. M., Seo, C. Y., and Lee, K. S. (2006). "Self-centering seismic-resistant steel concentrically-braced frames." *Proceedings of the 8th US National Conference on Earthquake Engineering, EERI, San Francisco*, 18–22.

- Rutenberg, A., Jennings, P. C., and Housner, G. W. (1980). "The response of Veterans Hospital building 41 in the San Fernando earthquake." *Earthquake Engineering & Structural Dynamics*, 10(3), 359–379.
- S.A.N.Z. (1976). "NZS 4203: Code of practice for general structural design and design loadings for buildings." *S.A.N.Z, Wellington*, 80.
- Sabelli, R. (2001). "Research on improving the design and analysis of earthquake-resistant steel-braced frames." *NEHRP Professional Fellowship Report. EERI*, 1–142.
- Sabelli, R., Roeder, C. W., and Hajjar, J. F. (2013). "Seismic Design of Steel Special Concentrically Braced Frame Systems- A Guide for Practicing Engineers." *NEHRP Seismic Design Technical Brief*, (8), 1–36.
- Sause, R., Ricles, J. M., Chancellor, N. B., and Roke, D. A. (2014). "Hybrid Simulations of Self-Centering Concentrically-Braced Frames Subject to Extreme Ground Motions." *10th U.S. National Conference on Earthquake Engineering*.
- Sause, R., Ricles, J. M., Roke, D., Seo, C. Y., and Lee, K. S. (2006). "Design of self-centering steel concentrically-braced frames." *Proc. Of Sessions of the 4th International Conference on Earthquake Engineering, Taipei Taiwan*, 122–131.
- SEAOC. (1995). "Performance based seismic engineering of buildings." *Structural Engineers Association of California*.
- Tremblay, R., Bouaanani, N., Leclerc, M., Rene, V., Fronteddu, L., and Rivest, S. (2008a). "Innovative viscously damped rocking braced steel frames." *Proceedings of the 14th World Conference on Earthquake Engineering, Beijing, China*.
- Tremblay, R., Lacerte, M., and Christopoulos, C. (2008b). "Seismic response of multistory buildings with self-centering energy dissipative steel braces." *Journal of Structural Engineering*, 134(1), 108–120.
- Truniger, R., Vassiliou, M. F., and Stojadinovic, B. (2014). "Experimental study on the interaction between elasticity and rocking." *Proceedings of the 10th national conference in earthquake engineering, Earthquake Engineering Research Institute, Anchorage, AK*.
- Uang, C. M., and Bertero, V. V. (1988). "Use of energy as a design criterion in earthquake-resistant design." *Report No. UCB/EERC-88/18, College of Engineering, Berkeley, California*.
- UCB. (2003). "U.C. Berkeley Seismic Guideline." *University of California, Berkeley*.
- Vamvatsikos, D., and Cornell, C. A. (2002). "Incremental dynamic analysis." *Earthquake Engineering & Structural Dynamics*, 31(3), 491–514.
- Wada, A., Qu, Z., Ito, H., Motoyui, S., Sakata, H., and Kasai, K. (2009). "Seismic retrofit using rocking walls and steel dampers." *In Proc. ATC/SEI Conference on Improving the Seismic Performance of Existing Buildings and Other Structures, San Francisco, CA, US*.
- Wang, T., Aburano, H., Matsuoka, Y., Hitaka, T., and Nakashima, M. (2008). "Strengthening of weak story moment frames using a rocking system with tendons." *14th World Conference on Earthquake Engineering*.

- Wiebe, L., and Christopoulos, C. (2013). "A new performance-based design methodology for controlled rocking steel frames." *Compdyn 2013 4th ECCOMAS Thematic Conference on Computational Methods in Structural Dynamics and Earthquake Engineering, Greece*.
- Yang, T. Y., Tung, D. P., and Li, Y. (2016). "Equivalent energy-based design procedure for innovative earthquake resilient structures." *Earthquake Engineering & Structural Dynamics*, (under review).
- Yim, S. C. S., and Chopra, A. K. (1985). "Simplified earthquake analysis of multistory structures with foundation uplift." *Journal of Structural Engineering*, 111(12), 2708–2731.

## Appendices

### Appendix A Design Calculations for 3-Storey Prototype

This section of the Appendix shows the detailed calculations of the EEDP design of 3-storey prototype discussed in Chapter- 4. The floor plan, elevations and the loading conditions for the building have been given in Chapter- 4. As already discussed, the CR-CBF is a SFRS which is responsible for resisting only the lateral inertial loads due to earthquakes. Hence, the CR-CBF shall be connected to the gravity framing surrounding it in such a way that the gravity load is not transferred to it. This requires reducing the bay width of the CR-CBF to 27 feet (324 inches), so that it fits between the gravity columns. The primary SFRS or ED consists of friction device installed at both the column bases. The secondary SFRS or PT consists of unbonded mono-strand PT system. The EEDP design procedure of the 3-storey prototype CR-CBF consists of the following steps.

#### A.1 Select Performance Objectives under different Seismic Hazard Intensities

In Section 4.2, the different seismic hazards (MCE, DBE and SLE) and their corresponding spectral acceleration spectra have been computed using ASCE/SEI 7-10 (2010), assuming the location of the prototype to be *Berkeley, California* and Soil Class 'C'. Different performance levels based on displacement-based limit states have been assumed in Section 3.2, corresponding to each seismic hazard intensity.

## A.2 Select Yielding RDR $\Delta_y$ to Compute $F_y$ and $T$

For the 3-storey prototype, the yielding roof drift ratio  $\Delta_y$  is chosen to be 0.15%. Using this value and the SLE hazard as shown in Figure 4.4, the value of yielding base shear  $F_y$  is computed to be 0.3845  $W$ , where  $W$  is the tributary seismic weight of the prototype (equal to 2994 *kips*). The fundamental time period  $T$  of the structure is computed using Equation [3.12] and is equal to 0.4 *sec*. The value of  $C_0$  is estimated to be equal to 1.3 (ASCE/SEI 41-06 2007).

## A.3 Select Plastic RDR $\Delta_p$ to Compute $\gamma_a$ and $F_p$

A value of 0.9% is chosen to represent the plastic RDR,  $\Delta_p$ , that defines the second yielding point. For  $T = 0.4$  *sec* and  $\mu_p = \frac{\Delta_p}{\Delta_y} = 6$ , the appropriate plot from Figure 3.7 is referred for the value of the energy modification factor  $\gamma_a$ . Hence,  $\gamma_a$  is equal to 1.25. In Equation [3.13], the value of  $\Delta E_{E1}$  and  $\Delta E_{NM1}$  are computed as 7022.3 *kip.in* and 5617.8 *kip.in*, respectively. Thus, substituting the known values of  $\gamma_a$ ,  $\Delta E_{E1}$ ,  $\Delta_p$ ,  $H$ ,  $\Delta_y$  and  $F_y$  in Equation [3.14], the value of ultimate base shear  $F_p$  is computed and is equal to 0.5421  $W$ .

## A.4 Calculate $\gamma_b$ and Ultimate RDR $\Delta_u$

The final step to completely define the trilinear force-deformation backbone is the estimation of  $\gamma_b$  and  $\Delta_u$ . For the value of the energy modification factor  $\gamma_b$ , the appropriate plot from Figure 3.8 is referred, using the known values of  $T$  and  $\mu_p$ . Hence, this value is equal to 1.15. In Equation [3.15], the value of  $\Delta E_{E2}$  and  $\Delta E_{NM2}$  are computed as 9373.3 *kip.in* and 8150.7 *kip.in*, respectively. Thus, substituting the known values of  $\gamma_b$ ,  $\Delta E_{E2}$ ,  $\Delta_p$ ,  $H$  and  $V_u$  in Equation [3.16],

the value of ultimate RDR  $\Delta_u$  is computed and is equal to 1.83%. At the end of this exercise, the final trilinear force-deformation backbone of the prototype is completely defined and is shown in Figure 4.4.

#### **A.5 Distribute Design Base Shears between Primary and Secondary SFRSs**

The structural design process starts with the distribution of the system strength into the primary and secondary sub-systems. From Equations [3.18-3.20], the values of  $F_{ED}$ ,  $F_{PT0}$  and  $F_{PT,y}$  are calculated as  $0.32 W$ ,  $0.32 W$  and  $0.58 W$  respectively.

#### **A.6 Select Yielding Mechanisms and Design Structural Members**

This step deals with the design of yielding and non-yielding structural components of CR-CBF. Firstly, the required strength of the yielding components (ED and PT) are determined by establishing energy equilibrium using the appropriate mechanism. Based on the vertical distribution of base shear given by Equation [3.22], work-energy equation for the ED is formed. As discussed in Section 3.2.2.6.1, the seismic force demand on the ED or  $F_{ED}$  is computed by solving Equations [3.24]. Table A.1 shows the calculations for the computation of  $F_{ED}$ . Here, the value of  $F_y = 1151 \text{ kips}$  and  $d_{ED} = 324 \text{ in}$ . Hence, the required slip load of the friction device ED or  $F_{ED}$  is approximately  $719 \text{ kips}$ . A slightly lower value is however preferred, to enhance the self-centering capability of the system. Hence, the required slip load or  $F_{ED}$  is assumed to be  $700 \text{ kips}$ .

**Table A.1 Calculations for computing ED force demand for 3-storey prototype**

Storey	$h_i$ (in)	$w_i$ (kips)	$w_i h_i$	$\sum w_i h_i$	$\beta_i$	$\lambda_i$	$\lambda_i F_y h_i$	$F_{ED}$ (kips)
3	540	723.5	390690	390690	1.0	0.43	267262	719
2	360	1135	408600	799290	1.9057	0.39	161600	
1	180	1135	204300	1003590	2.339	0.18	37292	
$\Sigma$	---	2994	---	---	---	1.0	466154	

Next, initial pre-tensioning force in the PT ( $F_{PT,0}$ ) is to be determined. As discussed in Section 3.2.2.6.2,  $F_{PT,0}$  is computed by solving Equations [3.25]. Here, the value of  $F_y = 1151$  kips,  $F_{ED} = 700$  kips,  $d_{ED} = 324$  in and  $d_{PT} = 324$  in. Hence,  $F_{PT,0}$  is calculated and is equal to 734 kips. The next step is to determine the seismic force demand on PT or  $F_{PT,y}$  similar to that of the ED. As discussed in Section 3.2.2.6.2,  $F_{PT,y}$  is computed by solving Equation [3.26]. Table A.2 shows the calculations for the computation of  $F_{PT,y}$ . Here, the value of  $F_p = 1625$  kips. Hence, the required yield load of the PT or  $F_{PT,y}$  is approximately 1325 kips. Since unbonded mono-strand PT system is used, the required area of PT is:  $F_{PT,y}/\sigma_y = 1325 \text{ kips}/243 \text{ ksi} = 5.4 \text{ sq. in}$ . Hence, 25# strands of 0.6" with a prestress of 50% of the ultimate tensile strength are used, such that  $F_{PT,0} = (25)(0.217)(270)(0.5) = 740$  kips.

**Table A.2 Calculations for computing PT force demand for 3-storey prototype**

Storey	$h_i$ (in)	$w_i$ (kips)	$w_i h_i$	$\sum w_i h_i$	$\beta_i$	$\lambda_i$	$\lambda_i F_p h_i$	$F_{PT,y}$ (kips)
3	540	723.5	390690	390690	1.0	0.43	377325	1325
2	360	1135	408600	799290	1.9057	0.39	228150	
1	180	1135	204300	1003590	2.339	0.18	52650	
$\Sigma$	---	2994	---	---	---	1.0	658125	

So far, the yielding components of the CR-CBF have been designed. The final step of the design procedure is to capacity design the frame members to remain elastic under the maximum expected loads of PT, thereby concentrating all the damage at desired locations only. The capacity design procedure adopted in this thesis has been explained in Section 3.2.2.6.3. Using FBDs to establish force equilibrium at various joints in the frame, design forces for each structural component is estimated. Table A.3 summarizes the calculation of braces, beams and columns design forces and the wide flange sections chosen to satisfy them in accordance with the requirements of ANSI/AISC 360-10 (2010). Although the beam at 1<sup>st</sup> floor level doesn't carry any load, section for the storey below is used.

**Table A.3 Summary of capacity design for 3-storey prototype**

<b>BRACES</b>				
<b>Storey</b>	<b>Design Force (kips)</b>	<b>Nature of Force</b>	<b>Length (ft.)</b>	<b>Section (US)</b>
3	1783	Compression	20.18	W14x283
2	1783	Compression	20.18	W14x283
1	1783	Compression	20.18	W14x283
<b>BEAMS</b>				
<b>Storey</b>	<b>Design Force (kips)</b>	<b>Nature of Force</b>	<b>Length (ft.)</b>	<b>Section (US)</b>
3	1325	Shear and Flexure	27	W27x539
2	2386	Tension	27	W14x283
1	0	--	27	W14x159
0	1193	Tension	27	W14x159
<b>COLUMNS</b>				
<b>Storey</b>	<b>Design Force (kips)</b>	<b>Nature of Force</b>	<b>Length (ft.)</b>	<b>Section (US)</b>
3	1325	Compression	15	W14x193
2	1325	Compression	15	W14x193
1	1325	Compression	15	W14x193

## **Appendix B Design Calculations for 6-Storey Prototype**

This section of the Appendix shows the detailed calculations of the EEDP design of 6-storey prototype discussed in Chapter- 4. The floor plan, elevations and the loading conditions for the building have been given in Chapter- 4. As already discussed, the CR-CBF is a SFRS which is responsible for resisting only the lateral inertial loads due to earthquakes. Hence, the CR-CBF shall be connected to the gravity framing surrounding it in such a way that the gravity load is not transferred to it. This requires reducing the bay width of the CR-CBF to 27 feet (324 inches), so that it fits between the gravity columns. The primary SFRS or ED consists of friction device installed at both the column bases. The secondary SFRS or PT consists of post-tensioning bars. The EEDP design procedure of the 6-storey prototype CR-CBF consists of the following steps.

### **B.1 Select Performance Objectives under different Seismic Hazard Intensities**

In Section 4.2, the different seismic hazards (MCE, DBE and SLE) and their corresponding spectral acceleration spectra have been computed using ASCE/SEI 7-10 ASCE/SEI 7-10 (2010), assuming the location of the prototype to be *Berkeley, California* and Soil Class 'C'. Different performance levels based on displacement-based limit states have been assumed in Section 3.2, corresponding to each seismic hazard intensity.

### **B.2 Select Yielding RDR $\Delta_y$ to Compute $F_y$ and $T$**

For the 6-storey prototype, the yielding RDR  $\Delta_y$  is chosen to be 0.22%. Using this value and the SLE hazard as shown in Figure 4.4, the value of yielding base shear  $F_y$  is computed to be 0.2525  $W$ , where  $W$  is the tributary seismic weight of the prototype (equal to 6400 *kips*). The

fundamental time period  $T$  of the structure is computed using Equation [3.12] and is equal to 0.8 *sec*. The value of  $C_0$  is estimated to be equal to 1.42 (ASCE/SEI 41-06 2007).

### B.3 Select Plastic RDR $\Delta_p$ to Compute $\gamma_a$ and $F_p$

A value of 0.92% is chosen to represent the plastic RDR,  $\Delta_p$ , that defines the second yielding point. For  $T = 0.8 \text{ sec}$  and  $\mu_p = \frac{\Delta_p}{\Delta_y} = 4.2$ , the appropriate plot from Figure 3.7 is referred for the value of the energy modification factor  $\gamma_a$ . Hence,  $\gamma_a$  is found to be equal to 1.85. In Equation [3.13], the value of  $\Delta E_{E1}$  and  $\Delta E_{NM1}$  are computed as 28630 *kip.in* and 15475.7 *kip.in*, respectively. Thus, substituting the known values of  $\gamma_a$ ,  $\Delta E_{E1}$ ,  $\Delta_p$ ,  $H$ ,  $\Delta_y$  and  $F_y$  in Equation [3.14], the value of ultimate base shear  $F_p$  is computed and is equal to 0.3872 *W*.

### B.4 Calculate $\gamma_b$ and Ultimate RDR $\Delta_u$

The final step to completely define the trilinear force-deformation backbone is the estimation of  $\gamma_b$  and  $\Delta_u$ . For the value of the energy modification factor  $\gamma_b$ , the appropriate plot from Figure 3.8 is referred, using the known values of  $T$  and  $\mu_p$ . Hence, this value is equal to 2.1. In Equation [3.15], the value of  $\Delta E_{E2}$  and  $\Delta E_{NM2}$  are computed as 38780 *kip.in* and 18466.7 *kip.in*, respectively. Thus, substituting the known values of  $\gamma_b$ ,  $\Delta E_{E2}$ ,  $\Delta_p$ ,  $H$  and  $V_u$  in Equation [3.16], the value of ultimate RDR  $\Delta_u$  is computed and is equal to 1.61%. At the end of this exercise, the final trilinear force-deformation backbone of the prototype is completely defined and is shown in Figure 4.4.

## **B.5 Distribute Design Base Shears between Primary and Secondary SFRSs**

The structural design process starts with the distribution of the system strength into the primary and secondary sub-systems. From Equations [3.18-3.20], the values of  $F_{ED}$ ,  $F_{PT0}$  and  $F_{PT,y}$  are calculated as  $0.42 W$ ,  $0.42 W$  and  $0.87 W$  respectively.

## **B.6 Select Yielding Mechanisms and Design Structural Members**

This step deals with the design of yielding and non-yielding structural components of CR-CBF. Firstly, the required strength of the yielding components (ED and PT) are determined by establishing energy equilibrium using the appropriate mechanism. Based on the vertical distribution of base shear given by Equation [3.22], work-energy equation for the ED is formed. As discussed in Section 3.2.2.6.1, the seismic force demand on the ED or  $F_{ED}$  is computed by solving Equations [3.24]. Table B.1 shows the calculations for the computation of  $F_{ED}$ . Here, the value of  $F_y = 1616 \text{ kips}$  and  $d_{ED} = 324 \text{ in.}$  Hence, the required slip load of the friction device ED or  $F_{ED}$  is approximately  $1993 \text{ kips}$ . A slightly lower value is however preferred, to enhance the self-centering capability of the system. Hence, the required slip load or  $F_{ED}$  is assumed to be  $1950 \text{ kips}$ .

**Table B.1 Calculations for computing ED force demand for 6-storey prototype**

Storey	$h_i$ (in)	$w_i$ (kips)	$w_i h_i$	$\sum w_i h_i$	$\beta_i$	$\lambda_i$	$\lambda_i F_y h_i$	$F_{ED}$ (kips)
6	1080	723.5	781380	781380	1.0	0.29	506131	1993
5	900	1135	1021500	1802880	1.93	0.27	392688	
4	720	1135	817200	2620080	2.58	0.19	221069	
3	540	1135	612900	3232980	3.05	0.13	113443	
2	360	1135	408600	3641580	3.34	0.08	46541	
1	180	1135	204300	3845880	3.49	0.04	11635	
$\Sigma$	---	6400	---	---	---	1.0	1291507	

Next, initial pre-tensioning force in the PT ( $F_{PT,0}$ ) is to be determined. As discussed in Section 3.2.2.6.2,  $F_{PT,0}$  is computed by solving Equations [3.25]. Here, the value of  $F_y = 1616$  kips,  $F_{ED} = 1950$  kips,  $d_{ED} = 324$  in and  $d_{PT} = 324$  in. Hence,  $F_{PT,0}$  is calculated and is equal to 2009 kips. The next step is to determine the seismic force demand on PT or  $F_{PT,y}$  similar to that of the ED. As discussed in Section 3.2.2.6.2,  $F_{PT,y}$  is computed by solving Equation [3.26]. Table B.2 shows the calculations for the computation of  $F_{PT,y}$ . Here, the value of  $F_p = 2478$  kips. Hence, the required yield load of the PT or  $F_{PT,y}$  is approximately 4118 kips. Since post-tensioning bars are used, the required area of PT is:  $F_{PT,y}/\sigma_y = 4130$  kips / 120 ksi = 34.3 sq. in. Hence, 13# bars of 1.75" with a prestress of 40% of the ultimate tensile strength are used, such that  $F_{PT,0} = (13)(2.62)(150)(0.4) = 2040$  kips.

**Table B.2 Calculations for computing PT force demand for 6-storey prototype**

Storey	$h_i$ (in)	$w_i$ (kips)	$w_i h_i$	$\sum w_i h_i$	$\beta_i$	$\lambda_i$	$\lambda_i F_p h_i$	$F_{PT,y}$ (kips)
6	1080	723.5	781380	781380	1.0	0.29	776109	4130
5	900	1135	1021500	1802880	1.93	0.27	602154	
4	720	1135	817200	2620080	2.58	0.19	338990	
3	540	1135	612900	3232980	3.05	0.13	173955	
2	360	1135	408600	3641580	3.34	0.08	71366	
1	180	1135	204300	3845880	3.49	0.04	17841	
$\Sigma$	---	6400	---	---	---	1.0	1980415	

So far, the yielding components of the CR-CBF have been designed. The final step of the design procedure is to capacity design the frame members to remain elastic under the maximum expected loads on PT, thereby concentrating all the damage at desired locations only. The capacity design procedure adopted in this thesis has been explained in Section 3.2.2.6.3. Using FBDs to establish force equilibrium at various joints in the frame, design forces for each structural component is estimated. Table B.3 summarizes the calculation of braces, beams and columns design forces and the wide flange sections chosen to satisfy them in accordance with the requirements of ANSI/AISC 360-10 (2010). Although the beams at the odd floor levels don't carry any load, sections for the storey above/below with lower design loads are used.

**Table B.3 Summary of capacity design for 6-storey prototype**

<b>BRACES</b>				
<b>Storey</b>	<b>Design Force (kips)</b>	<b>Nature of Force</b>	<b>Length (ft.)</b>	<b>Section (US)</b>
6	5544	Compression	20.18	W14x550
5	5544	Compression	20.18	W14x550
4	5544	Compression	20.18	W14x550
3	5544	Compression	20.18	W14x550
2	5544	Compression	20.18	W14x550
1	5544	Compression	20.18	W14x550
<b>BEAMS</b>				
<b>Storey</b>	<b>Design Force (kips)</b>	<b>Nature of Force</b>	<b>Length (ft.)</b>	<b>Section (US)</b>
6	3710	Tension	27	W14x455
5	0	--	27	W14x455
4	7420	Tension	27	W14x808
3	0	--	27	W14x455
2	7420	Tension	27	W14x808
1	0	--	27	W14x455
0	3710	Tension	27	W14x455

<b>COLUMNS</b>				
<b>Storey</b>	<b>Design Force (kips)</b>	<b>Nature of Force</b>	<b>Length (ft.)</b>	<b>Section (US)</b>
6	4120	Compression	15	W14x398
5	4120	Compression	15	W14x398
4	4120	Compression	15	W14x398
3	4120	Compression	15	W14x550
2	4120	Compression	15	W14x550
1	4120	Compression	15	W14x550